学位論文

Anisotropic superconducting gaps in YNi_2B_2C: A first-principles investigation (YNi_2B_2Cにおける異方的超伝導ギャップの第一原理的研究)

平成26年12月博士 (理学) 申請

東京大学大学院理学系研究科
物理学専攻

河村 光晶

Abstract

The borocarbide superconductor YNi_2B_2C has received significant interest because of its highly anisotropic superconducting gaps. From the observation of the isotope effect of boron atoms, it has been assumed that the electron-phonon interaction mainly induces the superconductivity in this material. However, it is an open question how the anisotropic superconducting gap of this material is realized with the phonon-induced superconducting mechanism.

In this study, we develop an accurate scheme and perform first-principles calculations based on density functional theory for superconductors to investigate the details of the superconducting gap function, where we particularly focus on its variation over the Fermi surfaces and the origin of the anisotropic gap function. For that purpose, we develop the optimized tetrahedron method by which we can calculate accurately phonons and response functions with less computational costs.

Calculated phonon frequencies, the quasiparticle density of states, and the transition temperature show good agreement with experimental results. From our calculation of superconducting gaps and orbital character analysis, we establish that the orbital character variation of the Fermi surface is the key factor of the anisotropic gap. Since the electronic states that consist of mainly Ni $3d$ orbitals couple weakly with phonons, the superconducting gap function is suppressed for the corresponding states, which results in the anisotropy observed in the experiments. These results are hints to increase the transition temerature of materials in the borocarbide family.

Contents

1 Introduction **9**
1.1 YNi_2B_2C and related materials . . . 9
1.2 Previous studies . . . 11
1.2.1 Specific heat . . . 11
1.2.2 Neutron diffraction . . . 11
1.2.3 Ultrasonic attenuation . . . 12
1.2.4 Thermal conductivity . . . 12
1.2.5 Tunnel conductance . . . 13
1.2.6 De Haas-van Alphen experiment and band structure calculation . . . 13
1.2.7 Angle-resolved photoemission spectroscopy . . . 14
1.3 Objective and the outline of this thesis . . . 14

2 Density functional theory for superconductors **17**
2.1 Density functional theory for the normal state . . . 17
2.2 Density functional perturbation theory . . . 19
2.2.1 Born-Oppenheimer approximation . . . 19
2.2.2 Harmonic approximation and phonons . . . 20
2.2.3 Calculation of the dynamical matrix . . . 21
2.2.4 The electron-phonon interaction . . . 22
2.3 DFT for phonons and superconducting electrons . . . 22
2.3.1 Extended Hohenberg-Kohn theorem . . . 23
2.3.2 Functionals . . . 25
2.4 Gap equation . . . 25
2.4.1 Decoupling approximation . . . 25
2.4.2 The exchange-correlation kernel . . . 27
2.4.3 The screened Coulomb interaction . . . 29

3 Numerical methods **31**
3.1 Brillouin-zone integration . . . 31
3.1.1 Difficulty in the Brillouin-zone integration . . . 31
3.1.2 Linear tetrahedron method and its drawbacks . . . 32
3.1.3 Optimized tetrahedron method . . . 33
3.1.4 Implementation of the optimized tetrahedron method . . . 34
3.1.5 Comparison with other integration schemes for actual calculations . . . 36
3.2 Integrations in the gap equation . . . 39
3.2.1 Difficulty in the calculation of the gap equation . . . 39
3.2.2 Auxiliary gap function . . . 39
3.3 The overall procedure . . . 41

4 Result **43**
4.1 Verification of our code 43
4.2 Electronic structures of normal state 43
4.3 Phonons and electron-phonon interactions 46
4.4 Superconducting gaps and transition temperature 49
4.5 The QPDOS and the ultrasonic attenuation 51

5 Discussion **53**
5.1 Origin of the anisotropic superconducting gaps 53
5.2 Ultrasonic attenuation experiment vs SCDFT gap functions 54
5.2.1 Calculated results that agree or disagree with experiments 54
5.2.2 Possible causes of the disagreement 55

6 Summary and conclusion **59**

Table 1: Notations used in this thesis. Unless I specify the unit, we use the Hartree unit ($\hbar = m_e = e = 4\pi\epsilon_0 = 1$) and set $k_\mathrm{B} = 1$.

Indices	
k, k', q	Bloch wave numbers
n, n'	Band indices
σ, σ'	Spin indices $\uparrow, \downarrow$
ν	Indices of phonon branches
R, R'	Lattice indices or Lattice vector.
τ, τ'	Indices or Position of atom in the unit cell
α, α'	Direction in Cartesian coordinate (x, y, z).
Quantities	
ε_{nk}	Kohn-Sham energy
ξ_{nk}	Kohn-Sham energy measured from μ
$\omega_{q\nu}$	Phonon frequency
$\eta_{q\nu}^{\tau\alpha}$	the α component of polarization vector of the nucleus τ of the normal mode with q as a wavenumber and ν as a branch index.
T	Temperature.
β	Inverted temperature. $1/T$.
λ	Fröhlich's mass enhancement factor.
N_C	Number of unit cells.
$\langle \hat{A} \rangle$	Ensemble average of $\hat{A}$.
ω_n	Odd Matsubara frequency. $2\pi(n+1)/\beta$.
ν_n	Even Matsubara frequency. $2\pi n/\beta$.
Operators	
$\hat{H}$	Hamiltonian.
$\hat{\psi}_\sigma(r)$	Annihilation operator of electrons.
Abbreviations	
BZ	Brillouin Zone.
KS	Kohn-Sham.
ES	Equilibrium State.
Functions	
$f(\xi)$	Fermi-Dirac distribution function.
$n(\omega)$	Bose-Einstein distribution function.
$\theta(x)$	Step function.

Chapter 1

Introduction

In this chapter, we explain the motivation of this study. We briefly introduce the previous studies, set a perspective of the study, and present an overview of the thesis.

1.1 YNi_2B_2C and related materials

The borocarbide family [1, 2] represented as $L_kT_l\mathrm{B}_n\mathrm{C}_m$ (L = Sc, Y, or lanthanoid, T = Co, Ni, Rh, Pd, Ir, or Pt) are interesting for their various properties despite that they show almost the same structure (see Table 1.1); the materials in this family consist of stacked ($L_k\mathrm{C}_m$) and ($T_l\mathrm{B}_n$) layers (See Fig. 1.1). E.g., although valence configuration of atomic Sc, Y, La, and Lu is similar ($3d4s^2$, $4d5s^2$, $5d6s^2$, and $4f^{14}5d6s^2$, respectively), $LaNi_2B_2C$ does not exhibit superconductivity.

In the borocarbide family, YNi_2B_2C has attracted particular attention for its anisotropic superconducting gap. The experimental results of YNi_2B_2C are summarized as follows:

- The isotope effect of boron is observed [9, 10].

YNi_2B_2C Space group : I4/mmm (No. 139) Bravais lattice : Body-centered tetragonal

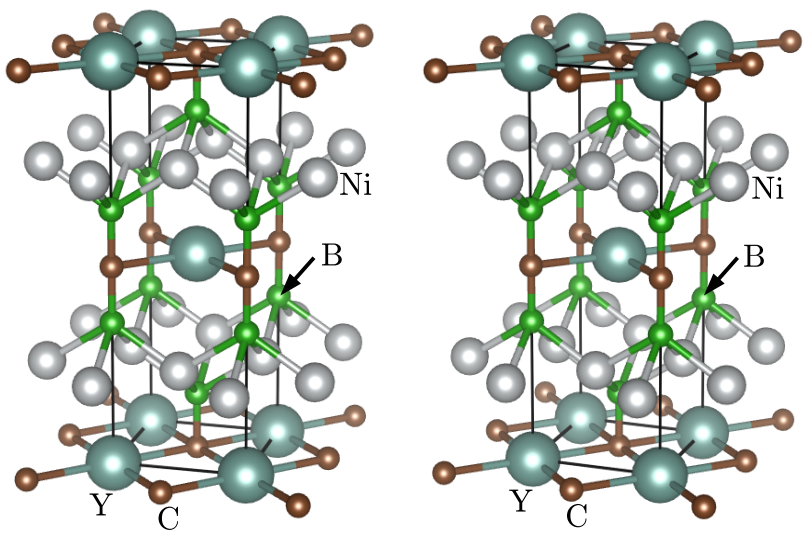

Figure 1.1: Parallel stereogram of crystalline structure of YNi_2B_2C.

Table 1.1: List of a part of materials in the borocarbide family together with their properties such as the superconducting transition temperature (T_c), the Néel temperature (T_N), and so on [3].

$ScNi_2B_2C$	Superconductivity ($T_c = 15.6K$) [4]
YNi_2B_2C	Superconductivity ($T_c = 15.6K$)
$LaNi_2B_2C$	Superconductivity is unobserved.
$CeNi_2B_2C$	Superconductivity of the heavy Fermion ($T_c = 0.1K$) [5]
$NdNi_2B_2C$	Antiferromagnetism ($T_N = 4.8K$), Superconductivity is unobserved [6].
$DyNi_2B_2C$	Antiferromagnetism ($T_N = 10.6K$) Superconductivity ($T_c = 6.2K$) [7]
$HoNi_2B_2C$	Reentrant superconductivity ($T_c = 8K$)
$YbNi_2B_2C$	Superconductivity is unobserved. The heavy Fermion
$LuNi_2B_2C$	Superconductivity ($T_c = 16.6K$)
YNiBC	Superconductivity ($T_c = 2.9K$)
LuNiBC	Superconductivity ($T_c = 3K$)
YPd_2B_2C	Superconductivity ($T_c = 23K$), metastable structure[8]

- The specific heat of YNi_2B_2C rises in proportion to the cube of the temperature ($C_p \propto T^3$). The specific heat of it in the vortex state is proportional to the square root of the magnetic field ($\sqrt{H}$) while that of an isotropic superconductor is proportional to H [11, 12, 13].

- The tunnel conductance spectrum has a broad peak[14]; it is a sign of the anisotropic gaps.

- The behavior of the ultrasonic attenuation coefficient is highly anisotropic [15].

- In the magnetic field, thermal conductivity strongly depends on the direction of the field [16].

- Apparent softening of the transverse acoustic (TA) phonon mode at $q = (0.55, 0, 0)$ is observed [17].

- The combination of the band structure calculation and the de Haas-van Alphen (dHvA) experiment indicates that there is a Fermi surface where the mass enhancement from phonons is small [18].

- Angle-resolved photoemission spectroscopy (ARPES) experiment observe the anisotropic gap ratio ($\Delta_{max}/\Delta_{min} = 3.2/1.5 = 2.1$)

Among the above reports, the most remarkable one is the boron isotope effect. On this basis, it has been assumed that the major driving force of the superconductivity is the phonon-mediated pairing interaction [10]. However, this scenario casts a fundamental question: Whether the phonon mechanism can realize such anisotropic gap as observed in the experiments?

To discuss this point more clearly, in the following sections, we explain details of the above previous studies.

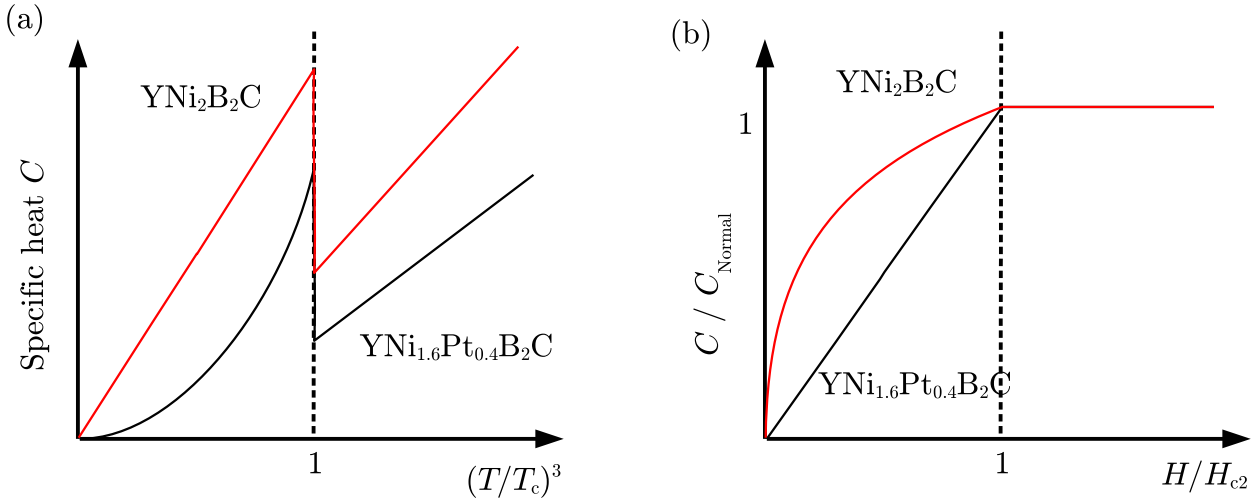

Figure 1.2: Schematic illustration of (a) the temperature dependence and (b) the magnetic field dependence of the specific heat; the red solid line and the black solid line indicate the specific heat of YNi_2B_2C and $YNi_{1.6}Pt_{0.4}B_2C$, respectively.

1.2 Previous studies

1.2.1 Specific heat

In the isotropic superconductor, the rise of the specific heat is proportional to the exponential of the temperature because of the gap. In YNi_2B_2C, it is proportional to T^3 [11] [Fig. 1.2 (a)]; This indicates that there is a small- or zero-gap region in the k-space. This T-cubic dependence turns into the T-exponential one when some Ni atoms are replaced with Pt atoms.

The specific heat of YNi_2B_2C shows also unusual magnetic field dependence; it is proportional to the square root of the field strength [11, 12, 13] [Fig. 1.2 (b)]. In an isotropic superconductor, the specific heat is proportional to the field strength; this H-linear dependence is understood as follows: In the vortex state, there are gap-less excitations whose density of states is proportional to the number of vortex lines. If the shape of the vortex lattice does not change, the number of vortex lines per unit area is proportional to the magnetic-field strength. Therefore, the low-temperature specific heat is proportional to field strength [19]. On the other hand, the unusual $\sqrt{H}$ dependence in YNi_2B_2C is explained as follows: When we increase the magnetic field, the vortex lattice turns into the square lattice from the triangular lattice [20, 21]; this transformation of the vortex lattice reduce the number of vortex lines per unit area. It is considered that the vortex-vortex interaction mediated by gap-less quasiparticles causes this transformation.

1.2.2 Neutron diffraction

In the metallic system, the ion-ion interaction is screened by electrons on Fermi surfaces. An inter-atomic force screened strongly in the presence of nested Fermi surfaces yields a low-frequency phonon; this is called the softening of the phonon due to electrons.

In YNi_2B_2C [17], significant softening occurs in the TA mode at $\boldsymbol{q} = (0.55, 0, 0)$ (Fig. 1.3), which suggests that the Fermi Surfaces have a nested regions connected by the corresponding q.

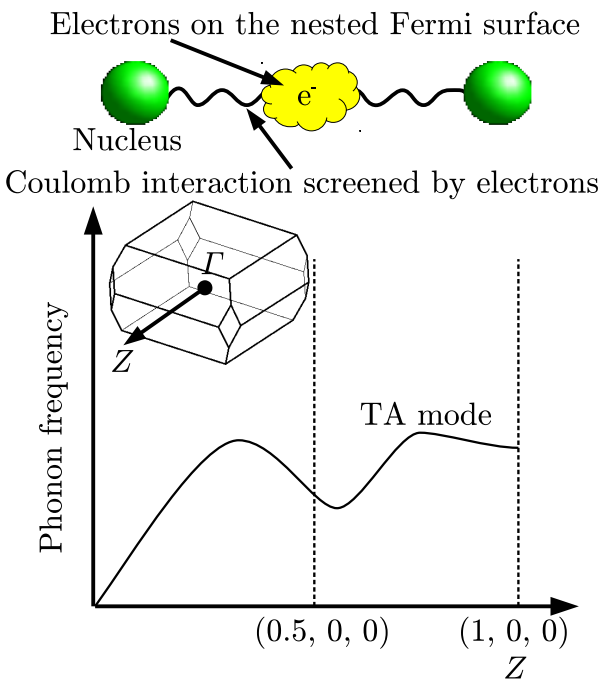

Figure 1.3: Schematic illustration of the softening of the phonon due to the response of electrons.

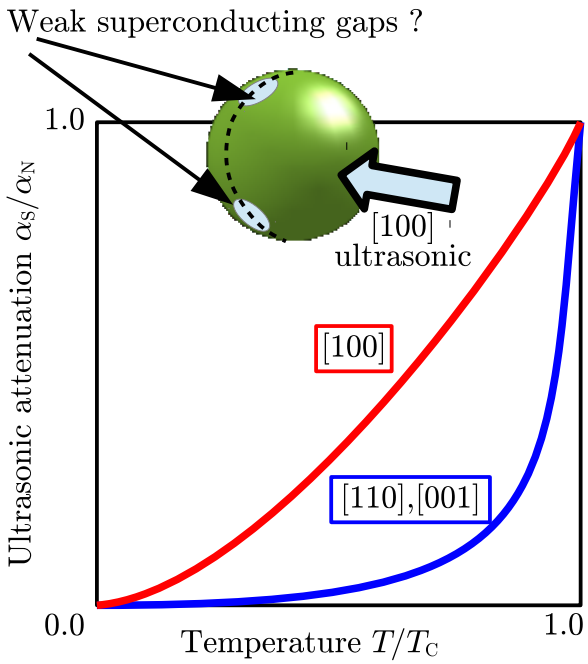

Figure 1.4: Schematic illustration of the ultrasonic attenuation.

1.2.3 Ultrasonic attenuation

When a superconductor is irradiated with ultrasonic waves, the Cooper pairs on the equator of the Fermi surface are destroyed, which causes ultrasonic attenuation. If these electrons have large superconducting gaps at low temperature, the ultrasonic attenuation hardly occurs, and as temperature becomes higher, thermally activated electrons couple with the ultrasonic wave, which also yield the attenuation.

In YNi_2B_2C [15], ultrasonic wave traveling in [100] direction is attenuated more strongly than that in [110] or [001] direction (see Fig. 1.4); this result indicates that there is small-gap regions on the equator corresponding to [100] direction.

1.2.4 Thermal conductivity

In a superconductor without magnetic field, thermal conduction hardly occurs because quasiparticles are hardly excited as the thermal carrier due to the superconducting gap. With the magnetic field, the vortices emerge in the superconductor and then the quasiparticle excitation energy shifts with $\boldsymbol{v}_S \cdot \boldsymbol{v}_F$ (the Doppler shift), where $\boldsymbol{v}_S$ and $\boldsymbol{v}_F$ are the superconducting current velocity and the Fermi velocity, respectively. Therefore, quasiparticles can be excited easily in the region where superconducting gap is smaller than the Doppler shift. If these regions are large enough, thermal conduction occurs in the superconductor.

In YNi_2B_2C [16], thermal conductivity is enhanced in the magnetic field in a particular direction (see Fig. 1.5); this result indicates that there are large regions where either the superconducting gap is small or the Fermi velocity is large.

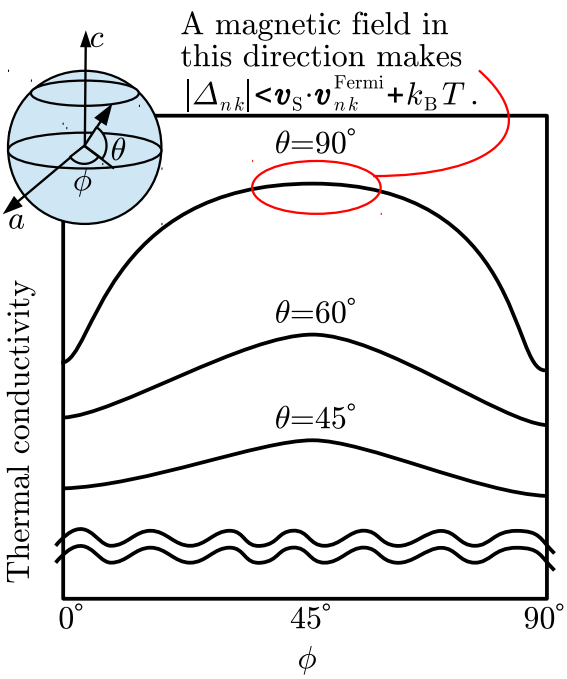

Figure 1.5: Schematic illustration of the thermal conductivity under the magnetic field.

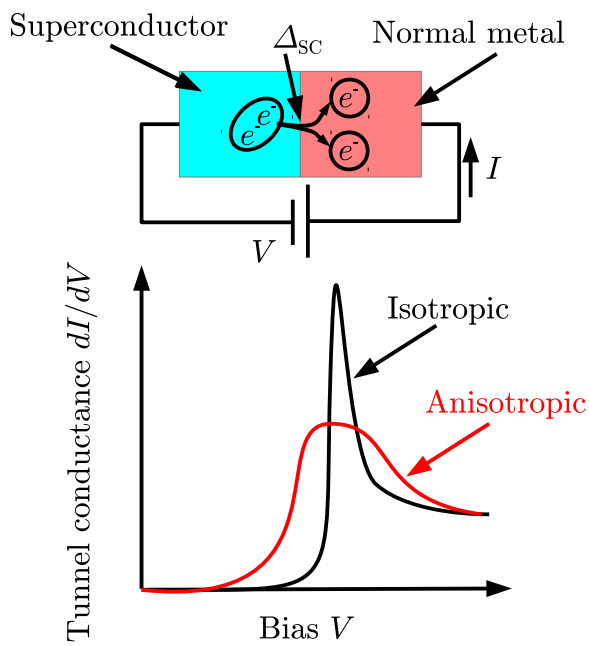

Figure 1.6: Schematic illustration of the tunnel spectrum measurement.

1.2.5 Tunnel conductance

In the tunnel conductance spectrum measurement, voltage is applied to the interface between a superconductor and a metal. When electrons transfer from the superconductor to the metal, the Cooper pair have to be destroyed (See upper panel of Fig. 1.6). Therefore, the bias larger than the superconducting gap is needed to apply the current. With the Fermi golden rule, we can obtain that the tunnel conductance dI/dV is proportional to the superconducting quasiparticle density of states (QPDOS) and the QPDOS has the Van Hove singularity at the superconducting gap when the gap is perfectly isotropic.

In YNi_2B_2C [14], the tunnel conductance spectrum shows a broad peak (See Fig. 1.6); this indicates that the superconducting gap varies over Fermi surfaces.

1.2.6 De Haas-van Alphen experiment and band structure calculation

With the combination of the dHvA experiment and the first-principles band-structure calculation, the shape of the Fermi surface has been analyzed [18]. In that analysis, authors apply modifications from the ordinary LDA calculation to reproduce cyclotron frequency branches obtained in the dHvA experiment: they shift upwardly Y $4d$ and Ni $3d$ level from those obtained with LDA by 0.11 Ry and 0.05 Ry. With these shifts, the obtained Fermi surface has a small electron pocket. The phononic mass-enhancement factor λ of electrons has been obtained from the ratio between the electronic effective mass of the experiment and that of the calculation ($\lambda = m_{\mathrm{exp}}/m_{\mathrm{calc}} - 1$); λ of the small electron pocket in the vicinity of the Γ point is specifically small (about one seventh of those of other Fermi surfaces).

1.2.7 Angle-resolved photoemission spectroscopy

Angle-resolved photoemission spectroscopy (ARPES) can observe directory the superconducting gap. The previous study observed superconducting-gap anisotropy on Fermi surfaces of YNi_2B_2C [22]; the minimum and the maximum of the superconducting gap on Fermi surfaces are 1.5 meV and 3.2 meV, respectively. The minimum of the superconducting gap is located on the Γ-Z-X-P plane; the observed ratio between the maximum and the minimum of the superconducting gap ($\Delta_{\max}/\Delta_{\min}$) is 2.1. These results do not agree with results obtained in the thermal conductivity measurement and the ultrasonic attenuation measurement; in these two experiments much larger anisotropy ($\Delta_{\max}/\Delta_{\min} \sim 10$ in the ultrasonic attenuation experiment, and it approximately 100 in the thermal conductivity measurement) and the superconducting-gap minimum at [100] direction are observed. These discrepancies may be due to the limitation of the measured region in the Brillouin zone in the ARPES experiment.

1.3 Objective and the outline of this thesis

As seen above, various experimental and theoretical studies suggests that the superconducting gap function have some anisotropic properties. However, it is still controversial to what extent the size of the gap varies over the Fermi surface. For example, the ultrasonic and Doppler-shift experiments has been understood by assuming the gap function with nodes [15, 16]. On the other hand, the tunneling and ARPES measurements have not detected signatures of the gap nodes. To clarify the property of the gap and its origin, *ab initio* calculation can be a powerful tool.

In this study, we investigate the mechanism of the anisotropic superconductivity in YNi_2B_2C. In particular, we focus on the possibility of the gap function having strong anisotropy emerging from the phonon-mediated pairing interaction. To calculate the k-dependent superconducting gap from first principles, we have to calculate dressed anomalous Green's functions on the basis of the Eliashberg theory [23, 24] or the G_0W_0 theory for superconductors [25, 26], with all the variables (k points, band indices, and Matsubara frequencies) retained; such a calculation requires us an unrealistically large numerical cost.

Alternatively, we employ the density functional theory for superconductors (SCDFT) [27], by using which we can obtain superconducting properties with a realistic numerical cost without any empirical parameters. We can obtain transition temperature and the real-space superconducting order parameter from the SCDFT gap function Δ_{nk} which is a solution of the following gap equation:

$$\Delta_{nk} = -\frac{1}{2}\sum_{n'k'} K_{nkn'k'} \tanh\left(\frac{\beta\varepsilon_{n'k'}}{2}\right)\frac{\Delta_{n'k'}}{\varepsilon_{n'k'}}. \tag{1.1}$$

This is successful in calculations of quantities in the superconducting state of elemental metals [28], MgB_2 [29], fcc lithium under high pressure [30, 31], and CaC_6 [32]. Although it is not guaranteed that the SCDFT superconducting gap is identical to the experimental gap, we consider that SCDFT describes the experimental gap on the semiquantitative level for the following reasons. It is known that there is a suggestive relation between SCDFT gaps and G_0W_0 gaps; from dressed anomalous Green's function $F^R_{nk}(\omega)$, we can obtain the G_0W_0 gap as

$$\Delta_{nk} \equiv 2|\xi_{nk}| \int_0^\infty \frac{d\omega}{2\pi} \mathrm{Im} F^R_{nk}(\omega), \tag{1.2}$$

where ξ_{nk} is the Kohn-Sham energy; this gap satisfies the gap equation similar to the one of SCDFT [25]. In the previous study for some materials based on SCDFT, the calculated gap agrees with the gap obtained in the tunnel conductance experiment.

In order to discuss the k dependence of the gap function, it is quite important to evaluate the k-dependent electronic and phononic properties accurately. However, the current standard methods for the electronic and phononic calculations do not meet this requirement. The problem stems from the Brillouin-zone integration of various functions rapidly varying over the Fermi surface, which must be managed in the electronic and phononic calculations. In prior to the superconducting problem, we revisit this point and develop an accurate numerical method for the Brillouin-zone integral, which is applicable to a very wide range of electronic and phononic calculations.

The outline of this thesis is as follows: In Chap. 2, we explain the theory to calculate atomic and electronic structure in the normal state (density functional theory), phonons and electron-phonon interactions (density functional perturbation theory), and superconducting properties such as the superconducting gap (density functional theory for superconductors). In Chap. 3, we develop the numerical method to perform the Brillouin-zone integration appearing in the calculations of phonons and response functions. With the optimized tetrahedron method proposed in this work, we can obtain these quantities accurately with less numerical costs. We also develop a method to solve the gap equation accurately. In Chap. 4, we show the resulting electronic and phonic structure of YNi_2B_2C; we show the band structure, Fermi surfaces, and the superconducting gap function. We also show the phonon dispersion, the superconducting transition temperature, the quasiparticle density of states, and the ultrasonic attenuation coefficient together with the corresponding experimental results. In Chap. 5, we discuss the origin of the anisotropic superconducting gaps in YNi_2B_2C. We also discuss improvement from calculations of this study to describe the experimental results more accurately. For this purpose, we examine whether the treatment of the Y $4d$ and the Ni $3d$ orbitals performed in Ref. [18] improves on the description of the anisotropic superconductivity in YNi_2B_2C. Finally in Chap. 6, we summarize this thesis and show future prospects.

Chapter 2

Density functional theory for superconductors

In this chapter, we explain the density functional theory for superconductors (SCDFT), which can describe superconductors without any empirical parameters. Before that, we introduce the density functional theory for the normal state and a method for calculating phonon frequency and electron-phonon interaction from the first principles.

2.1 Density functional theory for the normal state

The Hamiltonian for the interacting many-electron system is written as

$$\hat{H} = \sum_{\sigma} \int \hat{\psi}^{\dagger}_{\sigma}(r) \left(-\frac{\nabla^2}{2} + V(r) \right) \hat{\psi}_{\sigma}(r) + \frac{1}{2} \sum_{\sigma\sigma'} \iint d^3r d^3r' \frac{\hat{\psi}^{\dagger}_{\sigma}(r)\hat{\psi}^{\dagger}_{\sigma'}(r')\hat{\psi}_{\sigma'}(r')\hat{\psi}_{\sigma}(r)}{|r-r'|}, \quad (2.1)$$

where $\hat{\psi}_{\sigma}(r)$ is the annihilation operator for the electron of spin σ and position r and $V(r)$ is the crystalline potential. According to the Hohenberg-Kohn theorem [33], there is a functional of electronic charge density ρ of this system ($E_v[\rho]$) and it has following properties (figure 2.1).

- The minimum of this functional is equal to the total energy of the ground state of this system.
- The charge density giving the minimum of $E_v[\rho]$ is identical to that of the ground state.

Then, we separate $E_v[\rho]$ into

$$E_v[\rho] \equiv E^{\mathrm{kin}}_{\mathrm{eff}}[\rho] + E_{\mathrm{H}}[\rho] + E_{\mathrm{XC}}[\rho] + \int d^3r V(r)\rho(r), \quad (2.2)$$

where $E^{\mathrm{kin}}_{\mathrm{eff}}$ is the kinetic energy of the Kohn-Sham (KS) auxiliary non-interacting system [34] whose charge density of the ground state is also ρ, $E_{\mathrm{H}}[\rho]$ is the Hartree energy

$$E_{\mathrm{H}}[\rho] \equiv \frac{1}{2} \iint d^3r d^3r' \frac{\rho(r)\rho(r')}{|r-r'|}. \quad (2.3)$$

$E_{\mathrm{XC}}[\rho]$ is the remaining part part of the total energy, and it is called exchange correlation (XC) energy.

The Hamiltonian of the KS system is defined as

$$\hat{H}_{\text{eff}} = \sum_{\sigma} \int d^3r \hat{\psi}^{\dagger}_{\sigma}(r) \left(-\frac{\nabla^2}{2} + V_{\text{eff}}(r) \right) \hat{\psi}_{\sigma}(r), \tag{2.4}$$

where $V_{\text{eff}}(r)$ is the effective one-particle potential

$$V_{\text{eff}}(r) = V(r) + \int d^3r' \frac{\rho(r')}{|r - r'|} + \frac{\delta E_{\text{XC}}[\rho]}{\delta \rho(r)}. \tag{2.5}$$

This potential guarantees that the charge density of the ground state for H_{eff} becomes identical to that of the original (interacting) system; it can be obtained with the help of the variational principle $\delta E_v[\rho]/\delta\rho(r) = 0$. The ground-state charge density of the KS system is

$$\rho(r) = \sum_{nk}^{N} |\varphi_{nk}(r)|^2, \tag{2.6}$$

where $phi_{nk}(r)$ is the Kohn-Sham orbital, which satisfies the following equation

$$\left(-\frac{\nabla^2}{2} + V_{\text{eff}}(r) \right) \varphi_{nk}(r) = \varepsilon_{nk} \varphi_{nk}(r). \tag{2.7}$$

We can obtain the charge density with the self-consistent cycle of Eqs. (2.7), (2.6), and (2.5).

Although the exact and explicit form of E_{XC} is not known, various approximations for E_{XC} have been proposed. The local density approximation (LDA) is one of such approximations, where E_{XC} is assumed to have the following form:

$$E^{\text{LDA}}_{\text{XC}}[\rho] \approx \int d^3r \rho(r) \varepsilon_{\text{hom}}(\rho(r)), \tag{2.8}$$

where $\varepsilon_{\text{hom}}(\rho)$ is the XC energy per unit volume of the homogeneous electron gas with ρ being charge density. Explicit forms of ε_{hom} as a functions of ρ are obtained for examples with the

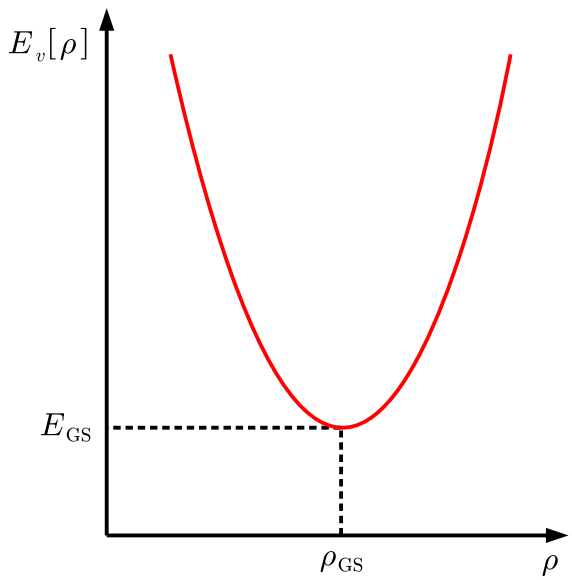

Figure 2.1: Schematic illustlation of the energy Functional for DFT.

Monte Carlo calculation for the homogeneous electron gas [35, 36]. The LDA is improved on by including the gradient of the charge density [37, 38] as

$$E_{\mathrm{XC}}^{\mathrm{GGA}}[\rho] \approx \int d^3r \rho(r) \varepsilon_{\mathrm{hom}}(\rho(r)) F_{\mathrm{XC}}(\rho(r), |\nabla\rho(r)|). \tag{2.9}$$

This generalized-gradient approximation (GGA) has been successful in various calculations of the electronic and atomic structures.

The extension of the DFT to the finite temperature system is straightforward [39]; instead of the total energy functional $E_v[\rho]$, we use the grand potential functional as

$$\Omega_v[\rho](T,\mu) \equiv E_{\mathrm{eff}}^{\mathrm{kin}}(T,\mu) - TS_{\mathrm{eff}}(T,\mu) - \mu N[\rho] + E_{\mathrm{H}}[\rho] + \Omega_{\mathrm{XC}}[\rho](T,\mu) + \int d^3r V(r)\rho(r). \tag{2.10}$$

With the variational principles $\delta\Omega_v[\rho]/\delta\rho(r) = 0$, the effective one-particle potential $V_{\mathrm{eff}}(r)$ of the finite temperature KS system is obtained as

$$V_{\mathrm{eff}}(r) = V(r) + \int d^3r' \frac{\rho(r')}{|r-r'|} + \frac{\delta\Omega_{\mathrm{XC}}[\rho]}{\delta\rho(r)}. \tag{2.11}$$

2.2 Density functional perturbation theory

In this section, we explain methods to calculate phonons and electron-phonon interactions from the first principles.

2.2.1 Born-Oppenheimer approximation

The Hamiltonian for interacting electrons and nuclei is written as

$$\begin{aligned}\hat{H} = &\sum_\sigma \int \hat{\psi}_\sigma^\dagger(r) \left(-\frac{\nabla^2}{2} + \sum_{R\tau} \frac{Z_\tau}{|r-(R+\tau+\hat{U}_{R\tau})|} \right) \hat{\psi}_\sigma(r) \\ &+ \frac{1}{2}\sum_{\sigma\sigma'} \iint d^3r d^3r' \frac{\hat{\psi}^\dagger(r)_\sigma \hat{\psi}_{\sigma'}^\dagger(r') \hat{\psi}_{\sigma'}(r') \hat{\psi}_\sigma(r)}{|r-r'|} \\ &+ \sum_{R\tau} \frac{|\hat{P}_{R\tau}|^2}{2M_\tau} + \sum_{RR'\tau\tau'} \frac{Z_\tau Z_{\tau'}}{|R+\tau+\hat{U}_{R\tau}-R'-\tau'-\hat{U}_{R'\tau'}|}.\end{aligned} \tag{2.12}$$

$\hat{U}_{R\tau}$ is the displacement operator of the ion with R and τ being the indices of the lattice and the internal coordinates, respectively; therefore the position operator of nuclei is

$$\hat{R}_\tau \equiv R_\tau^0 + \hat{U}_{R\tau} \equiv R + \tau + \hat{U}_{R\tau} \tag{2.13}$$

where R_τ^0 is the equilibrium position and other notations are listed in Table 1. Because the mass of a nucleus is much heavier than the mass of an electron, it is reasonable to employ the Born-Oppenheimer approximation, where the electrons are always in the ground state for any nuclear configurations. Then the Hamiltonian for the nuclei becomes

$$\hat{H}_{\mathrm{BO}} = \sum_{R\tau} \frac{|\hat{P}_{R\tau}|^2}{2M_\tau} + E(\{U_{R\tau}\}) \tag{2.14}$$

where

$$E(\{U_{R\tau}\}) = \Big\langle \Phi^e_{\rm GS}(\{U_{R\tau}\}) \Big| \sum_\sigma \int \hat{\psi}^\dagger_\sigma(r) \left(-\frac{\nabla^2}{2} + \sum_{R\tau} \frac{Z_\tau}{|r-(R+\tau+U_{R\tau})|} \right) \hat{\psi}_\sigma(r)$$
$$+\frac{1}{2}\sum_{\sigma\sigma'} \iint d^3r d^3r' \frac{\hat{\psi}^\dagger(r)_\sigma \hat{\psi}^\dagger_{\sigma'}(r')\hat{\psi}_{\sigma'}(r')\hat{\psi}_\sigma(r)}{|r-r'|} \Big| \Phi^e_{\rm GS}(\{U_{R\tau}\}) \Big\rangle$$
$$+ \sum_{RR'\tau\tau'} \frac{Z_\tau Z_{\tau'}}{|R+\tau+\hat{U}_{R\tau}-R'-\tau'-\hat{U}_{R'\tau'}|}, \tag{2.15}$$

and $\Phi^e_{\rm GS}(\{U_{R\tau}\})$ is the ground-state wave-function of electrons with nuclei regarded as classical particles fixed at $\{R+\tau+U_{R\tau}\}$.

In a metallic system, the Born-Oppenheimer approximation is not a precise framework because electrons are excited easily owing to the absence of the gap; this effect mainly appears as the electron-phonon interaction, which we will explain later.

2.2.2 Harmonic approximation and phonons

If the displacements of atoms are small, the Hamiltonian (2.14) becomes

$$\hat{H}_{\rm BO} = \sum_{R\tau\alpha} \frac{\hat{P}_{R\tau\alpha}\hat{P}_{R\tau\alpha}}{2M_\tau} + \sum_{RR'\tau\tau'} C_{\tau\alpha\tau'\alpha'}(R-R')\hat{U}_{R\tau\alpha}\hat{U}_{R'\tau'\alpha'}, \tag{2.16}$$

where inter-atomic force constant $C_{\tau\alpha\tau'\alpha'}(R-R')$ is

$$C_{\tau\alpha\tau'\alpha'}(R-R') \equiv \frac{\delta^2 E(\{U_{R\tau}\})}{\delta U_{R\tau\alpha}\delta U_{R'\tau'\alpha'}}. \tag{2.17}$$

This Hamiltonian is diagonalized as follows:

1. We perform the Fourier transformation of $\hat{P}_R$, $\hat{U}_R$, and $C(R-R')$ as

$$\hat{P}_{R\tau\alpha} \equiv {N_{\rm C}}^{-1/2}\sum_q \hat{P}_{q\tau\alpha}e^{iqR}, \qquad \hat{U}_{R\tau\alpha} \equiv {N_{\rm C}}^{-1/2}\sum_q \hat{U}_{q\tau\alpha}e^{iqR},$$
$$\bar{C}_{\tau\alpha\tau'\alpha'}(q) \equiv {N_{\rm C}}^{-1}\sum_{RR'} C_{\tau\alpha\tau'\alpha'}(R-R')e^{-iqR}e^{iqR'}. \tag{2.18}$$

   Then the Hamiltonian (2.16) becomes

$$\hat{H} = \sum_{q\tau\alpha} \frac{\hat{P}^\dagger_{q\tau\alpha}\hat{P}_{q\tau\alpha}}{2M_\tau} + \sum_{q\tau\tau'} \bar{C}_{\tau\alpha\tau'\alpha'}(q)\hat{U}^\dagger_{\tau\alpha}(q)\hat{U}_{\tau'\alpha'}(q), \tag{2.19}$$

   where $\bar{C}(q)$ is called the dynamical matrix.

2. We rewrite $\hat{P}_q$ and $\hat{U}(q)$ by using a dimensionless phonon-annihilation operator $\hat{b}$ as

$$\hat{U}_{q\tau\alpha} = \sum_\nu (2M_\tau\omega_{q\nu})^{-1/2}\eta^{\tau\alpha}_{q\nu}(\hat{b}_{q\nu} + \hat{b}^\dagger_{-q\nu}),$$
$$\hat{P}_{q\tau\alpha} = \sum_\nu (2M_\tau\omega_{q\nu})^{1/2}\eta^{\tau\alpha}_{q\nu}(\hat{b}_{q\nu} - \hat{b}^\dagger_{-q\nu}), \tag{2.20}$$

where $\eta_{q\nu}^{\tau\alpha}$ and $\omega_{q\nu}$ are the polarization vector and the frequency of the phonon; they are obtained by diagonalizing the normalized dynamical matrix as

$$\sum_{\tau'\alpha'} \frac{\bar{C}_{\tau\alpha\tau'\alpha'}(q)}{\sqrt{M_\tau M_{\tau'}}} \eta_{\tau'\alpha'}^{q\nu} = \omega_{q\nu}^2 \eta_{\tau\alpha}^{q\nu}. \tag{2.21}$$

3. Then we rewrite the Hamiltonian (2.19) by using $\hat{b}$ as

$$\hat{H} = \sum_{q\nu} \omega_{q\nu} \left(b_{q\nu}^\dagger b_{q\nu} + \frac{1}{2} \right). \tag{2.22}$$

2.2.3 Calculation of the dynamical matrix

As seen in the previous section, the calculation of the second derivative of $E(\{U_{R\tau}\})$ with respect to U [Eq. 2.17] is needed in the calculation of the phonon; to perform this calculation, there are following two methods (we assume calculation of phonons of $3N_{\text{atom}}$ branches, N_q wavenumbers of the system which has N_{atom} atoms in the unit cell).

Frozen phonon method We calculate the second derivative from the difference of the force of each atoms with finite displacement in the supercell whose size is proportional to the number of the phonon q vectors (N_q).

Density functional perturbation theory (DFPT) [40] We calculate the second derivative by using the perturbation theory. We can obtain the screened electron-phonon interaction as a by-product of the dynamical matrix.

In this work, we use the DFPT for calculations of phonons. First, we transform the dynamical matrix as follows.

$$\begin{aligned} C_{\tau\alpha\tau'\alpha'}(q) = N_{\text{C}}^{-1} \sum_{RR'} e^{-iqR} e^{iqR'} \Bigg\{ & \frac{\delta^2}{\delta R_{\tau\alpha}^0 \delta R_{\tau'\alpha'}^0} \frac{Z_\tau Z_{\tau'}}{|R_\tau - R'_{\tau'}|} \\ & + \int d^3 r \rho(r) \left(\frac{\delta\rho(r)}{\delta R_{\tau\alpha}^0} \frac{\delta V(r)}{\delta R_{\tau'\alpha'}^0} + \rho(r) \frac{\delta^2 V(r)}{\delta R_{\tau\alpha}^0 \delta R_{\tau'\alpha'}^0} \right) \Bigg\}, \end{aligned} \tag{2.23}$$

where

$$V(r) = \sum_{R\tau} \frac{Z_\tau}{|r - (R + \tau)|} \tag{2.24}$$

is the crystalline potential. The first and third terms of the dynamical matrix (2.23) are calculated directly, while $\delta\rho/\delta R$ in the second term is calculated using the perturbation theory as follows:

$$\begin{aligned} N_{\text{C}}^{-1/2} \sum_R e^{iqR} \frac{\delta\rho(r)}{\delta R_{\tau\alpha}^0} = & \sum_{knn'} \frac{\theta(\varepsilon_{n'k+q} - \mu) - \theta(\varepsilon_{nk} - \mu)}{\varepsilon_{n'k+q} - \varepsilon_{nk}} \\ & \times \int d^3 r \varphi_{n'k+q}^*(r) N_{\text{C}}^{-1/2} \sum_R e^{-iqR} \frac{\delta V_{\text{eff}}(r)}{\delta R_{\tau\alpha}^0} \varphi_{nk}(r). \end{aligned} \tag{2.25}$$

The spatial integration in the formula (2.25) is performed only in the unit cell because

$$\int d^3r\varphi^*_{n'k+q}(r)\sum_R e^{-iqR}\frac{\delta V_{\rm eff}(r)}{\delta R^0_{\tau\alpha}}\varphi_{nk}(r) = \int d^3r e^{-i(k+q)r}\bar{\varphi}^*_{n'k+q}(r)\sum_R e^{iqR}\frac{\delta V_{\rm eff}(r)}{\delta R^0_{\tau\alpha}}e^{ikr}\bar{\varphi}_{nk}(r)$$
$$= \int d^3r\bar{\varphi}^*_{n'k+q}(r)\sum_R e^{iq(r-R)}\frac{\delta V_{\rm eff}(r)}{\delta R^0_{\tau\alpha}}\bar{\varphi}_{nk}(r), \tag{2.26}$$

where $\bar{\varphi}_{nk}(r)$ is the periodic part of the Bloch wave function ($\varphi_{nk}(r) \equiv e^{ikr}\bar{\varphi}_{nk}(r)$), and $\sum_R e^{iq(r-R)}\delta V_{\rm eff}(r)/\delta R$ is also periodic. The derivative of $V_{\rm eff}$ with respect to R is obtained by using the Eq. (2.5) as

$$N_{\rm C}^{-1/2}\sum_R e^{iqR}\frac{\delta V_{\rm eff}(r)}{\delta R^0_{\tau\alpha}} = N_{\rm C}^{-1/2}\sum_R e^{iqR}\frac{\delta V(r)}{\delta R^0_{\tau\alpha}}$$
$$+\int d^3r'\left(\frac{1}{|r-r'|}+\frac{\delta^2 E_{\rm XC}}{\delta\rho(r)\delta\rho(r')}\right)N_{\rm C}^{-1/2}\sum_R e^{iqR}\frac{\delta\rho(r')}{\delta R^0_{\tau\alpha}}. \tate{2.27}$$

Practically, we solve self-consistently Eqs. (2.25) and (2.27).

2.2.4 The electron-phonon interaction

The crystalline potential is deformed by atomic displacement; this causes the electron-phonon interaction. The vertex function represented in Fig. 2.2 is obtained from the first order derivative of the crystalline potential.

The linear part of the change in the crystalline potential is

$$\Delta V(r) = V(r;\{R\}) - V(r;\{R^0\}) \approx \sum_{R\tau\alpha}\frac{\partial V}{\partial R^0_{\tau\alpha}}\hat{U}_{R\tau\alpha}$$
$$= N_{\rm C}^{-1/2}\sum_{R\tau\alpha q} e^{-iqR}\frac{\partial V}{\partial R^0_{\tau\alpha}}\hat{U}_{q\tau\alpha} = \sum_{q\nu}(\hat{b}_{q\nu}+\hat{b}^\dagger_{q\nu})V_{q\nu}(r), \tag{2.28}$$

where we use the formula (2.20) and

$$V^{\rm bare}_{q\nu}(r) \equiv \sum_{\tau\alpha}(2M_\tau\omega_{q\nu})^{-1/2}\eta^{\tau\alpha}_{q\nu}N_{\rm C}^{-1/2}\sum_R e^{iqR}\frac{\delta V(r)}{\delta R^0_{\tau\alpha}}. \tag{2.29}$$

Replacing $V(r)$ with $V_{\rm eff}(r)$, we can obtain electron-phonon interaction screened by electrons. The screened electron-phonon vertex function g represented in Fig. 2.2 is the matrix element between two KS orbitals as

$$g^{q\nu}_{n'k+qnk} = \int d^3r\varphi^*_{n'k+q}(r)V_{q\nu}(r)\varphi_{nk}(r), \tag{2.30}$$

Replacing $V(r)$ with $V_{\rm eff}(r)$ in Eq. (2.29), we obtain $V_{q\nu}(r)$ instead of $V^{\rm bare}_{q\nu}(r)$ and it finally yields $g^{q\nu}_{n'k+qnk}$ via Eq. (2.30).

2.3 DFT for phonons and superconducting electrons

In this section, we explain the basic of the density functional theory for superconductors.

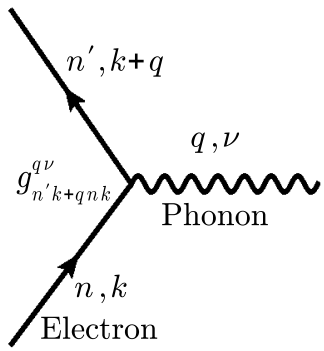

Figure 2.2: Electron-phonon vertex represented in Eqn. (2.30).

2.3.1 Extended Hohenberg-Kohn theorem

Because phonons play a significant role in superconductors, we start from the Hamiltonian (2.12). According to the extended Hohenberg-Kohn theorem for phonons and superconducting electrons [27, 41], there is a functional $\Omega[\rho, \chi, D]$ [1], where

$$\rho(r) = \sum_{\sigma} \left\langle \hat{\psi}^{\dagger}_{\sigma}(r)\hat{\psi}_{\sigma}(r) \right\rangle \text{ as the charge density,} \tag{2.31}$$

$$\chi(r, r') = \left\langle \hat{\psi}_{\uparrow}(r)\hat{\psi}_{\downarrow}(r') \right\rangle \text{as the superconducting singlet order parameter,} \tag{2.32}$$

$$D_{R\tau\alpha R'\tau'\alpha'} = \left\langle \hat{U}_{R\tau\alpha}\hat{U}_{R'\tau'\alpha'} \right\rangle \text{as the mean square displacement;} \tag{2.33}$$

this functional satisfies the following conditions.

1. The minimum of this functional is the grand potential of the equilibrium state of this system.

2. ρ, χ, and D giving the minimum of $\Omega[\rho, \chi, D]$ are identical to those of the equilibrium state.

Then, we decompose $\Omega[\rho, \chi, D]$ into several forms in the manner similar to that in DFT of the normal state;

$$\Omega[\rho, \chi, D] \equiv E^{\text{kin}}_{\text{eff,e}}[\rho, \chi] - TS_{\text{eff,e}}[\rho, \chi] + E^{\text{kin}}_{\text{eff,n}}[D] - TS_{\text{eff,n}}[D] + E_{\text{H}} + \Omega_{\text{XC}}[\rho, \chi, D], \tag{2.34}$$

where each parts are as follows:

1. E_{H} represents the Hartree energy, which contains normal Hartree energy, anomalous Hartree energy, and the classical electron-nucleus and nucleus-nucleus Coulomb interaction as

$$\begin{aligned} E_{\text{H}} \equiv & \frac{1}{2}\iint d^3r d^3r' \frac{\rho(r)\rho(r')}{|r-r'|} + \frac{1}{2}\iint d^3r d^3r' \frac{|\chi(r,r')|^2}{|r-r'|} \\ & + \int d^3r \sum_{R\tau} \frac{Z_\tau \rho(r)}{|r-(R+\tau)|} + \sum_{RR'\tau\tau'} \frac{\delta^2}{\delta R^0_{\tau\alpha}\delta R^0_{\tau'\alpha'}} \frac{Z_\tau Z_{\tau'} D_{R\tau\alpha R'\tau'\alpha'}}{|R^0_\tau - R'^0_{\tau'}|}. \end{aligned} \tag{2.35}$$

[1] We note that although the extended Hohenberg-Kohn theorem has been formulated with $\rho(r)$, $\chi(r, r')$, and $\Gamma(R_1, \cdots, R_{N_{\text{atom}}})$ in the original paper[41], where $\Gamma(R_1, \cdots, R_{N_{\text{atom}}})$ is the diagonal part of the nuclear N_{atom} particle density matrix, we formulate that theorem with $\rho(r)$, $\chi(r, r')$, and D. The reason of our modification is for simplification. Practically, this modification causes no difference between our formulation and the former one because the correlation functions of more than three nuclei have not been utilized in practice.

2. $E^{\rm kin}_{\rm eff,e}[\rho,\chi]$ and $S_{\rm eff,e}[\rho,\chi]$ are the kinetic energy and the entropy of the auxiliary non-interacting system whose equilibrium charge density and superconducting order parameter are ρ and χ, respectively; the Hamiltonian of this system is

$$\hat{H}_{\rm eff,e} \equiv \sum_\sigma \int d^3r \hat{\psi}^\dagger_\sigma(r)\left(-\frac{\nabla^2}{2}+V_{\rm eff}(r)\right)\hat{\psi}_\sigma(r) - \iint d^3r d^3r' \{\hat{\psi}_\uparrow(r)\hat{\psi}_\downarrow(r')\Delta^*_{\rm eff}(r,r') + \hat{\psi}^\dagger_\downarrow(r')\hat{\psi}^\dagger_\uparrow(r)\Delta_{\rm eff}(r,r')\}. \tag{2.36}$$

The equilibrium charge density and superconducting order parameter of this system are

$$\rho(r) = 2\sum nk\{|u_{nk}(r)|^2 f(\varepsilon_{nk}) + |v_{nk}(r)|^2 f(-\varepsilon_{nk})\},$$
$$\chi(r) = \sum nk\{u_{nk}(r)v^*_{nk}(r')f(-\varepsilon_{nk}) - u_{nk}(r')v^*_{nk}(r)f(\varepsilon_{nk})\}, \tag{2.37}$$

where we obtain $u_{nk}(r)$, $v_{nk}(r)$, and ε_{nk} by solving the following the Kohn-Sham-Bogoliubov-de Gennes equation;

$$\left\{-\frac{\nabla^2}{2}+V_{\rm eff}(r)-\mu\right\}u_{nk}(r) + \int d^3r' \Delta_{\rm eff}(r,r')v_{nk}(r') = \varepsilon_{nk}u_{nk}(r). \tag{2.38}$$

$$-\left\{-\frac{\nabla^2}{2}+V_{\rm eff}(r)-\mu\right\}v_{nk}(r) + \int d^3r' \Delta^*_{\rm eff}(r',r)u_{nk}(r') = \varepsilon_{nk}v_{nk}(r). \tag{2.39}$$

3. $E^{\rm kin}_{\rm eff,n}[D]$ and $S_{\rm eff,n}[D]$ are the kinetic energy and the entropy of the auxiliary system whose equilibrium mean square displacement is D; the Hamiltonian of this system is

$$\hat{H}_{\rm eff,n} = \sum_{R\tau}\frac{|\hat{P}_{R\tau}|^2}{2M_\tau} + \sum_{RR'\tau\tau'} C^{\rm eff}_{R\tau\alpha R'\tau'\alpha'}\hat{U}_{R\tau\alpha}\hat{U}_{R'\tau'\alpha'}. \tag{2.40}$$

Then, we diagonalize this Hamiltonian with the same method written in the previous section and obtain

$$D_{R\tau\alpha R'\tau'\alpha'} = \sum_{q\nu}\frac{\eta^{\tau\alpha}_{q\nu}\eta^{\tau'\alpha'}_{-q\nu}e^{iq(R-R')}}{\omega_{q\nu}\sqrt{M_\tau M_{\tau'}}}\left\{n(\omega_{q\nu})+\frac{1}{2}\right\}. \tag{2.41}$$

4. $\Omega_{\rm XC}[\rho,\chi,D]$ is the remains of the grand potential.

The consistency of ρ, χ, and D between original system and Kohn-Sham system is guaranteed by effective potentials $V_{\rm eff}$, $\Delta_{\rm eff}$, and $C^{\rm eff}$; with the help of the variation principles as

$$\frac{\delta\Omega}{\delta\rho(r)}=0, \quad \frac{\delta\Omega}{\delta\chi(r,r')}=0, \quad \frac{\delta\Omega}{\delta D_{R\tau\alpha R'\tau'\alpha'}}=0, \tag{2.42}$$

We obtain forms of effective potentials as

$$V_{\rm eff}(r) = \sum_{R\tau}\frac{Z_\tau}{|r-(R+\tau)|} + \int d^3r'\frac{\rho(r')}{|r-r'|} + \frac{\delta\Omega_{\rm XC}}{\delta\rho(r)}, \tag{2.43}$$

$$\Delta_{\rm eff}(r,r') = -\frac{\chi(r,r')}{|r-r'|} - \frac{\delta\Omega_{\rm XC}}{\delta\chi^*(r,r')}, \tag{2.44}$$

$$C_{R\tau\alpha R'\tau'\alpha'} = \sum_{RR'\tau\tau'}\frac{\delta^2}{\delta R^0_{\tau\alpha}\delta R^0_{\tau'\alpha'}}\frac{Z_\tau Z_{\tau'}}{|R^0_\tau - R'^0_{\tau'}|} + \frac{\delta\Omega_{\rm XC}}{\delta D_{R\tau\alpha R'\tau'\alpha'}}. \tag{2.45}$$

2.3.2 Functionals

To perform the SCDFT calculation, we need an explicit form of the $\Omega_{\rm XC}$. Since the exact form of the $\Omega_{\rm XC}$ is not known, we employ an approximation to $\Omega_{\rm XC}$.

A method to approximate $\Omega_{\rm XC}$ is the many-body perturbation theory [42]; in this method, we separate the Hamiltonian into

$$\hat{H} = \hat{H}_{\rm eff,e} + \hat{H}_{\rm eff,n} + (\hat{H} - \hat{H}_{\rm eff,e} - \hat{H}_{\rm eff,n}) \equiv \hat{H}_{\rm eff,e} + \hat{H}_{\rm eff,n} + \hat{H}_1. \tag{2.46}$$

Then, we obtain $\Omega_{\rm XC}$ as

$$\begin{aligned}\Omega_{\rm XC} &= \Omega - \Omega_{\rm eff} - E_{\rm H} + \Omega_{V_{\rm eff}} + \Omega_{\Delta_{\rm eff}} + \Omega_{C_{\rm eff}} \\ &= \frac{-1}{\beta}\sum_{n=1}\frac{(-1)^n}{n!}\int_0^\beta d\tau_1\int_0^{\tau_1}d\tau_2\cdots\int_0^{\tau_{n-1}}d\tau_n\langle\hat{H}_1(\tau_1)\cdots\hat{H}_1(\tau_n)\rangle_{SL} \\ &\quad - E_{\rm H} + \Omega_{V_{\rm eff}} + \Omega_{\Delta_{\rm eff}} + \Omega_{C_{\rm eff}},\end{aligned} \tag{2.47}$$

where $\Omega_{\rm eff}$ is the grand potential of the auxiliary non-interacting system whose Hamiltonian is $\hat{H}_{\rm eff,e} + \hat{H}_{\rm eff,n}$,

$$\Omega_{V_{\rm eff}} \equiv \int\int d^3r\rho(r)V_{\rm eff}(r), \tag{2.48}$$

$$\Omega_{\Delta_{\rm eff}} \equiv -\iint d^3rd^3r'\{\chi(r,r')\Delta^*_{\rm eff}(r,r') + \chi(r,r')^*(r,r')\Delta_{\rm eff}(r,r')\}, \tag{2.49}$$

$$\Omega_{C_{\rm eff}} \equiv \sum_{RR'\tau\tau'} C^{\rm eff}_{R\tau\alpha R'\tau'\alpha'}D_{R\tau\alpha R'\tau'\alpha'}, \tag{2.50}$$

$\hat{H}_1(\tau)$ is the interaction representation of $\hat{H}_1$ as

$$\hat{H}_1(\tau) = e^{\tau\hat{H}_S}\hat{H}_1e^{-\tau\hat{H}_S}, \tag{2.51}$$

and $\langle\hat{A}\rangle_{SL}$ denotes the contribution from all connected diagrams in the calculation of the ensemble-average of the operator $\hat{A}$ in the auxiliary system.

Alternatively, the local density approximation to $\Omega_{\rm XC}$ has been also proposed [43], but it does not include the effect of phonons.

2.4 Gap equation

In this section, we explain the procedure to perform actual calculation of SCDFT.

2.4.1 Decoupling approximation

In the original SCDFT, ρ, χ, and D affect each other. However, there is a large difference in magnitude of $V_{\rm eff}$ and $\Delta_{\rm eff}$; this difference makes Eqs. (2.38) and (2.39) numerically unstable. Hence, the self-consistent steps to obtain ρ, χ, and D [Eqs. (2.31), (2.32), (2.33)] are decoupled with the following approximations [41];

- Because ρ is insensitive to χ and D, we calculate ρ with the DFT for the normal state as described in section 2.1.
- Because D is insensitive to χ, we calculate D with the Born-Oppenheimer approximation as described in 2.2.

- We construct effective potential $\Delta_{\rm eff}[\rho,\chi,D]$ using ρ and D obtained in the above two steps; the self-consistent calculation of SCDFT is performed only for χ.

To perform the last step, we derive the SCDFT gap equation with the following procedure. The last step of this procedure is transformed to the partially linearized gap equation as follows:

1. We expand u_{nk} and v_{nk} in the Kohn -Sham-Bogoliubov-de Gennes equation (2.38, 2.39) as

$$u_{nk}(r)=\sum_{n'}\tilde{u}_{nn'k}\varphi_{n'k}(r),\quad v_{nk}(r)=\sum_{n'}\tilde{v}_{nn'k}\varphi_{n'k}(r), \tag{2.52}$$

where $\varphi_{nk}(r)$ is the Kohn-Sham orbital calculated in the normal-state DFT; and therefore $\varphi_{nk}(r)$ satisfies

$$\left\{-\frac{\nabla^2}{2}+V^e_{\rm eff}(r)-\mu\right\}\varphi_{nk}(r)=\xi_{nk}\varphi_{nk}(r). \tag{2.53}$$

Then, Eqs. (2.38) and (2.39) are transformed as follows

$$\xi_{nk}\tilde{u}_{nnk}+\sum_{n'}\Delta_{nn'k}\tilde{v}_{nn'k}=\varepsilon_{nk}\tilde{u}_{nnk}, \tag{2.54}$$

$$-\xi_{nk}\tilde{v}_{nnk}+\sum_{n'}\Delta^*_{nn'k}\tilde{u}_{nn'k}=\varepsilon_{nk}\tilde{v}_{nnk}, \tag{2.55}$$

where

$$\Delta_{nn'k}=\iint d^3rd^3r'\varphi^*_{nk}(r)\Delta_{\rm eff}[\rho,\chi,D](r,r')\varphi_{n'k}(r'). \tag{2.56}$$

2. We neglect the off-diagonal part of $\Delta_{nn'k}$; then, Eqs. (2.54) and (2.55) are simplified to the following secular equation;

$$\xi_{nk}\tilde{u}_{nk}+\Delta_{nk}\tilde{v}_k=\varepsilon_{nk}\tilde{u}_k, \tag{2.57}$$

$$-\xi_{nk}\tilde{v}_{nk}+\Delta^*_{nk}\tilde{u}_k=\varepsilon_{nk}\tilde{v}_k, \tag{2.58}$$

where $\Delta_{nk}\equiv\Delta_{nnk}$, $\tilde{u}_{nk}\equiv\tilde{u}_{nnk}$, and $\tilde{v}_{nk}\equiv\tilde{v}_{nnk}$.

3. We solve analytically this secular equation and obtain $\tilde{u}_{nk}$, $\tilde{v}_{nk}$, and ε_{nk} as

$$\tilde{u}_{nk}=\frac{1}{\sqrt{2}}\frac{\Delta_{nk}}{|\Delta_{nk}|}\sqrt{1+\frac{\xi_{nk}}{\varepsilon_{nk}}},\quad \tilde{v}_{nk}=\frac{1}{\sqrt{2}}\sqrt{1-\frac{\xi_{nk}}{\varepsilon_{nk}}}.\quad \varepsilon_{nk}=\sqrt{\xi^2_{nk}+|\Delta_{nk}|^2}. \tag{2.59}$$

4. We obtain the order parameter as

$$\chi(r,r')=\sum_{nk}\chi_{nk}\varphi_{nk}(r)\varphi^*_{nk}(r'), \tag{2.60}$$

where

$$\chi_{nk}=\iint d^3rd^3r'\varphi^*_{nk}(r)\chi(r,r')\varphi_{nk}(r')=\frac{1}{2}\frac{\Delta_{nk}}{\varepsilon_{nk}}\tanh\left(\frac{\beta\varepsilon_{nk}}{2}\right). \tag{2.61}$$

5. We construct the Kohn-Sham gap equation from Eqs. (2.56), (2.60), and $\Delta_{\rm eff} = \delta\Omega_{\rm HXC}/\delta\chi^*(r,r')$ as

$$\Delta_{nk} = -\iint d^3r d^3r' \varphi^*_{nk}(r) \frac{\delta\Omega_{\rm HXC}}{\delta\chi^*_{n'k'}} \frac{\delta\chi^*_{n'k'}}{\delta\chi^*(r,r')} \varphi_{n'k}(r') = -\frac{\delta\Omega_{\rm HXC}}{\delta\chi^*_{nk}}, \tag{2.62}$$

where $\Omega_{\rm HXC} \equiv E_{\rm H} + \Omega_{\rm XC}$. In the vicinity of the transition temperature, this gap equation can be linearized partially as

$$\begin{aligned}\Delta_{nk} &= -\sum_{n'k'} \frac{\delta^2\Omega_{\rm HXC}}{\delta\chi^*_{nk}\delta\chi_{n'k'}} \left.\frac{\delta\chi_{n'k'}}{\delta\Delta_{n'k'}}\right|_{\Delta=0}\Bigg|_{\xi=\varepsilon} \Delta_{n'k'} \\ &= -\frac{1}{2}\sum_{n'k'} K_{nkn'k'} \tanh\left(\frac{\beta\varepsilon_{n'k'}}{2}\right) \frac{\Delta_{n'k'}}{\varepsilon_{n'k'}},\end{aligned} \tag{2.63}$$

where $K_{nkn'k'}$ is the exchange-correlation kernel

$$K_{nkn'k'} \equiv \frac{\delta^2\Omega_{\rm HXC}}{\delta\chi^*_{nk}\delta\chi_{n'k'}}. \tag{2.64}$$

2.4.2 The exchange-correlation kernel

In this study, we approximate the perturbation Hamiltonian $\hat{H}_1$ in Eq (2.47) as

$$\hat{H}_1 = \hat{U}_{ee} + \hat{U}_{ep}, \tag{2.65}$$

where

$$\hat{U}_{ee} = \frac{1}{2}\sum_{\sigma\sigma'} \iint d^3r d^3r' \hat{\psi}^\dagger_\sigma(r)\hat{\psi}^\dagger_{\sigma'}(r') \frac{1}{|r-r'|} \hat{\psi}_{\sigma'}(r')\hat{\psi}_\sigma(r), \tag{2.66}$$

$$\hat{U}_{ep} = \sum_{\mathbf{q}\nu\sigma} (\hat{b}_{\mathbf{q}\nu} + \hat{b}^\dagger_{-\mathbf{q}\nu}) \int d^3r \hat{\psi}^\dagger_\sigma(r) V_{\mathbf{q}\nu}(r) \hat{\psi}_\sigma(r). \tag{2.67}$$

We neglect

$$\begin{aligned}&-\sum_\sigma \int d^3r \hat{\psi}^\dagger_\sigma(r) V_{\rm eff}(r) \hat{\psi}_\sigma(r) + \iint d^3r d^3r' \{\hat{\psi}_\uparrow(r)\hat{\psi}_\downarrow(r')\Delta^*_{\rm eff}(r,r') + \hat{\psi}^\dagger_\downarrow(r')\hat{\psi}^\dagger_\uparrow(r)\Delta_{\rm eff}(r,r') \\ &-\sum_{RR'\tau\tau'} C^{\rm eff}_{R\tau\alpha R'\tau'\alpha'} \hat{U}_{R\tau\alpha}\hat{U}_{R'\tau'\alpha'}\end{aligned} \tag{2.68}$$

in the perturbation Hamiltonian because the first order perturbation from this part is canceled by $\Omega_{V_{\rm eff}} + \Omega_{\Delta_{\rm eff}} + \Omega_{C_{\rm eff}}$ in Eqs (2.48), (2.49), and (2.50). Then we consider diagrams represented in Fig. 2.3 as the perturbative contributions to $\Omega - \Omega_S$; this treatment is almost the same as that of Ref. [31]. Here, lines in the diagram represent the following Matsubara Green functions.

- The normal Green function [Fig. 2.4(a)]

$$G_{\sigma\sigma'}(r,r',\omega_n) \equiv -\int_{-\beta}^{\beta} d\tau \frac{1}{2} e^{i\omega_n\tau} \langle \hat{T}\hat{\psi}_\sigma(r,\tau)\hat{\psi}^\dagger_\sigma(r',0)\rangle_S \tag{2.69}$$

- The anomalous Green function [Fig. 2.4(b)]

$$F_{\sigma\sigma'}(r,r',\omega_n) \equiv -\int_{-\beta}^{\beta} d\tau \frac{1}{2} e^{i\omega_n\tau} \langle \hat{T}\hat{\psi}_\sigma(r,\tau)\hat{\psi}_\sigma(r',0)\rangle_S \tag{2.70}$$

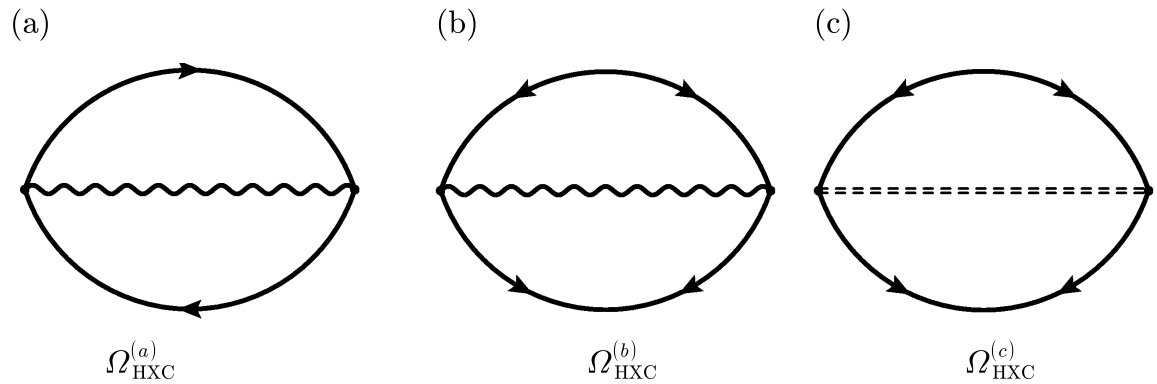

Figure 2.3: Diagrams for the Hartree-exchange-correlation grand potential $\Omega_{\rm HXC}$. Contributions from diagrams (a), (b), and (c) are represented in Eqs. (2.72), (2.73), and (2.74), respectively.

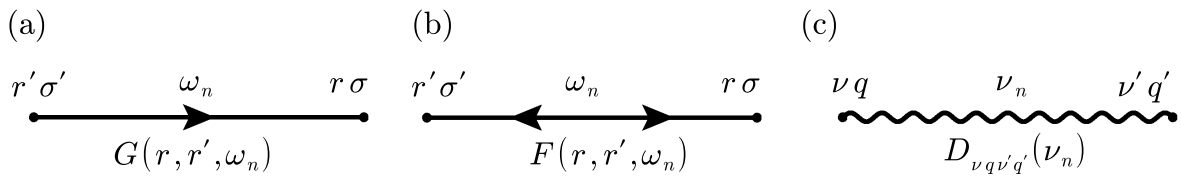

Figure 2.4: (a) normal , (b) anomalous, and (c)phonon Matsubara Green's function of the Kohn-Sham system represented in Eqs. (2.69), (2.70), and (2.71), respectively.

- The phonon Green function [Fig. 2.4(c)]

$$D_{\nu q \nu' q'}(\nu_n) \equiv \int_0^\beta d\tau e^{i\nu_n \tau} \langle \hat{T}\{\hat{a}_{\nu q}(\tau) + \hat{a}^\dagger_{\nu -q}(\tau)\}\{\hat{a}_{\nu' q'}(0) + \hat{a}^\dagger_{\nu' -q'}(0)\}\rangle_S \tag{2.71}$$

The dashed double line in Fig. 2.3 (c) indicates the screened Coulomb interaction $V_{\rm scr}(r, r', i\omega)$ explained in the next section.

Contributions of the diagrams represented in Fig. 2.3 are calculated as follows:

$$\Omega^{(a)}_{\rm HXC} = \frac{1}{2\beta^2} \sum_{\sigma\sigma'} \sum_{lm} \sum_{\nu q \nu' q'} \iint d^3r d^3r' G_{\sigma\sigma'}(r, r', \omega_l) G_{\sigma'\sigma}(r', r, \omega_m) D_{\nu q \nu' q'}(\omega_l - \omega_m) V_{\mathbf{q}\nu}(r) V_{\mathbf{q}'\nu'}(r'), \tag{2.72}$$

$$\Omega^{(b)}_{\rm HXC} = \frac{1}{2\beta^2} \sum_{\sigma\sigma'} \sum_{lm} \sum_{\nu q \nu' q'} \iint d^3r d^3r' F_{\sigma\sigma'}(r, r', \omega_l) F^*_{\sigma'\sigma}(r', r, \omega_m) D_{\nu q \nu' q'}(\omega_l - \omega_m) V_{\mathbf{q}\nu}(r) V_{\mathbf{q}'\nu'}(r'), \tag{2.73}$$

$$\Omega^{(c)}_{\rm HXC} = \frac{1}{2\beta^2} \sum_{\sigma\sigma'} \sum_{lm} \iint d^3r d^3r' F_{\sigma\sigma'}(r, r', \omega_l) F^*_{\sigma'\sigma}(r', r, \omega_m) V_{\rm scr}(r, r', \omega_l - \omega_m), \tag{2.74}$$

where $V_{\rm scr}$ is the screened Coulomb interaction explained later. With this approximation for $\Omega_{\rm HXC}$, we obtain the gap equation as

$$\Delta_{nk} = -\frac{1}{2} \sum_{n'k'} \frac{K^{\rm ep}_{nkn'k'} + K^{\rm ee}_{nkn'k'}}{1 + Z_{nk}} \tanh\left(\frac{\beta \varepsilon_{n'k'}}{2}\right) \frac{\Delta_{n'k'}}{\varepsilon_{n'k'}}, \tag{2.75}$$

where

$$Z_{nk} = \frac{1}{\Delta_{nk}} \frac{\delta \Omega^{(a)}_{\rm HXC}}{\delta \chi^*_{nk}}\bigg|_{\Delta=0}$$
$$= \frac{-1}{\tanh(\beta\xi/2)} \sum_{n'k'\nu} |g^{k'-k\nu}_{n'k'nk}|^2 \{J(\xi_{nk}, \xi_{n'k'}, \omega_{(k'-k)\nu}) + J(\xi_{nk}, -\xi_{n'k'}, \omega_{(k'-k)\nu})\}, \tag{2.76}$$

$$K^{\rm ep}_{nkn'k'} = \frac{\delta^2 \Omega^{(b)}_{\rm HXC}}{\delta \chi^*_{nk} \delta \chi_{n'k'}}\bigg|_{\Delta=0}$$
$$= \frac{2}{\tanh(\beta\xi/2)\tanh(\beta\xi'/2)} \sum_{\nu} |g^{k'-k\nu}_{n'k'nk}|^2 \{I(\xi_{nk}, \xi_{n'k'}, \omega_{(k'-k)\nu}) - I(\xi_{nk}, -\xi_{n'k'}, \omega_{(k'-k)\nu})\} \tag{2.77}$$

$$K^{\rm ee}_{nkn'k'} = \frac{\delta^2 \Omega^{(c)}_{\rm HXC}}{\delta \chi^*_{nk} \delta \chi_{n'k'}}\bigg|_{\Delta=0}$$
$$= \frac{2}{\pi} \int_0^\infty d\omega \frac{|\xi_{nk}| + |\xi_{n'k'}|}{(|\xi_{nk}| + |\xi_{n'k'}|)^2 + \omega^2} \iint d^3r d^3r' \varphi^*_{nk}(r) \varphi^*_{n'k'}(r') V_{\rm scr}(r, r', \omega) \varphi_{nk}(r') \varphi_{n'k'}(r), \tag{2.78}$$

and

$$I(\xi, \xi, \omega) = \tilde{I}(\xi, \xi', \omega) - \tilde{I}(\xi, \xi', -\omega), \tag{2.79}$$
$$\tilde{I}(\xi, \xi', \omega) = \frac{f(-\xi)f(\xi')n(\omega) + f(\xi)f(-\xi')n(-\omega)}{\xi - \xi' - \omega}, \tag{2.80}$$
$$J(\xi, \xi, \omega) = \tilde{J}(\xi, \xi', \omega) - \tilde{J}(\xi, \xi', -\omega), \tag{2.81}$$
$$\tilde{J}(\xi, \xi', \omega) = -\frac{f(\xi) - n(\omega)}{\xi - \xi' - \omega} \left[\frac{f(\xi') - f(\xi - \omega)}{\xi - \xi' - \omega} - \beta f(\xi - \omega) f(\omega - \xi) \right]. \tag{2.82}$$

We have neglected the temperature dependence of Eq. (2.74) to obtain (2.78).

2.4.3 The screened Coulomb interaction

$V_{\rm scr}(r, r')$ in the XC kernel (2.78) indicates the screened Coulomb interaction with density functional theory for the normal state;

$$V_{\rm scr}(r, r', \omega) = \frac{1}{|r - r'|} + \iint d^3r_1 d^3r_2 \left(\frac{1}{|r - r_1|} + \frac{\delta^2 E_{\rm XC}}{\delta\rho(r)\delta\rho(r_1)} \right) \Pi(r_1, r_2, \omega) \frac{1}{|r_2 - r'|} \tag{2.83}$$

where $\Pi(r, r', \omega)$ is the polarization function

$$\Pi(r, r', \omega) = \Pi_0(r, r', \omega) + \iint d^3r_1 d^3r_2 \Pi_0(r, r_1, \omega) \left(\frac{1}{|r_1 - r_2|} + \frac{\delta^2 E_{\rm XC}}{\delta\rho(r_1)\delta\rho(r_2)} \right) \Pi(r_2, r', \omega), \tag{2.84}$$

and $\Pi_0(r, r', i\omega)$ is the polarization function of non-interacting system

$$\Pi_0(r, r', \omega) = \sum_{nkn'k'} \frac{f(\xi_{nk}) - f(\xi_{n'k'})}{\xi_{n'k'} - \xi_{nk} + i\omega} \varphi^*_{nk}(r) \varphi^*_{n'k'}(r') \varphi_{nk}(r') \varphi_{n'k'}(r). \tag{2.85}$$

Chapter 3

Numerical methods

In this chapter, we develop numerical methods to perform the SCDFT calculations.

3.1 Brillouin-zone integration

In this section, we explain the difficulty of the Brillouin-zone integration in calculations of phonons and response functions. Then we propose optimized tetrahedron method to overcome this difficulty. To prove the effectiveness of this method, we apply this method to the calculation of phonons and electron-phonon interactions in MgB_2 and fcc lithium. The contents in this section have been published in Physical Review B **89**, 094515 (2014).

3.1.1 Difficulty in the Brillouin-zone integration

In calculations of the electronic and phononic properties in periodic systems, integrals of k-dependent functions over the Brillouin zone (BZ) are evaluated to obtain various physical quantities. This integral with respect to the Bloch wave vector k is replaced with a summation over discrete k points. However, the integrand functions generally show rapid or even singular k-point dependence. Approximations for the functions are therefore imperative for actual calculations. Then, approximation schemes employed for this summation inevitably affect the accuracy of the calculation.

Specifically, there are two standard schemes to perform such an integration over the k points, namely, the broadening method[44] and the linear tetrahedron method[45]. In the broadening method, we replace the delta function with a smeared function which has a finite broadening width; this method corresponds to smearing the electronic spectrum; as a result, the effect of detailed electronic structure cannot be evaluated and the calculation suffers from the systematic error depending on the smearing width. In the linear tetrahedron method, we perform analytical integration in tetrahedral regions covering the BZ with the piecewise linear interpolation of a matrix element. Unlike the broadening method, with this method, we can in principle reach to the exact value by increasing the number of k points.

However, the linear tetrahedron method has a drawback; if the integrand function is a convex (concave) function of k, this method systematically overestimates (underestimates) its contribution to the integral due to the linear interpolation involved. Because of this, the linear tetrahedron method sometimes requires an impractically large number of k points for practical accuracy. Although this can be avoided by using the quadratic interpolation, we cannot perform analytical integration straightforwardly in such a case.

In YNi_2B_2C, the band structure observed in the previous studies [17, 46, 18] is highly complicated in the vicinity of the Fermi level. There are bands of various characters; some of

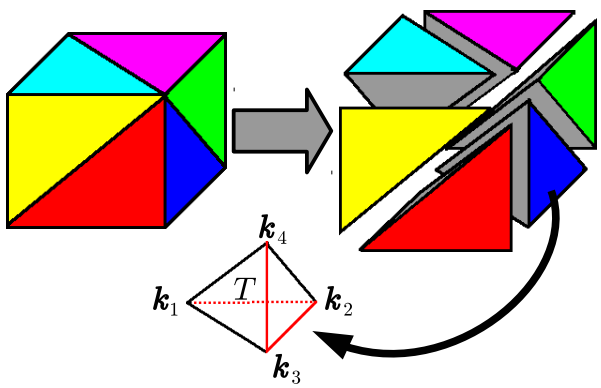

Figure 3.1: Sub-cell division into six tetrahedra and numbering of the tetrahedron corners; the red lines in the rightmost tetrahedron are the edges of the sub-cell.

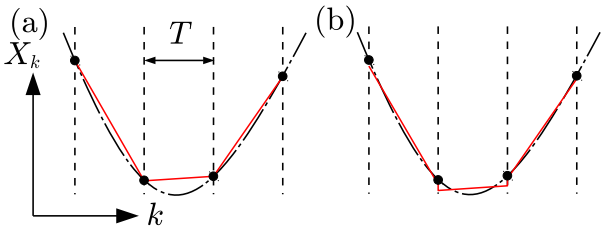

Figure 3.2: Two kinds of approximations of the matrix element. True and approximated matrix elements X_T are depicted as black dash-doted lines and red solid lines, respectively; the black points indicate the matrix elements X_k for a given value of k; the dashed lines indicate the boundaries of the tetrahedra. (a) The liner interpolated function X_T^1 is always smaller (larger) than the true function X_T in the case of a convex (concave) function. (b) The leveled linear function is a better approximation of the true function.

them are convex and others are concave. Some bands are very close to the Fermi level, but they do not cross the Fermi level. Bands having large curvatures make electron and hole pockets. In this situation, both of the broadening method and the linear tetrahedron method cause an error.

In this work, we develop the optimized tetrahedron method that is applicable to calculations involving integrations of functions with singularities on the Fermi surfaces. It is constructed by means of a higher-order interpolation and the least square method. We apply our method to the BZ integration in calculations of phonon frequencies based on density functional perturbation theory (DFPT) [40]. Specifically, the application is performed to MgB2 and fcc Li. For these systems, it has been known to be difficult to achieve convergence using the standard methods because the phonons in these materials couple strongly with electrons in the vicinity of Fermi surfaces [47, 48]. We demonstrate that our method successfully gives accurate results.

3.1.2 Linear tetrahedron method and its drawbacks

We overview the general procedure of the linear tetrahedron method and its drawbacks. We consider the integral

$$\int d^3k X_k F(\varepsilon_k), \tag{3.1}$$

on the basis of the linear tetrahedron method, where $F(\varepsilon_k)$ is a function of the orbital energy such as $\theta(\varepsilon_{\mathrm{F}} - \varepsilon_k)$, $\delta(\varepsilon_{\mathrm{F}} - \varepsilon_k)$, or $\theta(\varepsilon_{\mathrm{F}} - \varepsilon_k)/(\varepsilon_{\mathrm{F}} - \varepsilon_k)$. Here, $\theta(x)$ is the Heaviside step function. First, we divide a sub-cell into six tetrahedra (Fig. 3.1); this sub-cell is partitioned with the uniform k-point mesh; for convenience, we number the corners of each tetrahedron from 1 to 4

along specific edges of the sub-cell (see Fig. 3.1). The contribution of this tetrahedron (T) to the integral (3.1) is

$$6V_T \int_0^1 dx \int_0^{1-x} dy \int_0^{1-x-y} dz X_T(\boldsymbol{s}) F[\varepsilon_T(\boldsymbol{s})], \tag{3.2}$$

where $\boldsymbol{s} = (x, y, z)$, and

$$X_T(\boldsymbol{s}) \equiv X_{k_1^T(1-x-y-z)+k_2^T x+k_3^T y+k_4^T z}, \tag{3.3}$$

$$\varepsilon_T(\boldsymbol{s}) \equiv \varepsilon_{k_1^T(1-x-y-z)+k_2^T x+k_3^T y+k_4^T z}, \tag{3.4}$$

where k_i^T is the k point of the ith corner of T. In the linear tetrahedron method, we approximate X_T and ε_T with linear functions:

$$X_T^1(\boldsymbol{s}) = X_1(1-x-y-z) + X_2 x + X_3 y + X_4 z, \tag{3.5}$$

$$\varepsilon_T^1(\boldsymbol{s}) = \varepsilon_1(1-x-y-z) + \varepsilon_2 x + \varepsilon_3 y + \varepsilon_4 z, \tag{3.6}$$

where X_i and ε_i are the matrix element and the orbital energy at the ith corner, respectively. The integration (3.2) with Eqs. (3.5) and (3.6) is performed *analytically*.

However, linear interpolation has a drawback; if the matrix element $X_T(\boldsymbol{s})$ is a convex function within the tetrahedron T, the interpolated function $X_T^1(\boldsymbol{s})$ becomes $X_T^1(\boldsymbol{s}) \geq X_T(\boldsymbol{s})$ in T; hence, the integral is systematically overestimated. If $X_T(\boldsymbol{s})$ is a concave function, the sign of the inequality is reversed (see Fig. 3.2(a)).

3.1.3 Optimized tetrahedron method

The systematic error of the linear tetrahedron method is a result of the *linear interpolation*. Although we can avoid this problem if we use higher order interpolation, the integral (3.2) becomes unsolvable analytically; we have to improve on the *linear* approximation of the matrix elements. For this purpose, we employ *optimization* rather than interpolation (see Fig. 3.2 b). The procedure is explained as follows:

1. We construct the Nth-order polynomial $X_T^N(\boldsymbol{s})$ from X_k and k using the corners of a tetrahedron T and some additional surrounding points for sampling.

2. We fit a linear function

$$X_T^{\mathrm{LSM}}(\boldsymbol{s}) = \bar{A}_1(1-x-y-z) + \bar{A}_2 x + \bar{A}_3 y + \bar{A}_4 z \tag{3.7}$$

   into $X_T^N(\boldsymbol{s})$ through the least square method (LSM); that is to say, we solve

$$\frac{\partial}{\partial \bar{A}_i} \int_0^1 dx \int_0^{1-x} dy \int_0^{1-x-y} dz |X_T^N(\boldsymbol{s}) - X_T^{\mathrm{LSM}}(\boldsymbol{s})|^2 = 0. \tag{3.8}$$

3. We apply the same procedure to ε_k, and obtain $\varepsilon_T^{\mathrm{LSM}}(\boldsymbol{s})$.

4. We evaluate integral (3.2) replacing $X_T(\boldsymbol{s})$ and $\varepsilon_T(\boldsymbol{s})$ with $X_T^{\mathrm{LSM}}(\boldsymbol{s})$ and $\varepsilon_T^{\mathrm{LSM}}(\boldsymbol{s})$, respectively.

5. We repeat the above steps for all tetrahedra.

Although the approximated matrix element $X_T^{\mathrm{LSM}}(\boldsymbol{s})$ is discontinuous at boundaries of tetrahedra (see Fig. 3.2(b)), it is of no concern because we are interested only in the integrated value.

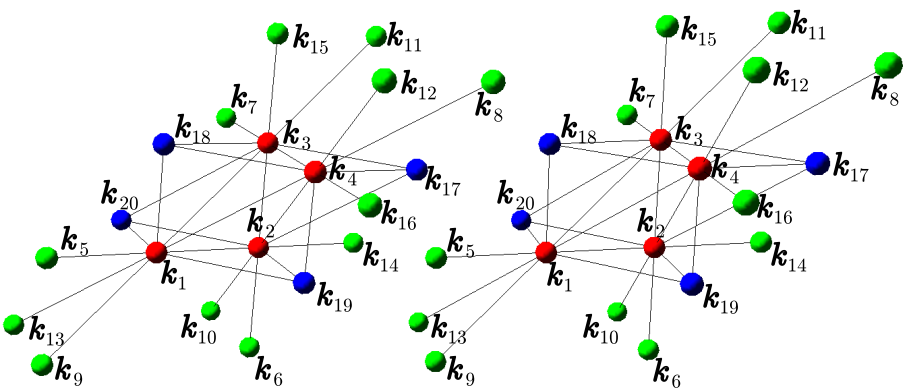

$$\boldsymbol{k}_5 = 2\boldsymbol{k}_1 - \boldsymbol{k}_2 \qquad \boldsymbol{k}_6 = 2\boldsymbol{k}_2 - \boldsymbol{k}_3$$
$$\boldsymbol{k}_7 = 2\boldsymbol{k}_3 - \boldsymbol{k}_4 \qquad \boldsymbol{k}_8 = 2\boldsymbol{k}_2 - \boldsymbol{k}_1$$
$$\boldsymbol{k}_9 = 2\boldsymbol{k}_1 - \boldsymbol{k}_3 \qquad \boldsymbol{k}_{10} = 2\boldsymbol{k}_2 - \boldsymbol{k}_4$$
$$\boldsymbol{k}_{11} = 2\boldsymbol{k}_3 - \boldsymbol{k}_1 \qquad \boldsymbol{k}_{12} = 2\boldsymbol{k}_4 - \boldsymbol{k}_2$$
$$\boldsymbol{k}_{13} = 2\boldsymbol{k}_1 - \boldsymbol{k}_4 \qquad \boldsymbol{k}_{14} = 2\boldsymbol{k}_2 - \boldsymbol{k}_1$$
$$\boldsymbol{k}_{15} = 2\boldsymbol{k}_3 - \boldsymbol{k}_2 \qquad \boldsymbol{k}_{16} = 2\boldsymbol{k}_4 - \boldsymbol{k}_3$$
$$\boldsymbol{k}_{17} = \boldsymbol{k}_4 - \boldsymbol{k}_1 + \boldsymbol{k}_2 \qquad \boldsymbol{k}_{18} = \boldsymbol{k}_1 - \boldsymbol{k}_2 + \boldsymbol{k}_3$$
$$\boldsymbol{k}_{19} = \boldsymbol{k}_2 - \boldsymbol{k}_3 + \boldsymbol{k}_4 \qquad \boldsymbol{k}_{20} = \boldsymbol{k}_3 - \boldsymbol{k}_4 + \boldsymbol{k}_1$$

Figure 3.3: Points for constructing a third order interpolation function (parallel stereogram). Red points denote the corners of T.

3.1.4 Implementation of the optimized tetrahedron method

We use a third order polynomial $X_T^3(\boldsymbol{s})$ as $X_T^N(\boldsymbol{s})$ in our implementation. The sampling points used to construct $X_T^3(\boldsymbol{s})$ are the corners of the tetrahedron T (4 points) and the other 16 points given in Fig. 3.3. As a result, $X_T^3(\boldsymbol{s})$ becomes

$$\begin{aligned}
X_T^3(\boldsymbol{s}) = {} & \frac{X_1}{2}u(u+1)(2-u) + \frac{X_2}{2}x(x+1)(2-x) + \frac{X_3}{2}y(y+1)(2-y) + \frac{X_4}{2}z(z+1)(2-z) \\
& - \frac{u^2x}{6}(2X_5 + X_{14}) - \frac{x^2y}{6}(2X_6 + X_{15}) - \frac{y^2z}{6}(2X_7 + X_{16}) - \frac{z^2u}{6}(2X_8 + X_{13}) \\
& - \frac{u^2y}{6}(2X_9 + X_{11}) - \frac{x^2z}{6}(2X_{10} + X_{12}) - \frac{y^2u}{6}(2X_{11} + X_9) - \frac{z^2x}{6}(2X_{12} + X_{10}) \\
& - \frac{u^2z}{6}(2X_{13} + X_8) - \frac{x^2u}{6}(2X_{14} + X_5) - \frac{y^2x}{6}(2X_{15} + X_6) - \frac{z^2y}{6}(2X_{16} + X_7) \\
& + (X_2 + X_4)xz(u+y) + (X_1 + X_3)uy(x+z) \\
& - \left(X_{17} + \frac{X_{10} + X_{12}}{2} + \frac{X_5 - X_{14}}{6} + \frac{X_{13} - X_8}{6}\right) xzu \\
& - \left(X_{18} + \frac{X_9 + X_{11}}{2} + \frac{X_6 - X_{15}}{6} + \frac{X_{14} - X_5}{6}\right) xyu \\
& - \left(X_{19} + \frac{X_{10} + X_{12}}{2} + \frac{X_7 - X_{16}}{6} + \frac{X_{15} - X_6}{6}\right) xyz \\
& - \left(X_{20} + \frac{X_9 + X_{11}}{2} + \frac{X_8 - X_{13}}{6} + \frac{X_{16} - X_7}{6}\right) yzu,
\end{aligned} \tag{3.9}$$

where $u = 1 - x - y - z$. By substituting it into (3.8), we obtain $X_T^{\mathrm{LSM}}(\boldsymbol{s})$:

$$\bar{A}_i = \sum_{j=1}^{20} P_{ij} X_{k_j}, \tag{3.10}$$

where

$$\mathbf{P} = (\mathbf{P}^{(1)}, \mathbf{P}^{(2)}, \mathbf{P}^{(3)}, \mathbf{P}^{(4)}, \mathbf{P}^{(5)}), \tag{3.11}$$

$$\mathbf{P}^{(1)} = \frac{1}{1260}\begin{pmatrix} 1440 & 0 & 30 & 0 \\ 0 & 1440 & 0 & 30 \\ 30 & 0 & 1440 & 0 \\ 0 & 30 & 0 & 1440 \end{pmatrix}, \tag{3.12}$$

$$\mathbf{P}^{(2)} = \frac{1}{1260}\begin{pmatrix} -38 & 7 & 17 & -28 \\ -28 & -38 & 7 & 17 \\ 17 & -28 & -38 & 7 \\ 7 & 17 & -28 & -38 \end{pmatrix} = {}^t\mathbf{P}^{(4)}, \tag{3.13}$$

$$\mathbf{P}^{(3)} = \frac{1}{1260}\begin{pmatrix} -56 & 9 & -46 & 9 \\ 9 & -56 & 9 & -46 \\ -46 & 9 & -56 & 9 \\ 9 & -46 & 9 & -56 \end{pmatrix}, \tag{3.14}$$

$$\mathbf{P}^{(5)} = \frac{1}{1260}\begin{pmatrix} -18 & -18 & 12 & -18 \\ -18 & -18 & -18 & 12 \\ 12 & -18 & -18 & -18 \\ -18 & 12 & -18 & -18 \end{pmatrix}. \tag{3.15}$$

We performe the same procedure for the orbital energy ε_k [1].

We can consider this procedure in a different way; when we calculate the contribution from a tetrahedron, we use the linear tetrahedron method after we have replaced matrix elements and orbital energies with those given in (3.10). Through this idea, we rewrite the integration (3.1) as

$$\int d^3k X_k F(\varepsilon_k) = \sum_k X_k w_k, \tag{3.16}$$

where the integration weight w_k is calculated as follows:

1. We divide the BZ into tetrahedra.

2. We calculate auxiliary orbital energies as

$$\bar{\varepsilon}_i = \sum_{j=1}^{20} P_{ij}\varepsilon_{k_j^T} \tag{3.17}$$

   for the corners of each tetrahedron.

3. We calculate the auxiliary weight $\bar{w}_i^T$ using the standard linear tetrahedron method with the auxiliary orbital energy (3.17).

4. The integration weight w_k is calculated as

$$w_k = \sum_T \sum_{i=1}^{4} \sum_{j=1}^{20} P_{ij}\bar{w}_i^T \delta(k - k_j^T). \tag{3.18}$$

[1] You do not have to type this compricated matrix in your source code when you implement the optimized tetrahedron method in your program; you just link libralies supplied by us (http://sourceforge.jp/projects/libtetrabz/).

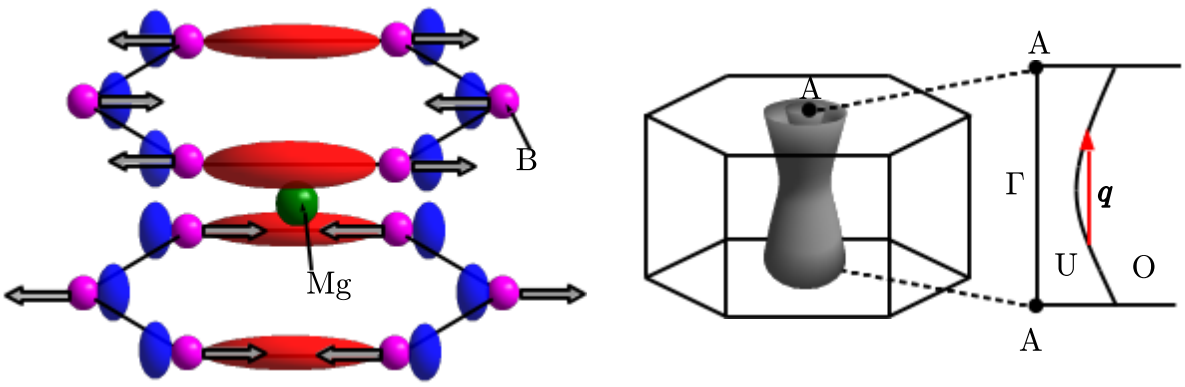

Figure 3.4: (left) Crystaline structure of MgB_2. Green and magenta spheres indicate Mg and B atoms, respectively. The σ orbital (blue and red isosurfaces of opposite signs.) and the displacement pattern of the intra-layer vibrational mode of the B atoms with wave number q at the A point (arrows) are also depicted. (right) Schematic illustration of the Fermi surfaces of the σ bands; the red arrow indicates the momentum vector of a phonon at the A point which connects occupied (O) and unoccupied (U) regions in the vicinity of the Fermi surface.

3.1.5 Comparison with other integration schemes for actual calculations

We implement our method in an first-principles electronic structure calculation code QUANTUM ESPRESSO[49, 50] which uses plane waves to represent Kohn-Sham orbitals. Then, we examine the effectiveness of the method through calculations of phonons in two materials, MgB_2 [51] and fcc lithium at a high pressure (20 GPa), based on DFPT [40]

Magnesium diboride has the highest T_c (about 40 K) of the known phonon-type superconductors under atmospheric pressure. Many *ab initio* studies have been performed since it was discovered [47, 52, 53, 54, 55], revealing that the high T_c is a result of the strong interaction between intra-layer vibrations of B atoms and their covalent bonding orbitals (σ bands) (Fig. 3.4). This strong electron-phonon coupling also softens phonon frequencies due to the screening of the ion-ion interaction; this screening occurs due to linear responses of σ electrons in the vicinity of the Fermi surfaces. We have to evaluate these responses accurately to determine the phonon frequencies precisely. Lithium exhibits a monatomic fcc structure at pressures between 7.5 and 39 GPa [56]. In this phase it becomes a superconductor. Its T_c increases with pressure up to 30 GPa [57, 58, 59] because of the enhancement of the electron-phonon interaction. The lower transverse acoustic (TA) mode at $q \approx K$ point couples with electrons most strongly in this material [48]. In this test, we consider the phonons of fcc Li at a pressure of 20 GPa.

We use norm-conserving pseudopotentials [60] in calculations of MgB_2; the cutoff energy of plane waves is set to 50 Ry. In the calculations of fcc lithium, we use an ultrasoft pseudopotential[61]. We treat the electrons in the 1s orbitals as valence electrons[62] and employ a cutoff energy of 80 Ry. In both of these applications, we use the GGA-PBE functional [38] and the first-order Hermite-Gaussian function [63, 44] for the broadening. We apply our method to the calculation of the frequency of the intra-layer vibrational mode of B atoms at the A point in the BZ (Fig. 3.5 top left). The result of the optimized linear tetrahedron method converges faster than that of the linear tetrahedron method; it converges with approximately 12^3 k points. If we use a broadening method with a small broadening width (0.01 Ry), the result converges at an unrealistically large number of k points (about 50^3 k points). On the other hand, using large broadening widths (0.03 Ry and 0.06 Ry), convergence occurs at a

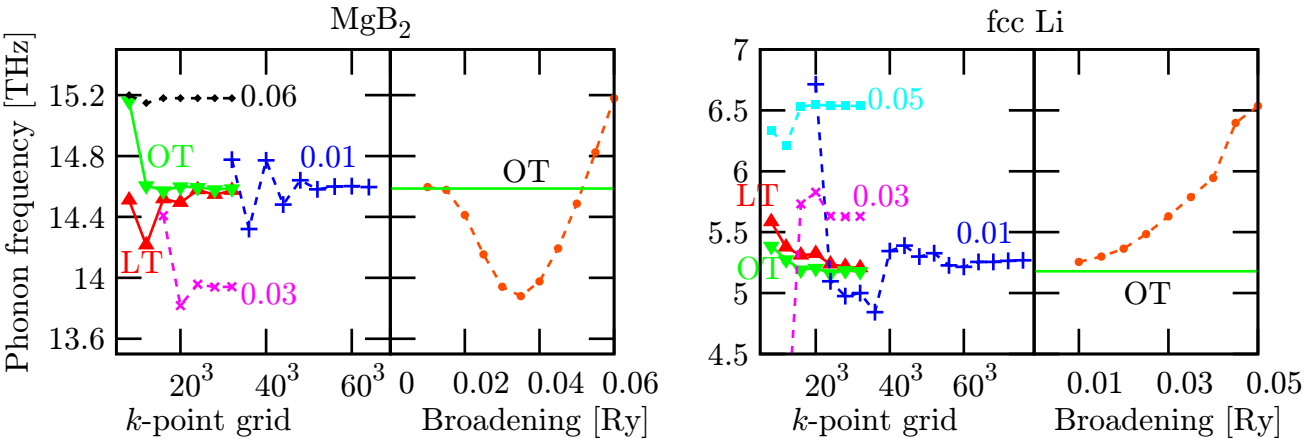

Figure 3.5: (left) The k convergences of the frequencies of the intra-layer vibrational mode of the B atoms at the A point in the BZ for MgB_2 (top) and the lower TA mode at the K point in the BZ for fcc Li at 20 GPa (bottom) with a different k integration method. ▲ and ▼ with red and green solid lines are the results of the linear and optimized linear tetrahedron methods; +, ×, ■, and ♦ with blue, magenta, cyan, and black dashed lines denote the results of the broadening method for widths of 0.01, 0.03, 0.05, and 0.06 Ry, respectively. Lines are guides for the eyes. (right) The frequency of these modes converged about the number of k at each broadening width (• with orange line); the green solid lines indicate the converged value obtained by our method.

lower number of k points. However, results are far away from the one converged about the broadening width; the complicated dependence of the convergence on the broadening width is shown in the top-right panel of Fig. 3.5. The result cannot be represented by a simple function, so it is difficult to extrapolate to a broadening width of zero.

The bottom left panel of Fig. 3.5 shows the k convergence of the lower TA mode at the K point in the BZ for fcc Li at 20 GPa calculated with the different integration schemes. Our method achieves convergence very quickly; it requires only 16^3 k points. In this system, the result of the broadening method is very sensitive to the broadening width; the error due to broadening is more than 25 % at a width of 0.05 Ry; hence, the broadening method is not suitable for this system.

We will show how the accuracy of the phonon calculations affects the prediction of the superconducting transition temperature within the framework of the following McMillan formula [64, 65]:

$$T_{\mathrm{c}} = \frac{\omega_{\log}}{1.2} \exp\left(\frac{-1.04(1+\lambda)}{\lambda - \mu^*(1+0.62\lambda)}\right). \tag{3.19}$$

Here,

$$\lambda = \sum_{q\nu} \lambda_{q\nu}, \qquad \log(\omega_{\log}) = \frac{1}{\lambda} \sum_{q\nu} \log(\omega_{q\nu}) \lambda_{q\nu}, \tag{3.20}$$

where

$$\lambda_{q\nu} = \sum_{knn'} \frac{2}{D(\varepsilon_{\mathrm{F}})\omega_{q\nu}} |g^{q\nu}_{n'k+qnk}|^2 \delta(\xi_{nk})\delta(\xi_{n'k+q}) \tag{3.21}$$

and $D(\varepsilon_{\mathrm{F}})$ is the density of states per spin at the Fermi energy. Although there are more precise methods to calculate T_{c} such as the density functional theory for superconductors [27, 41], we

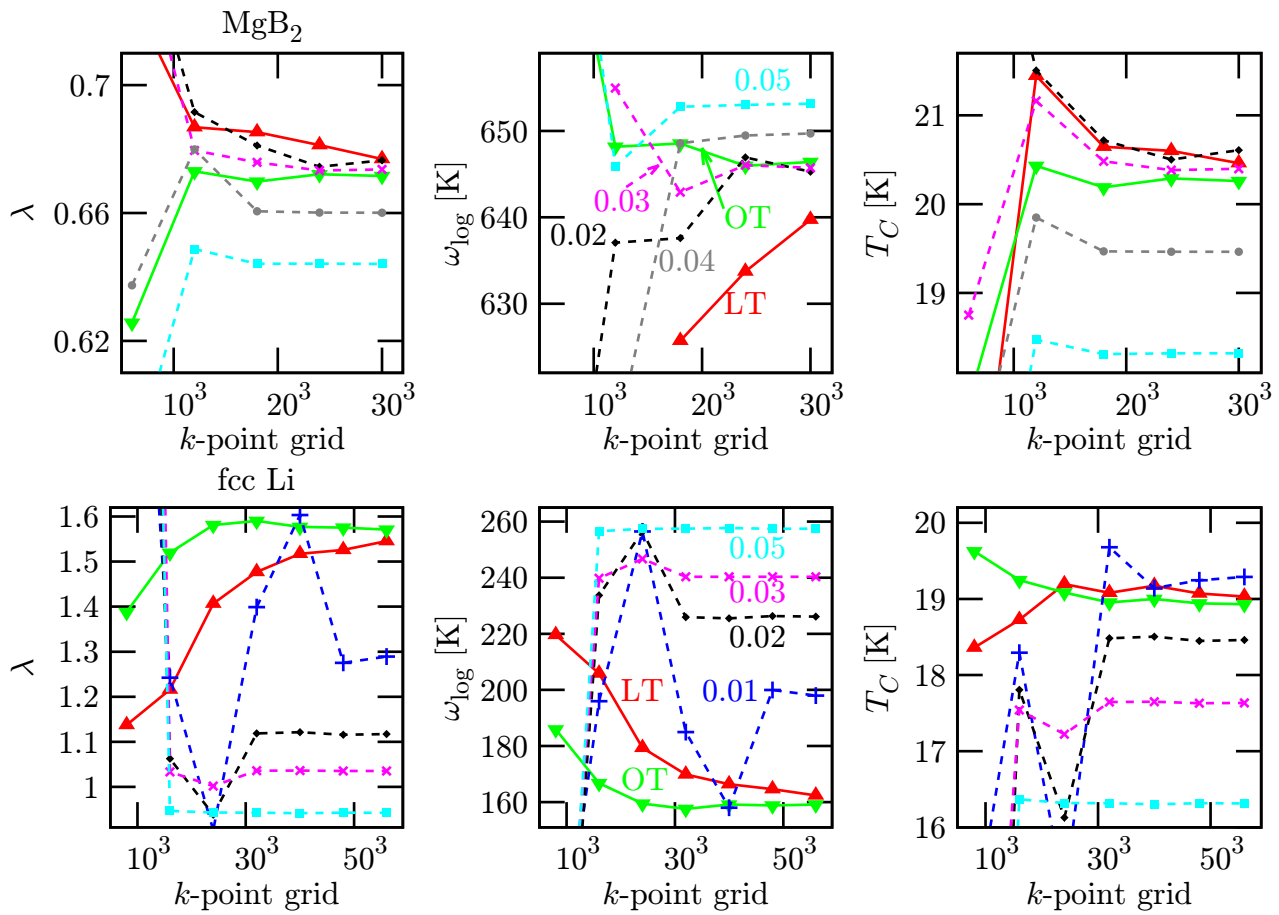

Figure 3.6: The k convergences of λ (top), $\omega_{\log}$ (middle), and T_c from the McMillan's formula (bottom) of MgB_2 (left) and fcc Li (right) calculated using $\omega_{q\nu}$ and $\delta v_S/\delta R_{\tau\alpha}(q)$ with different k integration schemes; ▲ and ▼ with red and green solid lines are the results of the linear and optimized linear tetrahedron methods; ♦, +, ×, ■, and • with gray, blue, magenta, black, and cyan dashed lines denote the results of broadening methods of widths 0.01, 0.02, 0.03, 0.04, and 0.05 Ry, respectively; lines are guides for the eyes.

use this simple formula because we are interested only in changes in the results due to the k integration in the phonon calculations.

To evaluate the integrals in (3.21), we use the linear tetrahedron method using a q grid of $6 \times 6 \times 4$ ($8 \times 8 \times 8$) and a k grid of $24 \times 24 \times 18$ ($32 \times 32 \times 32$) for MgB_2 (fcc Li), respectively. Additionally, we calculate each $\omega_{q\nu}$ and $V_{q\nu}(r)$ with different k grids and different k integration schemes.

Figure 3.6 shows the result of λ, $\omega_{\log}$, and T_c from the McMillan's formula ($\mu^* = 0.1$); in both the MgB_2 and Li cases, we obtain very fast k convergence using our method. Comparing the k-converged result of our method to that of the broadening method with a width of 0.05 Ry, we can see a large overestimate of the phonon frequencies occurs when the broadening method is used, resulting in an underestimated λ and an overestimated $\omega_{\log}$. Moreover, speeds of convergences about the broadening width for calculations of the λ and $\omega_{\log}$ are very slow; these results have not reach the convergence even for the broadening width of 0.01 Ry; if we use smaller broadening width (such as 0.005 Ry), we need an unrealistic number of k points to obtain the k-converged result.

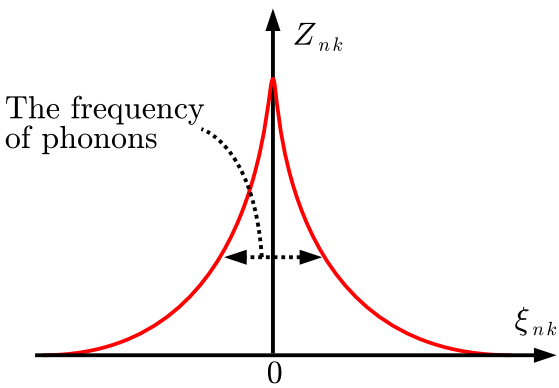

Figure 3.7: Schematic illustration of the energy dependence of Z_{nk}

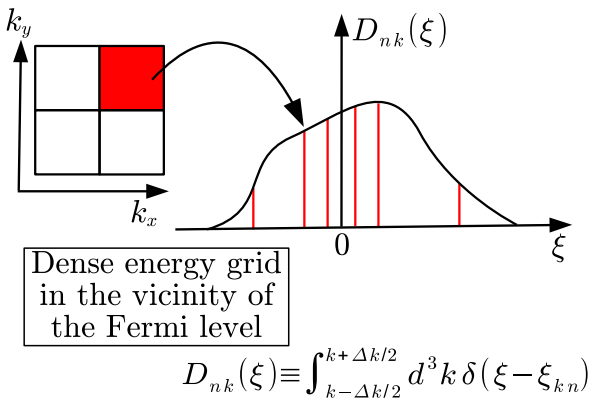

Figure 3.8: Schematic illustration of the auxiliary energy grid.

3.2 Integrations in the gap equation

In this section, we explain the numerical procedure to perform the integration in the gap equation (2.75).

3.2.1 Difficulty in the calculation of the gap equation

The renormalization factor Z_{nk}, the electron-phonon XC kernel $K^{\rm ep}_{nkn'k'}$, and the electron-electron XC kernel $K^{\rm ee}_{nkn'k'}$ vary rapidly in the vicinity of Fermi surfaces. The reason of this rapid variation is strong energy (ξ_{nk}, $\xi_{n'k'}$) dependence of Z_{nk}, $K^{\rm ep}_{nkn'k'}$, and $K^{\rm ee}_{nkn'k'}$ when $|\xi_{nk}|$ and $|\xi_{n'k'}|$ are equal to or lower than the phonon frequency (Fig. 3.7); because of this strong energy dependence, we have to trace the small energy variation (about the phonon frequency) in the vicinity of the Fermi level; therefore, we have to use an unrealistically large number of k points to solve the Kohn-Sham gap equation with the uniform grid.

In the previous works [28], randomly sampled k points have been used to perform the k integration in the gap equation; they adopt a large number of k points in the vicinity of Fermi surfaces. However, their method yields a numerical error because of the random sampling.

3.2.2 Auxiliary gap function

To avoid this difficulty, we develop an alternative method free from the randomness. We decouple the k dependence and energy dependence with a help of the auxiliary energy grid. Specifically, we define explicitly energy dependent auxiliary functions

$$\Delta_{nk}(\xi) \equiv -\frac{1}{2}\sum_{n'k'} K_{nkn'k'}(\xi, \xi_{n'k'}) \tanh\left(\frac{\beta\varepsilon_{n'k'}}{2}\right)\frac{\Delta_{n'k'}}{\varepsilon_{n'k'}}, \tag{3.22}$$

$$Z_{nk}(\xi) \equiv \frac{-1}{\tanh(\beta\xi/2)}\sum_{n'k'\nu} |g^{k'-k\nu}_{n'k'nk}|^2 \{J(\xi, \xi_{n'k'}, \omega_{(k'-k)\nu}) + J(\xi, -\xi_{n'k'}, \omega_{(k'-k)\nu})\}, \tag{3.23}$$

$$K^{\rm ep}_{nkn'k'}(\xi, \xi') \equiv \frac{2}{\tanh(\beta\xi/2)\tanh(\beta\xi'/2)}\sum_{\nu} |g^{k'-k\nu}_{n'k'nk}|^2 \{I(\xi, \xi', \omega_{(k'-k)\nu}) - I(\xi, -\xi', \omega_{(k'-k)\nu})\}, \tag{3.24}$$

$$K^{\rm ee}_{nkn'k'}(\xi, \xi') \equiv \frac{2}{\pi}\int_0^\infty d\omega \frac{|\xi| + |\xi'|}{(|\xi| + |\xi'|)^2 + \omega^2} \iint d^3r d^3r' \varphi^*_{nk}(r)\varphi^*_{n'k'}(r') V_{\rm scr}(r, r', i\omega)\varphi_{nk}(r')\varphi_{n'k'}(r), \tag{3.25}$$

where $K_{nkn'k'}(\xi,\xi') \equiv \{K^{\rm ep}_{nkn'k'}(\xi,\xi') + K^{\rm ee}_{nkn'k'}(\xi,\xi')\}/Z_{nk}(\xi)$. These functions are smooth function of k. They satisfy

$$\Delta_{nk}(\xi_{nk}) = \Delta_{nk}, \quad Z_{nk}(\xi_{nk}) = Z_{nk}, \quad K^{\rm ep}_{nkn'k'}(\xi_{nk},\xi_{n'k'}) = K^{\rm ep}_{nkn'k'}, \quad K^{\rm ee}_{nkn'k'}(\xi_{nk},\xi_{n'k'}) = K^{\rm ee}_{nkn'k'}. \tag{3.26}$$

Inserting $1 = \int d\xi' \delta(\xi - \xi_{n'k'})$ into Eq. (3.22), we obtain simultaneous equations for the auxiliary gap function

$$\Delta_{nk}(\xi) = -\frac{1}{2}\int d\xi' \sum_{n'k'} \delta(\xi' - \xi_{n'k'}) K_{nkn'k'}(\xi,\xi') \tanh\left(\frac{\beta\varepsilon_{n'k'}(\xi')}{2}\right)\frac{\Delta_{n'k'}(\xi')}{\varepsilon_{n'k'}(\xi')}, \tag{3.27}$$

where $\varepsilon_{nk}(\xi) \equiv \sqrt{|\Delta_{nk}(\xi)|^2 + \xi^2}$. We use smooth uniform k grid and dense non-uniform energy grid to solve this gap equation; the latter has much more points in the vicinity of $\xi = 0$ (Fig. 3.8).

Practically, the energy dependence becomes moderate when $\xi_{n'k'}$ is far from the Fermi level, we use this method only for bands crossing the Fermi level as

$$\begin{aligned}\Delta_{nk}(\xi) = -\frac{1}{2}\int_{\xi_{\min}}^{\xi_{\max}} d\xi' \sum_{n'}^{\rm Fermi}\sum_{k'} D_{n'k'}(\xi')\Delta_{n'k'}(\xi') K_{nkn'k'}(\xi,\xi') \tanh\left(\frac{\beta\varepsilon_{n'k'}(\xi')}{2}\right)\frac{\Delta_{n'k'}(\xi')}{\varepsilon_{n'k'}(\xi')} \\ -\frac{1}{2}\sum_{n'}^{\rm Other}\sum_{k'} K_{nkn'k'}(\xi,\xi_{n'k'}) \tanh\left(\frac{\beta\varepsilon_{n'k'}(\xi_{n'k'})}{2}\right)\frac{\Delta_{n'k'}(\xi_{n'k'})}{\varepsilon_{n'k'}(\xi_{n'k'})},\end{aligned} \tag{3.28}$$

where $\xi_{\max}$ and $\xi_{\min}$ are the maximum of the normal-state Kohn-Sham energy of bands crossing the Fermi level and minimum of that, and

$$D_{nk}(\xi) = \int_{\text{A surrounding region of } k} d^3k' \delta(\xi - \xi_{nk'}) \tag{3.29}$$

is the n- and k-dependent density of states calculated with a denser k grid (Fig. 3.9).

We use the following energy grid and the weight of the each point;

$$\xi_i = (x_i - x_{i_0})\varepsilon_{\min}\frac{n_\xi}{2}\exp\left[a\left(|x_i - x_{i_0}| - \frac{2}{n_\xi}\right)\right] \tag{3.30}$$

$$(d\xi)_i = (dx)_i(1 + a|x_i - x_{i_0}|)\varepsilon_{\min}\frac{n_\xi}{2}\exp\left[a\left(|x_i - x_{i_0}| - \frac{2}{n_\xi}\right)\right] \tag{3.31}$$

where n_ξ is the number of energy grid ($i = 1, 2, 3, \cdots, n_\xi$), x_i and $(dx)_i$ are the representative point and the weight in the Gauss-Legendre quadrature ($-1 < x_i < 1$). We choose i_0 from $i = 1, 2, \cdots, n_\xi$, so that the following factor is minimized:

$$\begin{aligned}&\left|\xi_{\max} - (1 - x_{i_0})\varepsilon_{\min}\frac{n_\xi}{2}\exp\left[a\left(1 - x_{i_0} - \frac{2}{n_\xi}\right)\right]\right| \\ &+\left|\xi_{\min} - (-1 - x_{i_0})\varepsilon_{\min}\frac{n_\xi}{2}\exp\left[a\left(1 + x_{i_0} - \frac{2}{n_\xi}\right)\right]\right|,\end{aligned} \tag{3.32}$$

where

$$a = \max\left[\frac{1}{1 - x_{i_0} - 2/n_\xi}\ln\left(\frac{\xi_{\max}}{(1 - x_{i_0})\varepsilon_{\min}n_\xi/2}\right), \frac{1}{1 + x_{i_0} - 2/n_\xi}\ln\left(\frac{-\xi_{\min}}{(1 + x_{i_0})\varepsilon_{\min}n_\xi/2}\right)\right]. \tag{3.33}$$

This energy grid has the following properties (see Fig. 3.10):

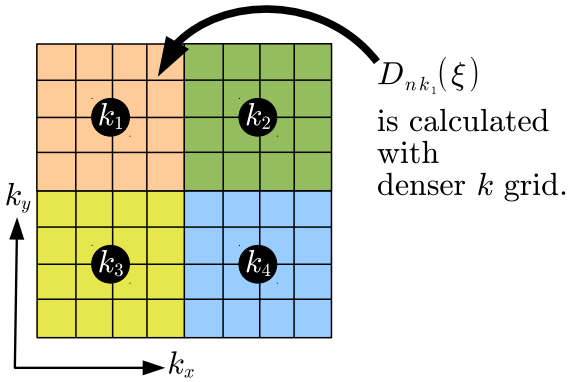

Figure 3.9: A schematic illustration of the calculation of $D_{nk}(\xi)$

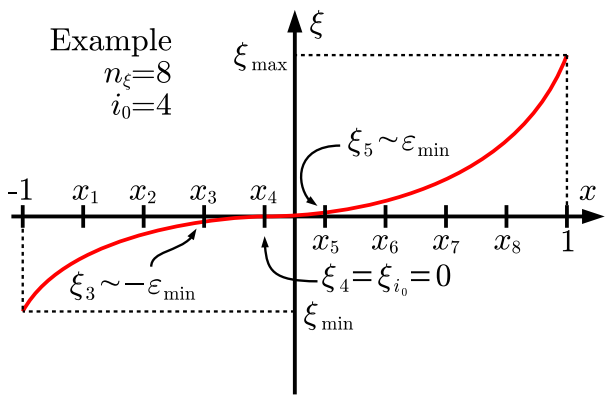

Figure 3.10: A schematic illustration of the energy grid.

1. It ranges between approximately $\xi_{\min}$ and $\xi_{\max}$.
2. The minimum energy scale is $\varepsilon_{\min}$.

Then, we can easily control the accuracy by tuning n_ξ and $\varepsilon_{\min}$.

3.3 The overall procedure

We perform calculations in this study as follows (Fig. 3.11); we use the optimized tetrahedron method for the Brillouin-zone integrations in all steps below except the step 4.

1. We perform first-principles structure optimization based on the density functional theory for the normal state, and obtain $\rho(r)$, $\varphi_{nk}(r)$, and $\xi_{nk}(r)$.
2. We calculate the screened coulomb interaction $V_{\rm scr}$ and the matrix element

$$V^{\rm C}_{nkn'k'}(\omega) = \iint d^3r d^3r' \varphi^*_{nk}(r)\varphi^*_{n'k'}(r') V_{\rm scr}(r,r',i\omega)\varphi_{nk}(r')\varphi_{n'k'}(r). \tag{3.34}$$

   We use the optimized tetrahedron method in the calculation of the polarization function $\Pi_0(r,r',i\omega)$.

3. We obtain phonon frequencies $\omega_{q\nu}$ and the deformation potential $V_{q\nu}(r)$ with density functional perturbation theory with the optimized tetrahedron method.
4. We calculate electron-phonon vertex function $g^{q\nu}_{n'k+qnk}$ with $\omega_{q\nu}$ and $V_{q\nu}(r)$.
5. We solve the gap equation

$$\begin{aligned}\Delta_{nk}(\xi) = &-\frac{1}{2}\int d\xi' \sum_{n'}^{\rm Fermi}\sum_{k'} \delta(\xi'-\xi_{n'k'}) K_{nkn'k'}(\xi,\xi') \tanh\left(\frac{\beta\varepsilon_{n'k'}(\xi')}{2}\right)\frac{\Delta_{n'k'}(\xi')}{\varepsilon_{n'k'}(\xi')} \\ &-\frac{1}{2}\sum_{n'}^{\rm Other}\sum_{k'} K_{nkn'k'}(\xi,\xi_{n'k'}) \tanh\left(\frac{\beta\varepsilon_{n'k'}(\xi_{n'k'})}{2}\right)\frac{\Delta_{n'k'}(\xi_{n'k'})}{\varepsilon_{n'k'}(\xi_{n'k'})},\end{aligned} \tag{3.35}$$

   from $\xi_{nk}(r)$, $V^{\rm C}_{nkn'k'}$, $\omega_{q\nu}$, and $g^{q\nu}_{n'k+qnk}$, and solve it self-consistently; then obtain $\Delta_{nk}(\xi)$.

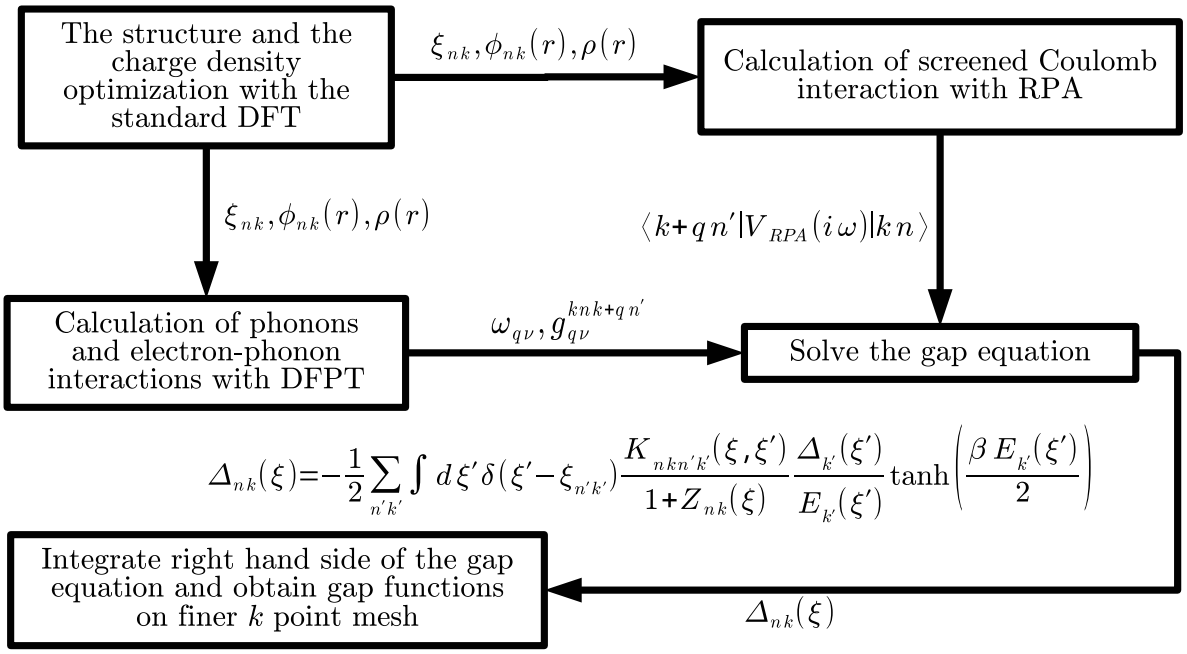

Figure 3.11: The overall procedure

6. We solve the gap equation at each temperature, and we obtain the transition temperature at which $\Delta_{nk}(\xi)$ becomes 0.

7. We integrate once the right hand side of the gap equation (do not solve self-consistently) with the original k' grid and a denser k grid and obtain $\Delta_{nk}(\xi)$ on the denser k grid; this $\Delta_{nk}(\xi)$ is used to calculate the quasiparticle density of states and the ultrasonic attenuation coefficients because we have to use dense k grid in these calculations.

Chapter 4

Result

In this chapter, at first, we show results of SCDFT calculations of Al, Nb, Ta, Mo, Pb, and MgB_2 by using our codes besides results of experimental and theoretical previous works; it is an verification of our codes. Next, we show our results of YNi_2B_2C: the band structure, Fermi surfaces, phonon dispersion, superconducting transition temperature, gap functions, quasiparticle DOS, and ultrasonic attenuation coefficients.

In this study, we use the DFT code Quantum ESPRESSO[49], which uses plane-waves and the pseudopotential to describe Kohn-Sham orbitals and the crystalline potential, respectively.

4.1 Verification of our code

We calculate superconducting transition temperatures of Al, Nb, Ta, Pb, and MgB_2 as a test of our program. We use ultrasoft pseudopotentials in Ref. [66]. We use LDA-PZ[36] and GGA-PBE[38] functional, ultrasoft pseudopotentials, We perform following $2 \times 3 = 6$ kinds of calculations per a system.

LDA/GGA We perform structure optimization and calculation of phonons by using LDA-PZ functional [36] and GGA-PBE functional [38].

Coulomb kernel in SCDFT We treat Coulomb interaction in the Coulomb kernel of SCDFT as the static (frequency independent) RPA level (sRPA) [32, 67, 68], dynamical (frequency dependent) RPA level (dRPA) [31], and the dynamical RPA + adiabatic LDA level (RPA+XC, see Chap. 2).

In the RPA+XC calculation with GGA-PBE functional, we use the XC kernel of LDA-PW functional [69] which is the local part of GGA-PBE functional. We use the 16^3 k grid for the structure/charge-density optimization and the phonon calculation; we calculate phonons on the 8^3 q grid; we set plane-wave cutoffs for Kohn-Sham orbitals in Al, Nb, Ta, Pb, and MgB_2 to 50 Ry, 50 Ry, 60 Ry, 50 Ry, and 50 Ry, respectively. Results are represented in Table 4.1.

4.2 Electronic structures of normal state

We perform calculations by using GGA-PBE [38] functional; we set the plane-wave cutoff for Kohn-Sham orbitals to 50 Ry; we use the ultrasoft pseudopotentials [61] in Ref. [72]. We also perform calculations by using LDA-PZ functional [36]; We represent those results as references only when it is necessary.

The numerical conditions and optimized lattice constants are in Table 4.2

The length of c axis is slightly underestimated and this underestimations is reported also in the previous study [17]. We use calculated lattice parameters in this study hereafter because we have found little difference between the calculated result (such as phonon frequencies) with theoretical (GGA-PBE) lattice parameters and that with experimental lattice parameters.

Table 4.1: Calculated lattice constants, λ, $\omega_{\ln}$, and T_c. We perform calculations by using GGA and LDA functional; we treat screened Coulomb interaction as the static RPA level (sRPA), the dynamical RPA level (dRPA), and the dynamical RPA + adiabatic LDA level(RPA+XC).

	Al	Nb	Ta	Pb	MgB_2
lattice constant a (LDA) [Å]	3.980	3.250	3.249	4.883	3.038
lattice constant a (GGA) [Å]	4.035	3.311	3.315	5.040	3.073
lattice constant a (experiment)[Å]	4.04	3.30	3.30	4.95	3.08
lattice constant c (LDA) [Å]	-	-	-	-	3.450
lattice constant c (GGA) [Å]	-	-	-	-	3.517
lattice constant c (experiment)[Å]	-	-	-	-	3.52
λ (LDA)	0.41	1.40	1.02	1.06	0.59
λ (GGA)	0.43	1.25	0.99	1.15	0.64
λ (previous work, LDA)	0.417 [31]	1.26 [28, 70]	0.86 [28, 70]	1.3 [68]	0.71 [67]
$\omega_{\ln}$ (LDA) [K]	295	137	145	65	724
$\omega_{\ln}$ (GGA) [K]	279	153	141	61	674
$\omega_{\ln}$ (previous work, LDA) [K]	314 [31]	185 [28, 70]	160 [28, 70]	-	-
T_c(LDA, sRPA) [K]	0.86	9.94	5.18	4.15	14.2
T_c(LDA, dRPA) [K]	2.61	14.7	8.08	5.40	21.2
T_c(LDA, RPA+XC) [K]	2.59	14.0	7.68	5.37	22.1
T_c(GGA, sRPA) [K]	1.00	9.14	4.52	4.32	19.1
T_c(GGA, dRPA) [K]	2.85	14.2	7.39	5.65	26.4
T_c(GGA, RPA+XC) [K]	2.85	13.3	6.97	5.62	27.2
T_c(LDA, sRPA, previous work)[K]	0.8 [31]	9.5[28]	3.7 [28]	5.25 [68]	22 [67]
T_c(LDA, dRPA, previous work)[K]	1.4 [31]	-	-	-	-
T_c(experimental) [71]	1.196	9.23	4.39	7.193	39

Table 4.2: Numerical conditions and results of the structure optimization in comparison with experimental data[73]. Crystalline structure is depicted in figure 4.1 (a).

k grid (structure optimization)	$12 \times 12 \times 12$
q grid (wavenumber of phonons)	$6 \times 6 \times 6$
k grid (density of states)	$40 \times 40 \times 40$
The number of bands (gap equation)	50 bands
The number of bands (polarization function Π_0)	50 bands
The number of points for energy grid n_ξ	100
ε_{min} in energy grid	10^{-6} Ry
lattice constant a [Å]	3.48 (LDA) / 3.51 (GGA) / 3.533 (Experiment)
lattice constant c [Å]	10.19 (LDA) / 10.31 (GGA) / 10.566 (Experiment)
B-C length [Å]	1.483 (LDA) / 1.494 (GGA) / 1.492 (Experiment)

Figure 4.2 shows the band structure of YNi_2B_2C [the k path is depicted in Fig. 4.1 (b)]. In this figure, we also depict contributions of the atomic orbitals of Y $4d$, Ni $3d$, B $2s2p$, and C $2s2p$ as the size of the symbols; that of Ni $3d$ is

$$p_{nk}^{\mathrm{Ni}3d} = \sum_{\tau=\mathrm{Ni1,Ni2}} \sum_{m} |\langle \varphi_{\tau dm} | \varphi_{nk} \rangle|^2. \tag{4.1}$$

We can see that the electronic states lying just below the Fermi level consist mainly of Ni $3d$

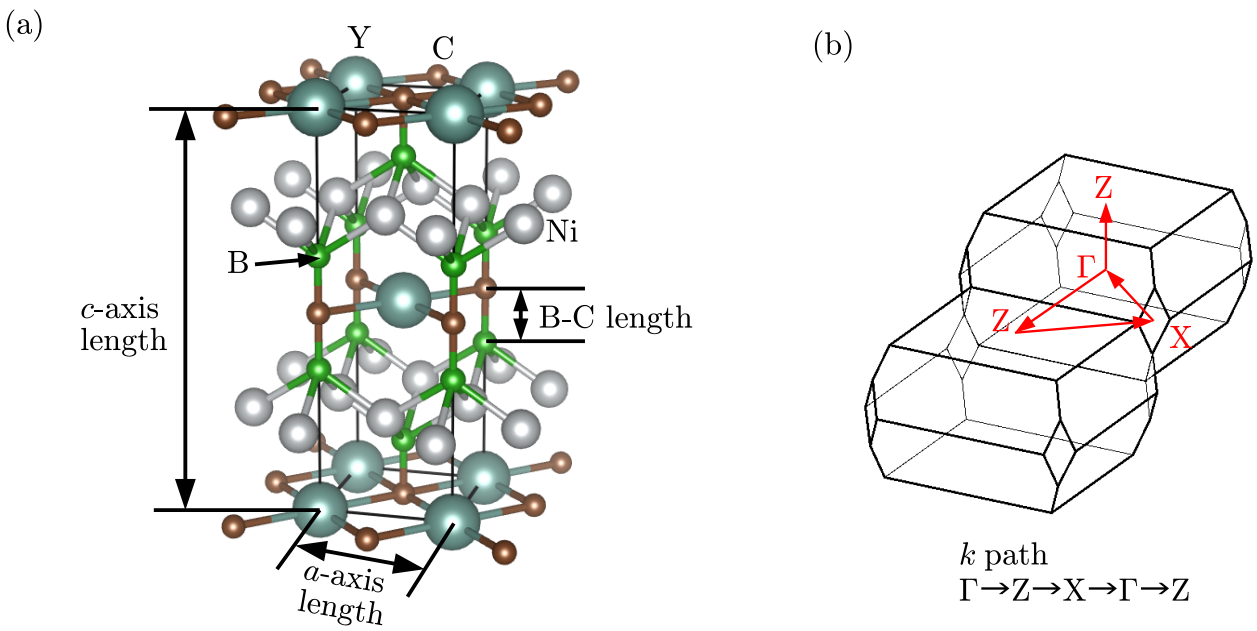

Figure 4.1: (a) Crystalline structure of YNi_2B_2C. (b) Brillouin zone and k path

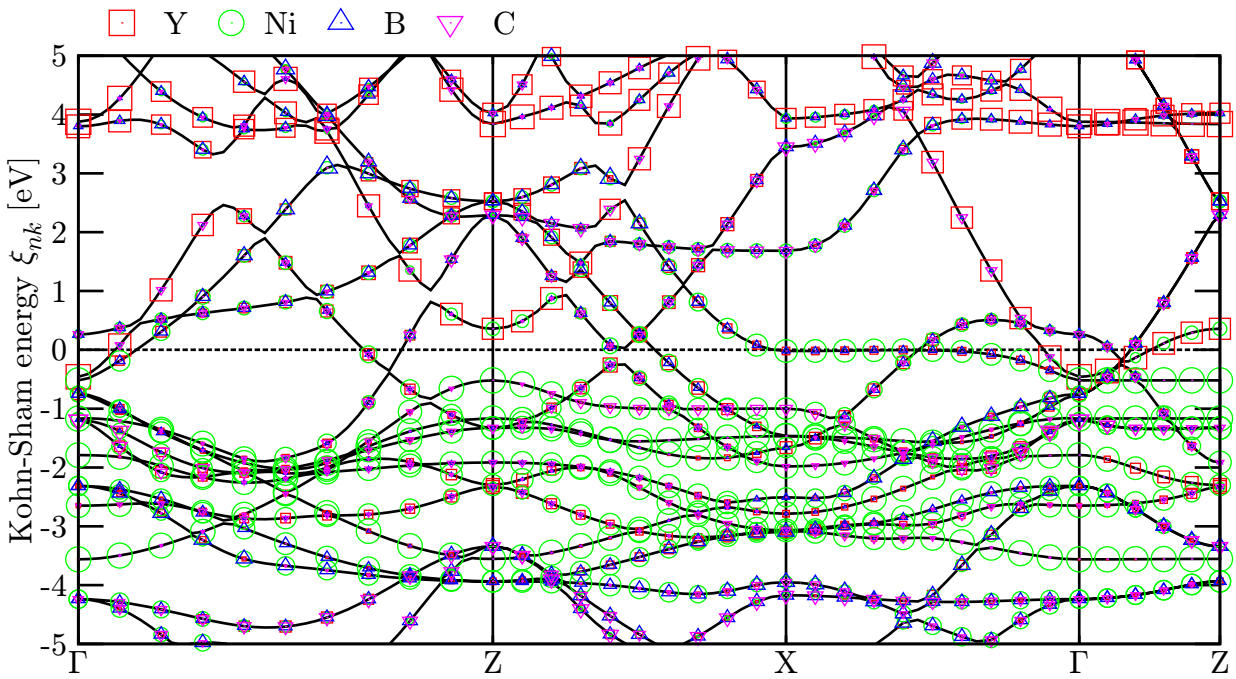

Figure 4.2: Electronic structure. Sizes of red squares, green circles, blue upward triangles, and magenta downward triangles indicate the amount of components of atomic orbitals of Y $4d$, Ni $3d$, B $2s2p$, and C $2s2p$, respectively.

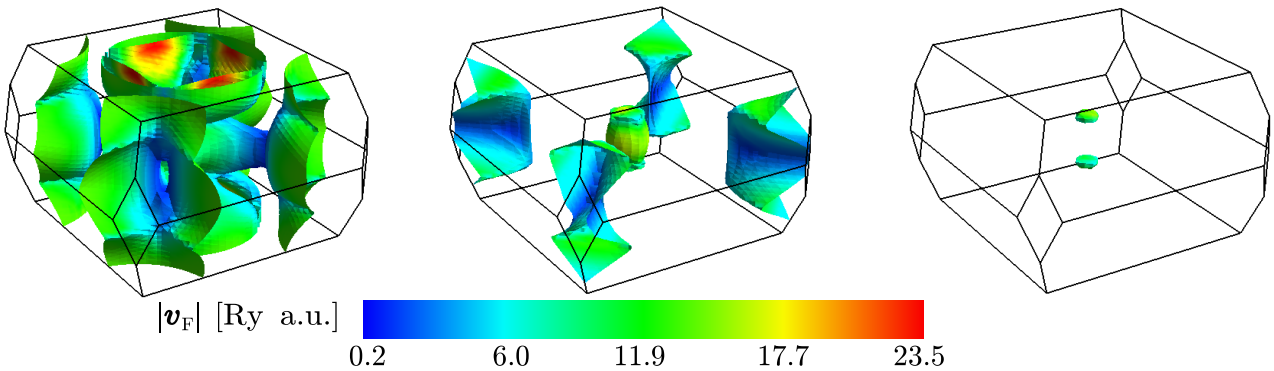

Figure 4.3: Fermi velocity of the electronic states on Fermi surfaces. The red, green, and blue region have a high, middle, and low Fermi velocity, respectively. This is depicted with our own visualization tool [74].

orbitals and those located just above the Fermi level have Y $4d$ character. There is a flat band near the Fermi level on the $X - \Gamma$ line; electronic states in this flat band consist mainly of Ni 3 d state. The total density of states at the Fermi level is 29 states per Ry, spin, and a unit cell; contributions from Y $4d$, Ni $3d$, B $2s2p$, and C $2s2p$ are 16.5%, 62.7%, 16.6%, and 4.2%, respectively. The large contribution from the Ni $3d$ orbital mainly comes from the flat band on the $X - \Gamma$ line.

Figure 4.3 shows the Fermi surfaces, on which we describe the Fermi velocity with a color plot. The magnitude of the Fermi velocity varies largely over Fermi surfaces; the ratio of the maximum and minimum of the Fermi velocity is about 100 ($v_{\mathrm{max}}/v_{\mathrm{min}} \sim 100$). We calculate the projections of the atomic orbitals Y $4d$, Ni $3d$, B $2s2p$, and C $2s2s$, to the electronic states on Fermi surfaces (Fig. 4.4). There is no regions dominated by B $2s2p$, and C $2s2p$ orbitals. Comparing Fig. 4.3 and Fig. 4.4, we found that the minimum of the Fermi velocity is in the regions where Ni $3d$ orbitals are dominant.

4.3 Phonons and electron-phonon interactions

We next calculated the phonon and electron-phonon interaction using the optimized tetrahedron method. First we confirm the effectiveness of this method with Fig. 4.5. Figure 4.5 shows the k and broadening width dependency of the calculated phonon frequency of the TA mode at $q = X$ point, which has been shown to depend strongly on the integration method [17]. It is clear that the optimized tetrahedron method yields a well-converged result, which cannot be achieved with the linear tetrahedron method. Also, our calculated value is free from the systematic error of more than 10% with the smearing method. The error of the latter originates from the following fact: In YNi_2B_2C, there are numerous bands which are located very near the Fermi energy but do not cross that (See Fig. 4.2). With the broadening method, these bands are treated as partially occupied, though they should be treated as perfectly occupied or unoccupied (Fig. 4.6). This treatment corresponds to calculating the phonon spectra with incorrect electronic charge density. Using the optimized tetrahedron method, we were able to avoid this error with the $12 \times 12 \times 12$ k-point grid.

We show calculated Raman-active phonon frequencies in Table 4.3. Results from a previous study of the Raman scattering experiment and the first-principles calculation with the all-electron full potential linear augmented plane wave (FLAPW) method and GGA-PBE functional are also shown. Our results show good agreement with both previous experimental and

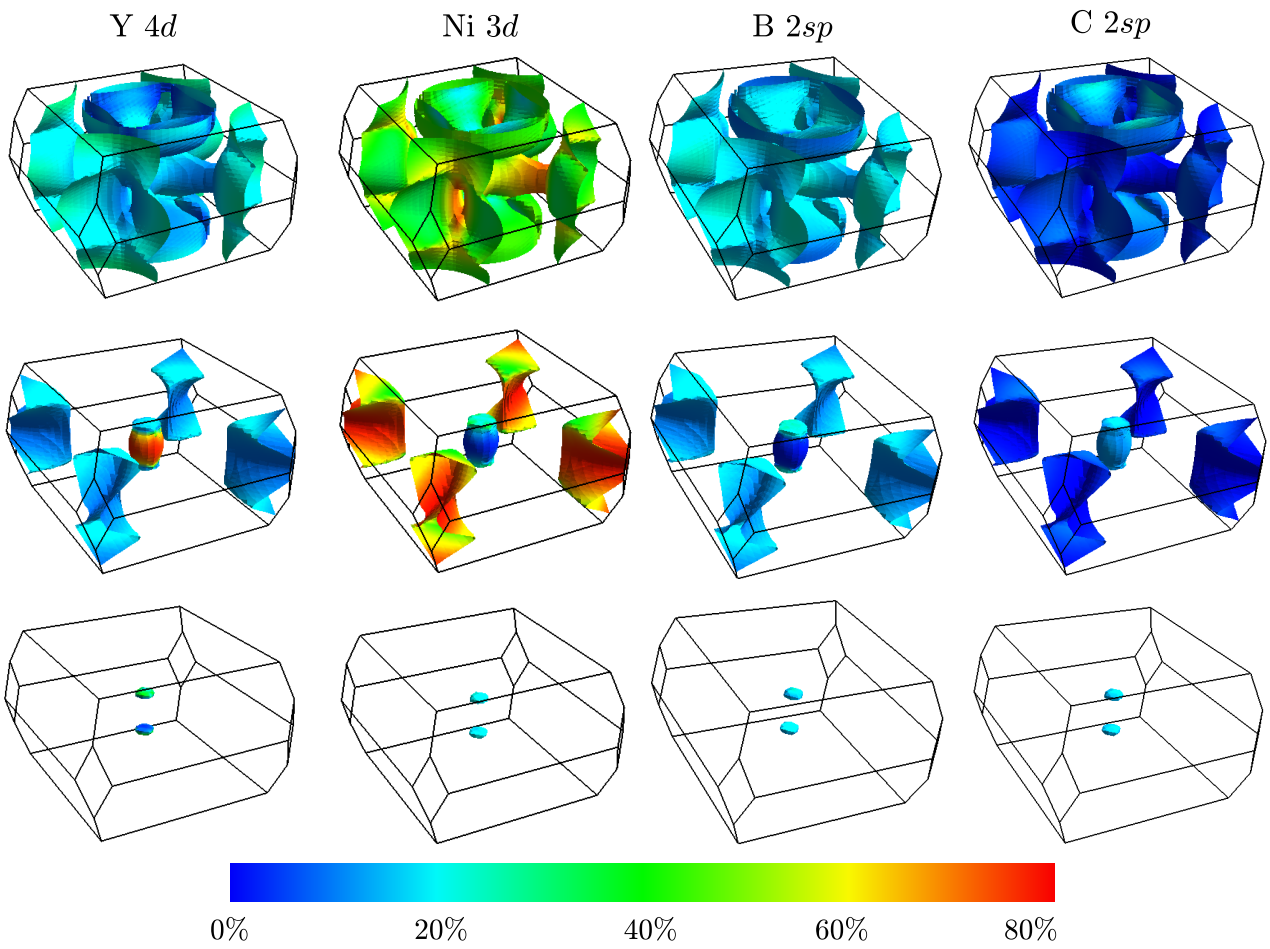

Figure 4.4: Projection of atomic orbitals on Fermi surfaces ($|\langle\varphi_{\mathrm{Atom}}|\varphi_{nk}\rangle|^2$).

Table 4.3: Calculated Raman-active phonon frequencies in cm^{-1} in comparison with those obtained in the previous theoretical work[46] with full potential linear augmented plane wave (FLAPW) method and GGA-PBE functional and experimental Raman-scattering measurements.

	This work	Previous (FLAPW)[46]	Previous (experiment)
Ni-B_{1g}	193	200	199[75], 198[76], 193[77]
Ni-E_g	279	271	287[75], 282 [76]
B-E_g	461	447	460[75], 470[76]
B-A_{1g}	836	821	813[75], 832[76], 823[77], 847[78]

theoretical results.

Calculated phonon dispersion is shown in Fig. 4.7. Calculated phonon frequencies agree with those observed with the neutron scattering measurement [17] except for the frequency of TA mode at $q \sim (0.55, 0, 0)$; although this mode shows strong softening in experiments, the softening obtained in our calculation is not so strong. We observe an imaginary mode in the vicinity of the Γ point; this indicate that long-period structure is preferred, but it is inconsistent with the realistic structure. This imaginary mode might be an artifact of the present approximation; we just neglect this because phonons with such a long wavelength does not affect the superconductivity. We also depict the electron-phonon coupling constant $\lambda_{q\nu}$

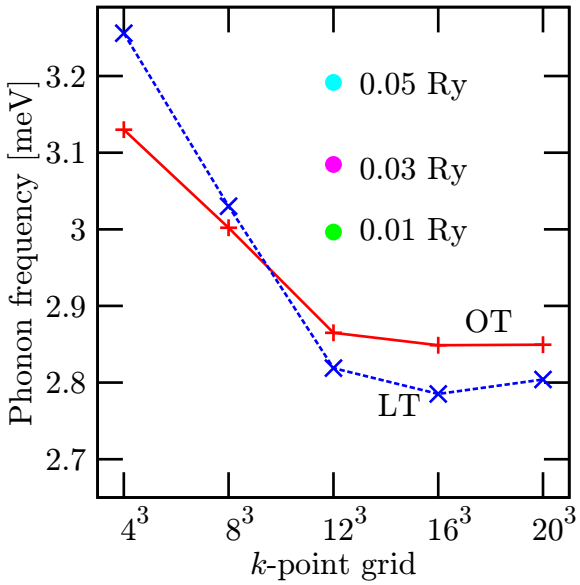

Figure 4.5: The k and broadening width dependency of the calculated phonon frequency of the TA mode at $q = X$ point. The red solid line and blue dashed line indicate results with the optimized tetrahedron method (OT) and with the linear tetrahedron method (LT), respectively. The Green, magenta, and cyan circles indicate the results with the broadening method; the broadening widths are 0.01 Ry, 0.03 Ry, 0.05 Ry, respectively.

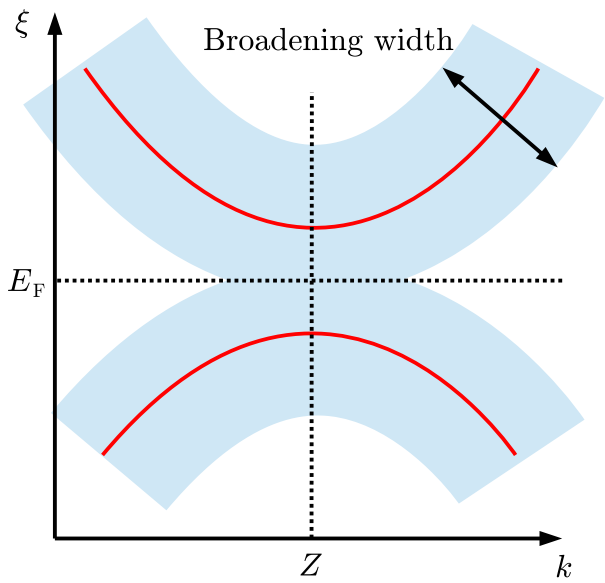

Figure 4.6: Schematic illustration of the broadening method. Red lines indicate bands in the vicinity of the Fermi surface at $k = Z$ point. Although these bands are not on the Fermi level in reality, we find these on the Fermi level when we use the broadening method.

(3.21) of each phonons as radii of circles; the TA mode has large electron-phonon interaction. The contribution from each atom to each phonon mode can be seen in Fig. 4.8; there is roughly six groups in this phonon dispersion:

- Three acoustic branches range from 0 meV to 30 meV.
- Y-dominant branches range from 10 meV to 25 meV.
- Ni-dominant branches range from 20 meV to 35 meV.
- B-C branches range from 35 meV to 60 meV.
- B-dominant branch at approximately 102 meV.
- A B-C branch at approximately 159 meV.

Non-dispersive branches at 102 meV and 159 meV are observed by the time-of-flight neutron spectroscopy experiment [79] in good agreement with our calculation.

The electron-phonon renormalization Z_{nk} (2.76) of electronic states on Fermi surfaces are shown in Fig. 4.9. This has large anisotropy and the ratio between the maximum of Z_{nk} and the minimum of the Z_{nk} is approximately 5; this ratio is close to the ratio previously determined with the combination of the dHvA experiment and the band structure calculation

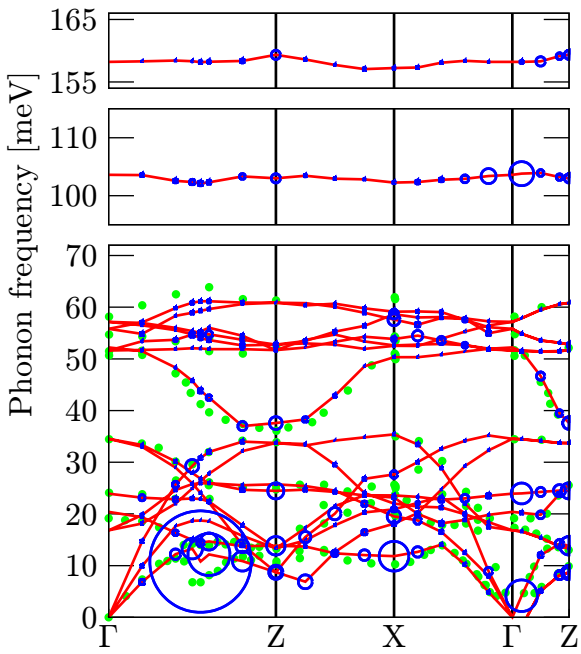

Figure 4.7: Phonon dispersion. The radii of circles indicate magnitude of $\lambda_{q\nu}$ (3.21). Green filled circles indicate results of the neutron diffraction [17].

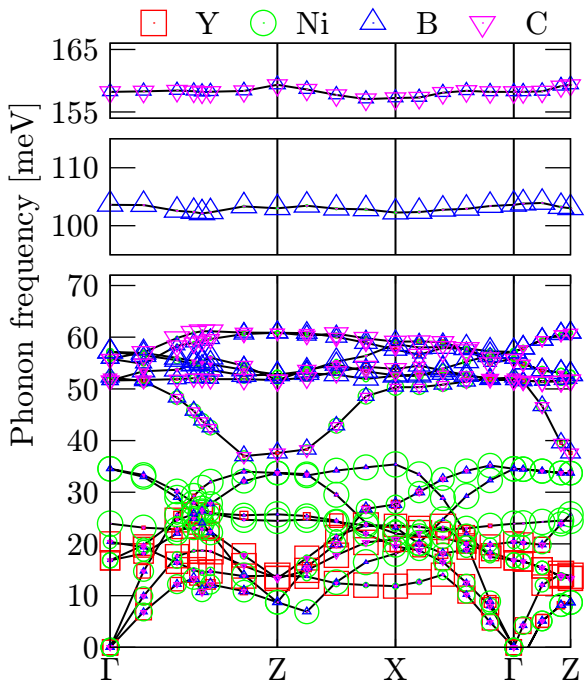

Figure 4.8: Phonon dispersion. Sizes of red squares, green circles, blue upward triangles, and magenta downward triangles indicate magnitude of components of Y, Ni, B, and C, respectively of the polarization $\eta_{q\nu}^{\tau\alpha}$ (2.21).

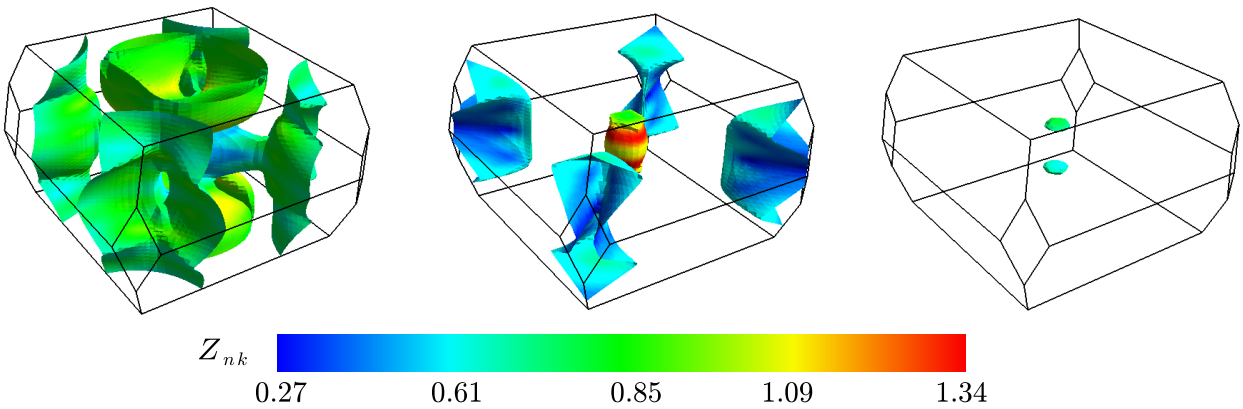

Figure 4.9: Electron-phonon renormalization Z_{nk} (2.76) on Fermi surfaces.

[18]. Comparing Fig. 4.4 and Fig. 4.9, we can see that the electronic states that have small Z_{nk} consist mainly of Ni $3d$ orbitals.

We obtain $lmabd = 0.72$, and $\omega_{\ln} = 270$ K (23.3 meV) by using GGA-PBE functional; we obtain $lmabd = 0.54$, and $\omega_{\ln} = 291$ K (25.1 meV) by using LDA-PZ functional.

4.4 Superconducting gaps and transition temperature

Now, we move on to the superconducting properties. We calculated the superconducting gap function at each temperature, and plot the superconducting gap averaged over the Fermi sur-

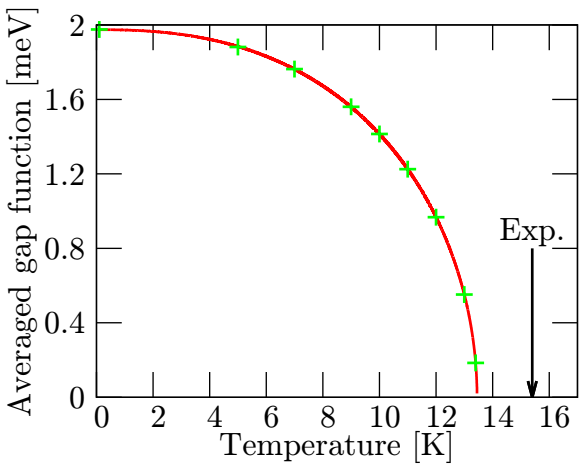

Figure 4.10: Calculated and experimental superconducting transition temperature. Green points indicate superconducting gaps averaged over Fermi surfaces; red line is a fit of averaged gaps with a function $\Delta(T) = \Delta_0\{1 - (T/T_c)^p\}^{1/q}$ via Δ_0, T_c, p, and q.

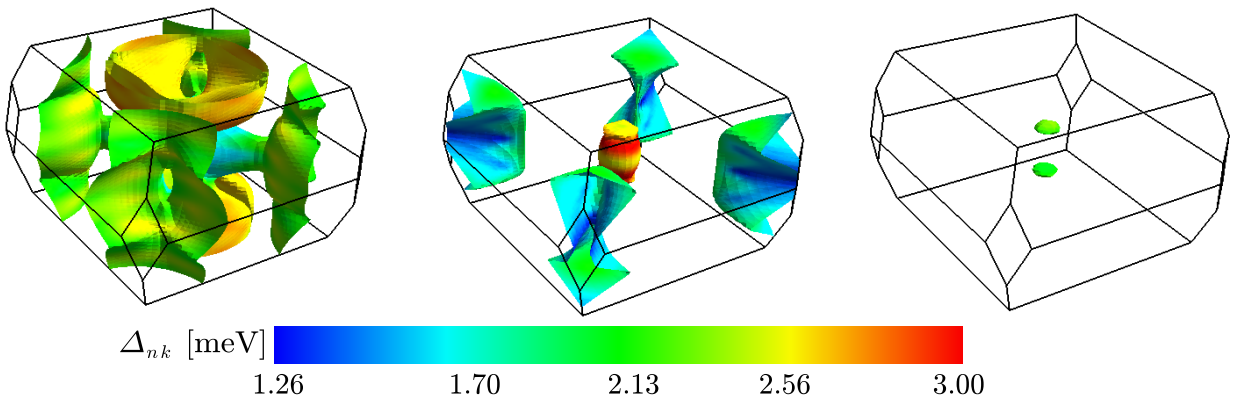

Figure 4.11: Superconducting gap functions Δ_{nk} on Fermi surfaces at 0.1 K.

faces at each temperature in Fig. 4.10; the calculated transition temperature where superconducting gaps disappear agrees well with the experimental value. On the other hand, we obtain $T_c = 8.73$ K when we use LDA-PZ functional.

We obtain calculated isotope effect exponent $\alpha = 0.16$; it agrees with experimental results [9, 10].

We depict superconducting gaps Δ_{nk} on Fermi surfaces at 0.1 K (calculation at the 0 K needs special treatment, and the result at 0 K and that at 0.1 K are almost the same; therefore we calculate at 0.1 K instead of the 0 K). As we expected, superconducting gaps of YNi_2B_2C is anisotropic; however, the degree of anisotropy is smaller than that of the electron-phonon renormalization; the ratio between the maximum and minimum of the gap functions on Fermi surfaces is 2.4 . This suppression of anisotropy might be due to the screened Coulomb interaction. Similar to the case of Z_{nk}, electronic states that have a small superconducting gap consist of Ni $3d$ orbitals.

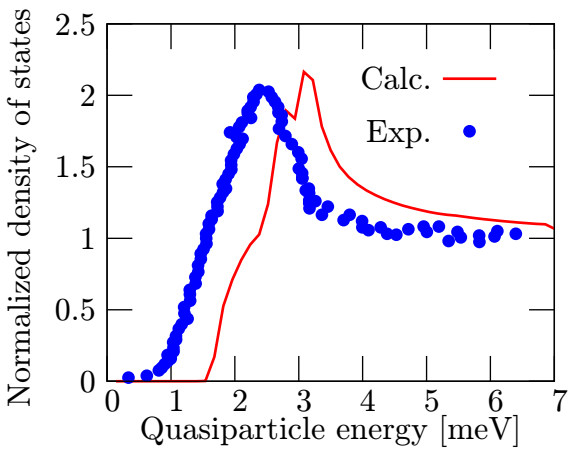

Figure 4.12: Calculated superconducting quasiparticle density of states at 0.1 K and experimental tunnel conductance spectrum at 0.5 K [14].

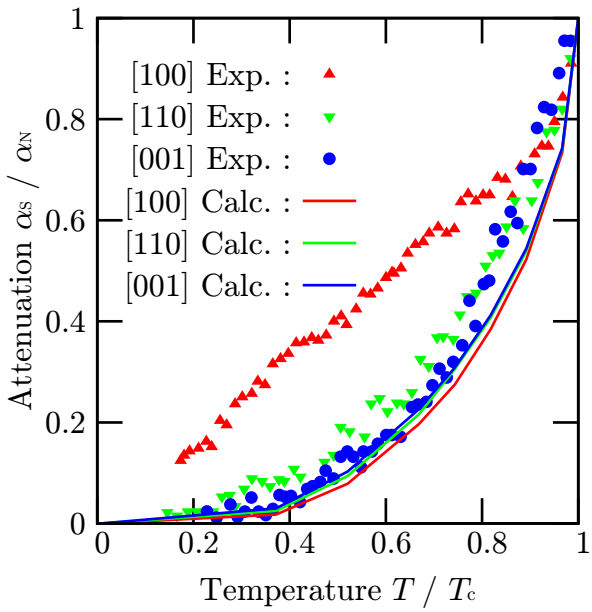

Figure 4.13: Calculated ultrasonic attenuation coefficients beside experimental results [15].

4.5 The QPDOS and the ultrasonic attenuation

Using the calculated k-dependent gap function, we next evaluated the quasiparticle density of states in the superconducting phase and ultrasonic attenuation coefficient, which are comparable with experiments. We calculated the quasiparticle density of states (QPDOS) D_{S} as

$$D_{\mathrm{S}}(\varepsilon) = \sum_{nk} \delta(\varepsilon - \varepsilon_{nk}) \tag{4.2}$$

$$= \sum_{nk} \int d\xi \delta(\xi - \xi_{nk}) \delta(\varepsilon - \varepsilon_{nk}(\xi)); \tag{4.3}$$

this four-dimensional ($\boldsymbol{k}$ and ξ) integration is performed by using the interpolation scheme which is similar to the tetrahedron method of the three dimensional integration. The calculated QPDOS is compared to the result of the tunnel-conductance experiment [14] (Fig. 4.12); although there is a visible discrepancy between the peak positions of the calculated QPDOS and the experimental spectrum, their whole shapes are in good agreement (Fig. 4.10).

Finally, we calculated the ultrasonic attenuation coefficient. It is written as [24]

$$\alpha = \sum_{nn'k} g^{q\nu}_{n'k+qnk} \left(1 + \frac{\xi_{nk}\xi_{n'k+q} - \Delta_{nk}\Delta_{n'k+q}}{E_{nk}E_{n'k+q}}\right) \{f(\varepsilon_{nk}) - f(\varepsilon_{n'k+q})\} \delta(\varepsilon_{n'k+q} - \varepsilon_{nk} - \omega_{q\nu}); \tag{4.4}$$

then by assuming $\omega_{q\nu} = v_\nu q$, we obtain

$$\alpha = \sum_{nn'k} g^{q\nu}_{n'k+qnk} \left(1 + \frac{\xi_{nk}\xi_{n'k+q} - \Delta_{nk}\Delta_{n'k+q}}{E_{nk}E_{n'k+q}}\right) \times \left\{-\frac{\partial f(\varepsilon_{nk})}{\partial \varepsilon_{nk}} v_\nu q\right\} \delta(\varepsilon_{n'k} + \nabla_k \varepsilon_{n'k} \cdot \boldsymbol{q} - \varepsilon_{nk} - v_\nu q). \tag{4.5}$$

Because phonon frequency and phonon wavenumber are very small, the inter band excitation is irrelevant; hence we assume $n' = n$, and obtain

$$\begin{aligned}\alpha &= \sum_{nk} g^{q\nu}_{nk+qnk}\left(1+\frac{\xi^2_{nk}-\Delta^2_{nk}}{\varepsilon^2_{nk}}\right)\left\{-\frac{\partial f(\varepsilon_{nk})}{\partial\varepsilon_{nk}}\right\}\delta\left(\frac{\nabla_k\varepsilon_{nk}\cdot\boldsymbol{\epsilon}_q}{v_\nu}-1\right)\\ &= \sum_{nk} g^{q\nu}_{nk+qnk}\frac{2\xi^2_{nk}}{\varepsilon^2_{nk}}\left\{-\frac{\partial f(\varepsilon_{nk})}{\partial\varepsilon_{nk}}\right\}\delta\left\{\frac{\boldsymbol{v}_{\mathrm{F},nk}\cdot\boldsymbol{\epsilon}_q}{v_\nu}\left(\frac{\xi_{nk}}{\varepsilon_{nk}}+\frac{\Delta_{nk}}{\varepsilon_{nk}}\frac{\partial\Delta_{nk}(\xi_{nk})}{\partial\xi_{nk}}\right)-1\right\},\end{aligned} \tag{4.6}$$

where $\boldsymbol{\epsilon}_q \equiv \boldsymbol{q}/q$ and $\boldsymbol{v}_{\mathrm{F},nk} = \nabla_k\xi_{nk}$. Although we can obtain ultrasonic attenuation coefficient from Eq. (4.6), we use more simplified one obtained with the following to do comparisons with previous reports.

- We assume that the velocity of the phonon is mach smaller than the Fermi velocity ($v_\nu \ll v_{\mathrm{F}}$).
- We assume that $\partial\Delta_{nk}(\xi_{nk})/\partial\xi_{nk} \ll 1$ in the vicinity of the Fermi level and $\Delta_{nk}/\varepsilon_{nk}$ rapidly decrease with increasing distance from the Fermi level. Therefore, we approximate

$$\frac{\Delta_{nk}}{\varepsilon_{nk}}\frac{\partial\Delta_{nk}(\xi_{nk})}{\partial\xi_{nk}} \sim 0 \tag{4.7}$$

- We assume that the electron-phonon interaction of the acoustic phonon with long wave number is insensitive to the band index n and the electronic wave number k. Therefore, we replace the electron-phonon interaction $g^{q\nu}_{nk+qnk}$ with its averaged value g.

Then, we obtain a simplified formula for the ultrasonic attenuation coefficient

$$\begin{aligned}\alpha &\sim 2gv_\nu\sum_{nk}\frac{\xi^2_{nk}}{\varepsilon^2_{nk}}\left\{-\frac{\partial f(\varepsilon_{nk})}{\partial\varepsilon_{nk}}\right\}\frac{\varepsilon_{nk}}{|\xi_{nk}|}\delta(|\boldsymbol{v}_{\mathrm{F},nk}\cdot\boldsymbol{\epsilon}_q|)\\ &= 2gv_\nu\sum_{nk}\int d\xi\delta(\xi-\xi_{nk})\frac{|\xi_{nk}|}{\varepsilon_{nk}}\left\{-\frac{\partial f(\varepsilon_{nk})}{\partial\varepsilon_{nk}}\right\}\delta(|\boldsymbol{v}_{\mathrm{F},nk}\cdot\boldsymbol{\epsilon}_q|)\\ &\sim 2gv_\nu\sum_{nk}\delta(\xi_{nk})\delta(|\boldsymbol{v}_{\mathrm{F},nk}\cdot\boldsymbol{\epsilon}_q|)\int d\xi\frac{|\xi|}{\sqrt{\xi^2+\Delta^2_{nk}}}\left\{-\frac{\partial f(\sqrt{\xi^2+\Delta^2_{nk}})}{\partial\sqrt{\xi^2+\Delta^2_{nk}}}\right\}\\ &= 4gv_\nu\sum_{nk}\delta(\xi_{nk})\delta(|\boldsymbol{v}_{\mathrm{F},nk}\cdot\boldsymbol{\epsilon}_q|)f(|\Delta_{nk}|)\end{aligned} \tag{4.8}$$

When we compare the experimental and the theoretical results of the ultrasonic attenuation, it is convenient to use the normalized attenuation coefficient

$$\frac{\alpha_{\mathrm{S}}}{\alpha_{\mathrm{N}}} = \frac{\sum_{nk}\delta(\xi_{nk})\delta(|\boldsymbol{v}_{\mathrm{F},nk}\cdot\boldsymbol{\epsilon}_q|)2f(|\Delta_{nk}|)}{\sum_{nk}\delta(\xi_{nk})\delta(|\boldsymbol{v}_{\mathrm{F},nk}\cdot\boldsymbol{\epsilon}_q|)}, \tag{4.9}$$

where α_{S} and α_{N} are the ultrasonic attenuation coefficient [Eq. (4.8)] in the superconducting state and the normal state, respectively. We calculate the ratio between the ultrasonic attenuation coefficient in the superconducting state α_{S} and that in the normal state α_{N} and compare it with experimental results in Fig. 4.13. Calculated and experimental results of the ultrasonic attenuation in directed to [110] and [001] directions behave similarly; however behaviors of calculated and experimental results in [100] direction are quite different; we will discuss it in the next chapter.

Chapter 5

Discussion

5.1 Origin of the anisotropic superconducting gaps

Although we found some discrepancies between results of our calculations and experiments, we discuss the origin of the anisotropic superconductivity based on our results in this section. After that, we discuss the reason of these discrepancies and possible approaches to overcome these discrepancies.

From the results in the previous chapter, we discovered a significant correlation between the anisotropy of the superconducting gaps in YNi_2B_2C and the variation of the ratio of atomic orbitals on the Fermi surfaces. The electronic states on the Fermi surfaces in YNi_2B_2C consist of Y $4d$, Ni $3d$, B $2s2s$, and C $2s2p$; in particular, the electronic states dominated by Ni $3d$ orbitals couple to phonons very weakly, consequently exhibiting very small gap. To evaluate contributions from each atomic orbitals to the electron-phonon interaction, we fit Z_{nk} by the following function:

$$Z_{nk}^{\mathrm{test}} = Z_{\mathrm{Y}4d} p_{nk}^{\mathrm{Y}4d} + Z_{\mathrm{Ni}3} p_{nk}^{\mathrm{Ni}3d} + Z_{\mathrm{B}2s2p} p_{nk}^{\mathrm{B}4d} + Z_{\mathrm{C}2s2p} p_{nk}^{\mathrm{C}2s2p}, \tag{5.1}$$

where p_{nk}s are contributions from each atomic orbitals to the electronic state φ_{nk} [Eqn. (4.1)]; minimizing

$$\sigma^2 = \sum_{nk} \delta(\xi_{nk})(Z_{nk} - Z_{nk}^{\mathrm{test}})^2, \tag{5.2}$$

we obtain $Z_{\mathrm{Y}4d} = 0.85$, $Z_{\mathrm{Ni}3d} = 0.45$, $Z_{\mathrm{B}2s2p} = 1.21$, and $Z_{\mathrm{C}2s2p} = 4.22$; the fitting error

$$\Delta Z = \frac{\sum_{nk} \delta(\xi_{nk}) |Z_{nk} - Z_{nk}^{\mathrm{test}}| / |Z_{nk}|}{\sum_{nk} \delta(\xi_{nk})} \tag{5.3}$$

is 14.9 %. This result indicates that the mixing of Ni $3d$ orbitals is the key factor behind the mechanism of the anisotropic gap. This picture is supported by the fact that anomalous behavior of specific heat is reduced when some Ni atoms are replaced with Pt atoms in the specific-heat measurement [11, 12, 13] (see Fig. 1.2).

Here we discuss why the Ni $3d$ orbital results in the weak electron-phonon interaction. We infer that the localized nature of Ni 3d orbitals has a crucial role. This orbital is localized strongly on the Ni atom; this localization affects the electron-phonon interaction through the following three possible routes:

- As the ratio of the Ni 3d orbitals increase, electronic wave functions become localized around the Ni ions. This makes the electronic states more sensitive to the deformation potential of the Ni ion, which should yield stronger electron-phonon coupling.

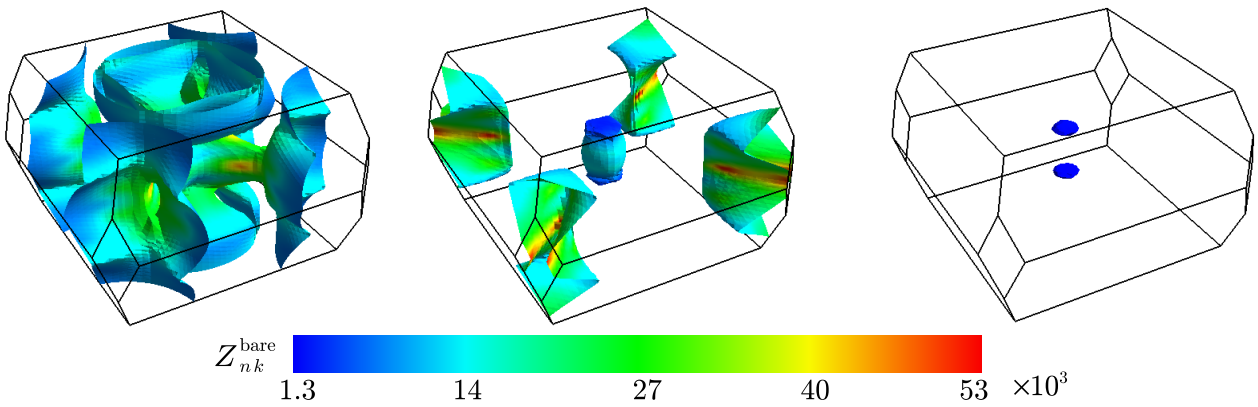

Figure 5.1: The electron-phonon renormalization Z_{nk} (2.76) calculated by using the bare electron-phonon vertex on Fermi surfaces.

- The highly localized Ni $3d$ electrons participate in the local screening of the deformation potential, which should make the electron-phonon coupling weak.
- This localized electronic state makes the density of states at the Fermi level larger; when the DOS at the Fermi level becomes larger, the total electron-phonon coupling represented by the mass-enhancement factor also becomes stronger.

In the present case, the second of the above three is thought to be dominant. To examine the effect of the screening, we calculate the renormalization factor Z_{nk} by using the bare electron-phonon vertex in substitution for the screened one. Figure 5.1 shows the resulting Z_{nk}^{bare}; Performing the same fitting as before, we obtain $Z_{\mathrm{Y}4d} = 6.3 \times 10^3$, $Z_{\mathrm{Ni}3d} = 3.8 \times 10^4$, $Z_{\mathrm{B}2s2p} = -1.3 \times 10^4$, and $Z_{\mathrm{C}2s2p} = 6.7 \times 10^3$; the fitting error is 39.1 % [1]. $Z_{\mathrm{Ni}3}$ is larger than other Zs when we use the bare electron-phonon vertex whereas it is smaller than others when we use the screened vertex. This result shows that the screening to the electron-phonon interaction of the Ni $3d$ orbital is specifically large; this strong screening makes this interaction especially weak. It is supporting evidence of our scenario that YPd_2B_2C has the transition temperature higher than that of YNi_2B_2C [8]; according to our scenario, the Pd $4d$ orbitals are localized more weakly than the Ni $3d$ and therefore interact with phonons more strongly than the Ni $3d$ orbital. This scenario is to be confirmed in the future by the SCDFT calculation for YPd_2B_2C.

5.2 Ultrasonic attenuation experiment vs SCDFT gap functions

5.2.1 Calculated results that agree or disagree with experiments

We classify our calculated results into ones which agree and ones which disagree with experimental results.

- Agree
  - We reproduce the phonon dispersion except for the TA mode at $q = (0.56, 0, 0)$.

[1] The cause of the increase in fitting error is that the bare deformation potential is more sensitive to the wave number than the screened one; this is unrelated to the orbital character. However, it is not a problem when we discuss qualitatively.

  - We observe that the ratio between maximum and minimum of the electron-phonon renormalization is approximately 5; in the previous work [18], it is approximately 7.
  - The calculated superconducting transition temperature shows good agreement with the experimental value.
  - The calculated quasiparticle density of states behave similarly to the experimental tunnel conductance spectrum.

- Disagree
  - We can obtain the only softening of the TA mode at $q = (0.56, 0, 0)$ weaker than that of the experimental result.
  - We can obtain no anomalous attenuation coefficients of the ultrasonic traveling to [100] direction; the attenuation coefficient of this direction shows a peculiar behavior.

In the next section, we discuss why the latter disagreements with experimental results.

5.2.2 Possible causes of the disagreement

Numerical noises

In principle, we cannot completely exclude subtle numerical error due to the BZ integrations using the discrete meshes. However, at least, we successfully minimized such error using the optimized tetrahedron method. For example, we have confirmed that such error was minimized so that it has little contribution to the phonon property, which is the ingredient most sensitive to the accuracy of the BZ integration among the input of the SCDFT (See Fig. 4.5). Hence, we assert that the appreciable discrepancies are not due to the *numerical* error, but due to absence of *physical* effects with the present approximations.

Exchange-correlation potential for the normal state

In the previous study of the combination of dHvA experiment and the band-structure calculation[18], authors shifted upwardly Y $4d$ and Ni $3d$ levels from LDA levels by 0.11 Ry and 0.05 Ry. They state these shifts correspond to the self-interaction and/or the non-local correction to the LDA. On the other hand, reproduction of the Fermi surfaces that agree well with the experiments without such an empirical treatment has not been achieved so far. Thus, the detailed shape of the Fermi surfaces has not been settled.

If we improve on the description of the Fermi surface, the following improvements may be accomplished.

- The nesting which corresponds to the TA mode at $q = (0.56, 0, 0)$ improves on; the strength of the nesting is sensitive to the fine structure of the Fermi surface.
- Regions which consist *only* of Ni $3d$ orbital appear; such regions should couple with phonons very weakly and have quite small gaps.
- The equator corresponding to to the [100] direction changes entirely; the ultrasonic attenuation strongly depends on whether the equator passes gap minima.

To see if the above expectations are likely, we examine whether the treatment of the Y $4d$ and the Ni $3d$ orbitals performed in Ref. [18] improves on the description of the Fermi surface

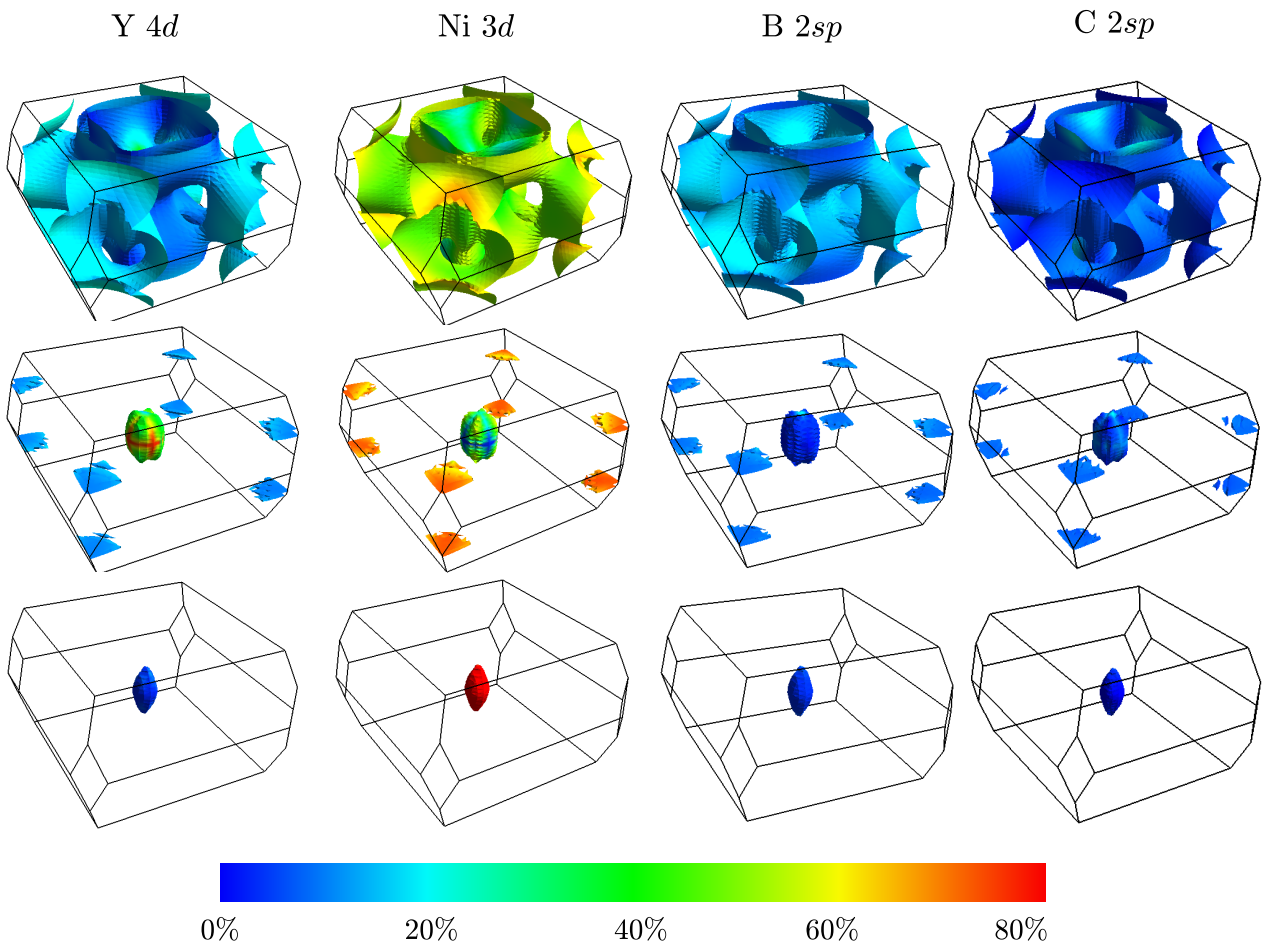

Figure 5.2: Projection of atomic orbitals to the electronic state on the Fermi surfaces ($|\langle\varphi_{\mathrm{Atom}}|\varphi_{nk}\rangle|^2$).

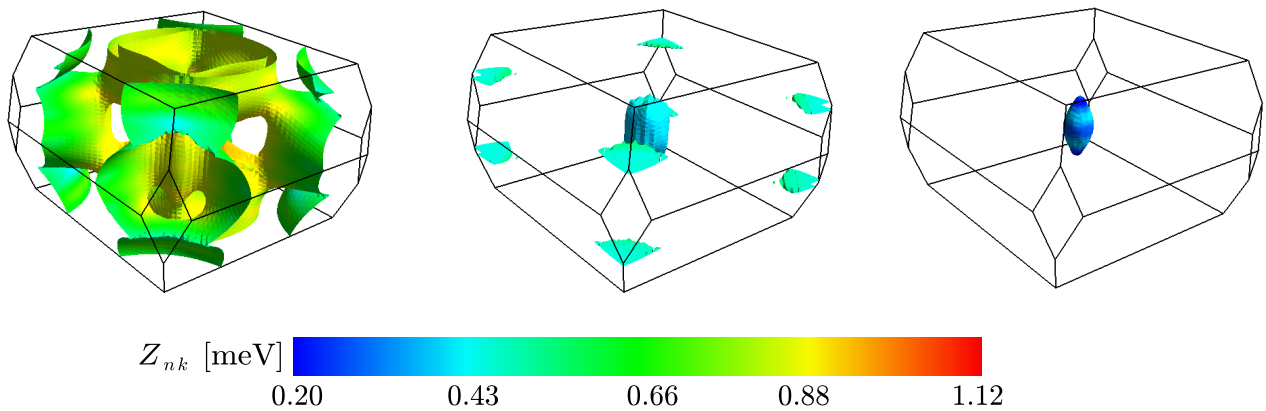

Figure 5.3: The electron-phonon renormalization Z_{nk} (2.76) on Fermi surfaces.

and the ultrasonic attenuation. We set energy-level shifts for Y $4d$ and Ni $3d$ orbitals to 0.5 eV and 0.7 eV so as to obtain the same Fermi surface as that in Ref. [18].

Resulting Fermi surfaces are shown in Fig. 5.2 with the color plot of the orbital character. There is a small electron pocket which consist almost only of the Ni $3d$ orbital at the Γ point.

Figure 5.3 shows the electron-phonon renormalization factor Z_{nk} of electronic states on the

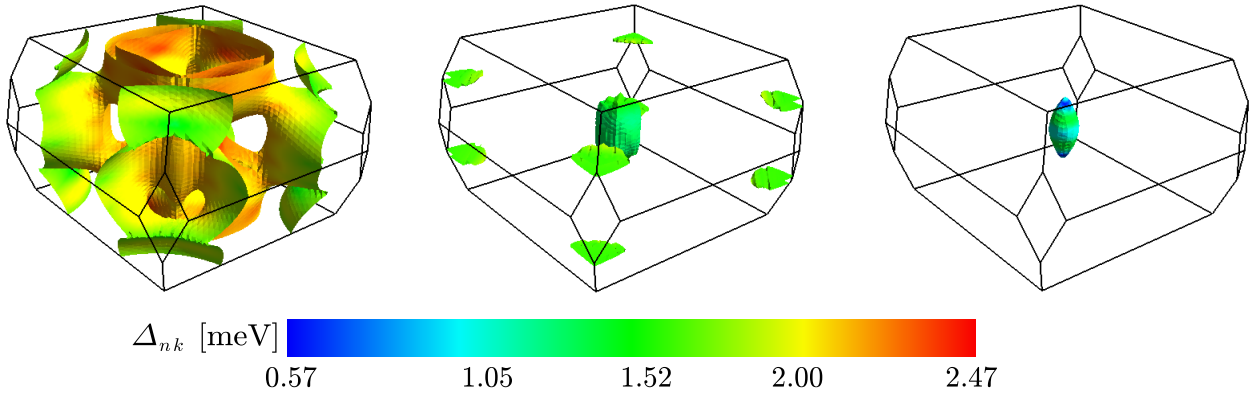

Figure 5.4: Superconducting gap functions Δ_{nk} on Fermi surfaces at 0.1 K.

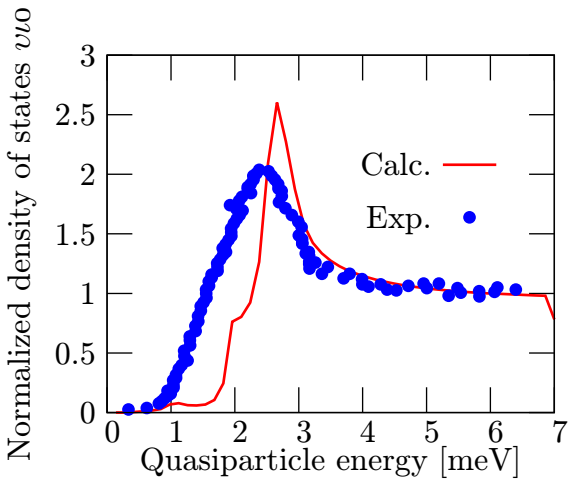

Figure 5.5: Calculated superconducting quasiparticle density of states at 0.1 K and experimental tunnel conductance spectrum at 0.5 K [14].

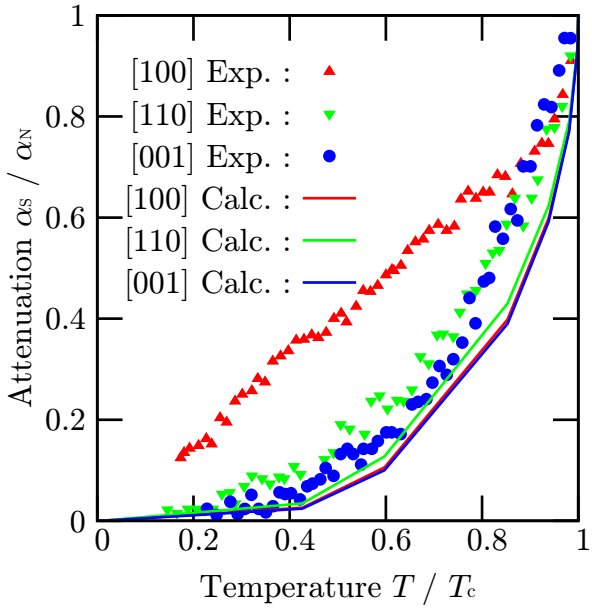

Figure 5.6: Calculated ultrasonic attenuation coefficients beside experimental results [15].

Fermi surfaces; we can see that the electronic states in this small pocket exhibit quite weak electron-phonon coupling. This agree well to the previous study; they indirectly derived the electron-phonon interaction with the combination of the band structure calculation and the dHvA experiment and we obtain the same result from the first-principles phonon calculation.

When we apply this energy-level shifts, the calculated transition temperature descend from 13.4 K to 11.7 K. We calculated the superconducting gap function and depict that in Fig. 5.4. The superconducting gap function is small for the electronic states dominated by the Ni $3d$ orbital. This tendency is the same as that obtained by the superconducting-gap calculation without energy-level shifts (Chap. 4).

Next, we calculated the QPDOS using the calculated gap function. We depict the quasiparticle density of states in Fig. 5.5 together with the experimental tunnel conductance spectrum; it is quite different from that without energy-level shifts 4.12. The shape of the QPDOS does not much deviates from the experimental tunnel conductance spectrum: The peak is sharper

and multiple step-like structures are seen in the slope.

We calculate the ultrasonic attenuation coefficient; we show the resulting coefficient in Fig 5.6. This shows no improvement from the calculation without energy-level shifts; the anomaly of the [100] ultrasonic attenuation coefficient is not seen yet.

We found no improvement in the calculation of the TA mode phonon at $q = (0.56, 0, 0)$; the softening is still weaker than that of the experiment.

The above analysis clarified several remarkable aspects of the calculated superconducting properties. First, the Tc remains rather high (11.7 K) inspite of the modified Fermi surfaces. Second, the correlation between the gap variation and the ratio of the Ni $3d$ orbitals are reproduced. These facts indicate that these properties can be more or less reproduced regardless of the shape and geometry of the calculated Fermi surfaces and therefore reinforce our view that the experimental results are perfectly explained by improving on the description of the Fermi surfaces. At least, however, summing up the above results, we conclude that the shifting scheme employed in the previous DFT calculation [18] does not improve on the description of the anisotropic superconducting gaps. We should use advanced functional such as the hybrid-functional or the DFT+U formalism to describe anomalous ultrasonic attenuation and the strong softening of the TA mode phonon at $q = (0.56, 0, 0)$; this remains as a future work.

Formalism of the ultrasonic attenuation

We used a very simple formula for the ultrasonic attenuation [Eq. (4.8)] in this study; this simplification allows us to examine how the anisotropic superconducting gap yields the anomalous ultrasonic attenuation. We compare our formula for the isotropic superconductor as follows.

$$\frac{\alpha_{\mathrm{S}}}{\alpha_{\mathrm{N}}} = 2f(\Delta) \qquad \text{Isotropic.} \tag{5.4}$$

$$\frac{\alpha_{\mathrm{S}}}{\alpha_{\mathrm{N}}} = \frac{\sum_{nk} \delta(\xi_{nk})\delta(|\boldsymbol{v}_{\mathrm{F},nk} \cdot \boldsymbol{\epsilon}_q|) 2f(|\Delta_{nk}|)}{\sum_{nk} \delta(\xi_{nk})\delta(|\boldsymbol{v}_{\mathrm{F},nk} \cdot \boldsymbol{\epsilon}_q|)} \qquad \text{Anisotropic in this work.} \tag{5.5}$$

The difference between them is that the latter is the average of the Fermi-Dirac distribution function of the anisotropic superconducting gap along the corresponding equator while the former is the Fermi-Dirac distribution function of the isotropic superconducting gap. To obtain the attenuation coefficient consistent with the experiment from Eq. 5.5, we have confirmed that the ratio of the maximum to the minimum of the superconducting gap function must be at least $\sim$10. However, the ratio calculated from our ab initio gap function is approximately 2.5; this is the reason of the disagreement.

Here, we also focus on the temperature dependence of the attenuation coefficient. In the experimental result, the ultrasonic attenuation coefficient depend largely on the temperature; such temperature dependence cannot be described with the formula Eq. (5.5). This suggests that effects of the temperature are relevant in the present system and the formula Eq. (5.5) used in our analysis is not applicable.

From these reasons, we expect that the calculated attenuation coefficient is improved on with Eq. (4.6) rather than Eq. (4.8). This is also a future work.

Chapter 6

Summary and conclusion

In this study, we performed a first principle investigation to find the origin of the anisotropic superconductivity in YNi_2B_2C. To treat precisely the wavenumber dependence of the electronic and phononic structure, we considered what causes the numerical error; with the broadening method, we encounter systematic errors that are dependent on broadening widths; with the linear tetrahedron method, on the other hand, numerical convergence is difficult to achieve because of the systematic overestimation (underestimation) for approximating the convex (concave) functions. Then, we developed the optimized tetrahedron method which uses higher order interpolation to overcome the systematic error of the linear interpolation. Using this method, we performed the calculation of the superconducting gap and obtain a highly k dependent superconducting gap; then, we examined if we could reproduce the experimental results (the phonon dispersion, the tunnel conductance spectrum, and the ultrasonic attenuation coefficient) that suggest the anisotropic superconductivity in YNi_2B_2C.

From our investigation, we found that the origin of the anisotropic superconductivity is traced back to the variation of the rate of the Ni $3d$ orbital on the Fermi surface. As the components of these orbitals increase, the electron-phonon coupling of the electronic state becomes weak and its superconducting gap function becomes small. Because of this effect, the superconducting gap rapidly varying over the Fermi surface emerges. As a possible scenario, we proposed that the localized nature of the Ni $3d$ orbitals is a key factor for the weakening of the electron-phonon coupling. This scenario is also supported by the T_c in YPd_2B_2C higher than that in YNi_2B_2C. We also noticed that it is important to improve on the description of the Fermi surface and the energy level of the localized orbital; they largely affect the softening of the phonon and the ultrasonic attenuation. With the present improvement, we will derive more knowledge from YNi_2B_2C.

Let us also discuss the methodological aspect of the present study. As a matter of fact, the newly developed optimized tetrahedron method has large potential to increase the accuracy for general calculations dealing with the BZ integral in the crystal. This method is applicable to various kinds of calculations such as the susceptibility [80], the phonon frequency [81], the local Green's function as part of the dynamical mean field theory in the Hubbard model [82], the phonon linewidth, and so on. Although there have also been different alternative methods to improve on the linear tetrahedron method [83, 84], our method is superior to them in its compatibility. This method is effcient especially for the hybrid-DFT [85] calculation and the GW calculation [86]: Although the computational costs for these calculations are proportional to the square of the number of k points, our method can make them feasible by reducing the number of k points required for good convergence.

Bibliography

[1] C. Mazumdar, R. Nagarajan, C. Godart, L. Gupta, M. Latroche, S. Dhar, C. Levy-Clement, B. Padalia, R. Vijayaraghavan, Solid State Communications **87**, 413 (1993).

[2] R. Cava, H. Takagi, H. Zandbergen, J. Krajewski, W. Peck, T. Siegrist, B. Batlogg, R. Vandover, R. Felder, K. Mizuhashi, J. Lee, H. Eisaki, S. Uchida, Nature(London) **367**, 252 (1994).

[3] H. Fukuyama, J. Akimitsu, 超伝導ハンドブック, 朝倉書店, (2009).

[4] H. Ku, C. Lai, Y. You, J. Shieh, W. Guan, Phys. Rev. B **50**, 351 (1994).

[5] M. E. Massalami, R. Rapp, G. Nieuwenhuys, Physica C: Superconductivity **304**, 184 (1998).

[6] S. Skanthakumar, J. Lynn, Physica B: Condensed Matter **259261**, 576 (1999).

[7] B. Cho, P. Canfield, D. Johnston, Phys. Rev. B **52**, R3844–R3847 (1995).

[8] R. Cava, H. Takagi, B. Batlogg, H. Zandbergen, J. Krajewski, W. Peck, R. Vandover, R. Felder, T. Siegrist, K. Mizuhashi, J. Lee, H. Eisaki, S. Carter, S. Uchida, Nature (London) **367**, 146 (1994).

[9] D. Lawrie, J. Franck, Physica C **245**, 159 (1995).

[10] K. Cheon, I. Fisher, P. Canfield, Physica C **312**, 35 (1999).

[11] M. Nohara, M. Isshiki, F. Sakai, H. Takagi, Journal of the Physical Society of Japan **68**, 1078–1081 (1999).

[12] M. Nohara, H. Suzuki, N. Mangkorntong, H. Takagi, Physica C: Superconductivity **341348, Part 4**, 2177 (2000), proceedings of the International Conference on Materials and Mechanisms of Superconductivity High Temperature Superconductors {VI}.

[13] K. Izawa, A. Shibata, Y. Matsuda, Y. Kato, H. Takeya, K. Hirata, C. J. van der Beek, M. Konczykowski, Phys. Rev. Lett. **86**, 1327 (2001).

[14] P. Martínez-Samper, H. Suderow, S. Vieira, J. Brison, N. Luchier, P. Lejay, P. Canfield, Phys. Rev. B **67**, 014526 (2003).

[15] T. Watanabe, M. Nohara, T. Hanaguri, H. Takagi, Phys. Rev. Lett. **92**, 147002 (2004).

[16] K. Izawa, K. Kamata, Y. Nakajima, Y. Matsuda, T. Watanabe, M. Nohara, H. Takagi, P. Thalmeier, K. Maki, Phys. Rev. Lett. **89**, 137006 (2002).

[17] F. Weber, L. Pintschovius, W. Reichardt, R. Heid, K.-P. Bohnen, A. Kreyssig, D. Reznik, K. Hradil, Phys. Rev. B **89**, 104503 (2014).

[18] K. Yamauchi, H. Katayama-Yoshida, A. Yanase, H. Harima, Physica C **412**, 225 (2004).

[19] P. De Gennes, Superconductivity Of Metals And Alloys, Advanced Books Classics Series, Westview Press, 1999.

[20] H. Sakata, M. Oosawa, K. Matsuba, N. Nishida, H. Takeya, K. Hirata, Phys. Rev. Lett. **84**, 1583 (2000).

[21] H. Nishimori, K. Uchiyama, S.-i. Kaneko, A. Tokura, H. Takeya, K. Hirata, N. Nishida, Journal of the Physical Society of Japan **73**, 3247 (2004).

[22] T. Baba, T. Yokoya, S. Tsuda, T. Watanabe, M. Nohara, H. Takagi, T. Oguchi, S. Shin, Phys. Rev. B **81**, 180509 (2010).

[23] G. Eliashberg, Sov. Phys. JETP **11**, 696 (1960).

[24] J. Schrieffer, Theory of Superconductivity, Advanced Book Program Series, Advanced Book Program, Perseus Books, (1983).

[25] Y. Takada, Journal of the Physical Society of Japan **45**, 786 (1978).

[26] Y. Takada, Journal of the Physical Society of Japan **49**, 1267–1275 (1980).

[27] L. N. Oliveira, E. K. U. Gross, W. Kohn, Phys. Rev. Lett. **60**, 2430 (1988).

[28] M. A. L. Marques, M. Lüders, N. N. Lathiotakis, G. Profeta, A. Floris, L. Fast, A. Continenza, E. K. U. Gross, S. Massidda, Phys. Rev. B **72**, 024546 (2005).

[29] A. Floris, G. Profeta, N. N. Lathiotakis, M. Lüders, M. A. L. Marques, C. Franchini, E. K. U. Gross, A. Continenza, S. Massidda, Phys. Rev. Lett. **94**, 037004 (2005).

[30] G. Profeta, C. Franchini, N. N. Lathiotakis, A. Floris, A. Sanna, M. A. L. Marques, M. Lüders, S. Massidda, E. K. U. Gross, A. Continenza, Phys. Rev. Lett. **96**, 047003 (2006).

[31] R. Akashi, R. Arita, Phys. Rev. Lett. **111**, 057006 (2013).

[32] A. Sanna, G. Profeta, A. Floris, A. Marini, E. K. U. Gross, S. Massidda, Phys. Rev. B **75**, 020511 (2007).

[33] P. Hohenberg, W. Kohn, Phys. Rev. **136**, B864 (1964).

[34] W. Kohn, L. J. Sham, Phys. Rev. **140**, A1133 (1965).

[35] D. Ceperley, B. Alder, Phys. Rev. Lett. **45**, 566 (1980).

[36] J. Perdew, A. Zunger, Phys. Rev. B **23**, 5048 (1981).

[37] A. Becke, Phys. Rev. A **38**, 3098 (1988).

[38] J. P. Perdew, K. Burke, M. Ernzerhof, Phys. Rev. Lett. **78**, 1396 (1997).

[39] N. Mermin, Phys. Rev. **137**, A1441 (1965).

[40] S. Baroni, S. de Gironcoli, A. Dal Corso, P. Giannozzi, Rev. Mod. Phys. **73**, 515 (2001).

[41] M. Lüders, M. A. L. Marques, N. N. Lathiotakis, A. Floris, G. Profeta, L. Fast, A. Continenza, S. Massidda, E. K. U. Gross, Phys. Rev. B **72**, 024545 (2005).

[42] A. Abrikosov, L. Gor'kov, I. Dzyaloshinski, Dzialoshinski, Methods of Quantum Field Theory in Statistical Physics, Dover Books on Physics Series, Dover Publications, (1975).

[43] S. Kurth, M. Marques, M. Lüders, E. K. U. Gross, Phys. Rev. Lett. **83**, 2628 (1999).

[44] M. Methfessel, A. T. Paxton, Phys. Rev. B **40**, 3616 (1989).

[45] O. Jepsen, O. K. Andersen, Solid State Commun. **9**, 1763 (1971).

[46] P. Ravindran, A. Kjekshus, H. Fjellvåg, P. Puschnig, C. Ambrosch-Draxl, L. Nordström, B. Johansson, Phys. Rev. B **67**, 104507 (2003).

[47] M. Calandra, G. Profeta, F. Mauri, Phys. Rev. B **82**, 165111 (2010).

[48] T. Bazhirov, J. Noffsinger, M. L. Cohen, Phys. Rev. B **82**, 184509 (2010).

[49] P. Giannozzi, S. Baroni, N. Bonini, M. Calandra, R. Car, C. Cavazzoni, D. Ceresoli, G. L. Chiarotti, M. Cococcioni, I. Dabo, A. Dal Corso, S. de Gironcoli, S. Fabris, G. Fratesi, R. Gebauer, U. Gerstmann, C. Gougoussis, A. Kokalj, M. Lazzeri, L. Martin-Samos, N. Marzari, F. Mauri, R. Mazzarello, S. Paolini, A. Pasquarello, L. Paulatto, C. Sbraccia, S. Scandolo, G. Sclauzero, A. P. Seitsonen, A. Smogunov, P. Umari, R. M. Wentzcovitch, J. Phys.: Condens. Matter **21**, 395502 (2009).

[50] I release the modified Quantum ESPRESSO in http://qeforge .

[51] J. Nagamatsu, N. Nakagawa, T. Muranaka, Y. Zenitani, J. Akimitsu, Nature (London) **410**, 63 (2001).

[52] Y. Kong, O. V. Dolgov, O. Jepsen, O. K. Andersen, Phys. Rev. B **64**, 020501 (2001).

[53] K.-P. Bohnen, R. Heid, B. Renker, Phys. Rev. Lett. **86**, 5771 (2001).

[54] H. J. Choi, D. Roundy, H. Sun, M. L. Cohen, S. G. Louie, Phys. Rev. B **66**, 020513 (2002).

[55] A. Eiguren, C. Ambrosch-Draxl, Phys. Rev. B **78**, 045124 (2008).

[56] M. Hanfland, K. Syassen, N. Christensen, D. Novikov, Nature (London) **408**, 174 (2000).

[57] S. Deemyad, J. S. Schilling, Phys. Rev. Lett. **91**, 167001 (2003).

[58] V. Struzhkin, M. Eremets, W. Gan, H. Mao, R. Hemley, Science **298**, 1213 (2002).

[59] K. Shimizu, H. Ishikawa, D. Takao, T. Yagi, K. Amaya, Nature (London) **419**, 597 (2002).

[60] D. R. Hamann, M. Schlüter, C. Chiang, Phys. Rev. Lett. **43**, 1494 (1979).

[61] D. Vanderbilt, Phys. Rev. B **41**, 7892 (1990).

[62] We used the pseudopotential Li.pbe-s-rrkjus_psl.0.2.1.UPF from http://www.quantum-espresso.org.

[63] S. de Gironcoli, Phys. Rev. B **51**, 6773 (1995).

[64] W. L. McMillan, Phys. Rev. **167**, 331 (1968).

[65] R. Dynes, Solid State Commun. **10**, 615 (1972).

[66] We use the pseudopotentials Al.pbe-n-rrkjus_psl.0.1.UPF, Al.pz-n-rrkjus_psl.0.1.UPF, Nb.pbe-spn-rrkjus_psl.0.3.0.UPF, Nb.pz-spn-rrkjus_psl.0.3.0.UPF, Ta.pbe-spn-rrkjus_psl.0.2.UPF, Ta.pz-spn-rrkjus_psl.0.2.UPF, Pb.pbe-dn-rrkjus_psl.0.2.2.UPF, Pb.pz-dn-rrkjus_psl.0.2.2.UPF, Mg.pbe-n-rrkjus_psl.0.3.0.UPF, Mg.pz-n-rrkjus_psl.0.3.0.UPF, B.pbe-n-rrkjus_psl.0.1.UPF, and B.pz-n-rrkjus_psl.0.1.UPF (http://theossrv1.epfl.ch/Main/Pseudopotentials).

[67] A. Floris, A. Sanna, M. Lders, G. Profeta, N. Lathiotakis, M. Marques, C. Franchini, E. Gross, A. Continenza, S. Massidda, Physica C: Superconductivity **456**, 45 (2007), recent Advances in MgB2 Research.

[68] A. Floris, A. Sanna, S. Massidda, E. K. U. Gross, Phys. Rev. B **75**, 054508 (2007).

[69] J. P. Perdew, Y. Wang, Phys. Rev. B **45**, 13244–13249 (1992).

[70] S. Y. Savrasov, D. Y. Savrasov, Phys. Rev. B **54**, 16487 (1996).

[71] 国立天文台, 理科年表, 丸善出版, 2014.

[72] We use the pseudopotentials Y.pbe-spn-rrkjus_psl.0.2.3.UPF, Ni.pbe-n-rrkjus_psl.0.1.UPF, B.pbe-n-rrkjus_psl.0.1.UPF, and C.pbe-n-rrkjus_psl.0.1.UPF in PSLibrary 0.3.1 (http://theossrv1.epfl.ch/Main/Pseudopotentials).

[73] T. Siegrist, R. Cava, J. Krajewski, W. P. Jr., Journal of Alloys and Compounds **216**, 135 (1994).

[74] I am developing a Fermi surface visualization tool "Fermi Surfer"; and it is released in http://sourceforge.jp/projects/fermisurfer/ .

[75] J. Hartmann, F. Gompf, B. Renker, Journal of Low Temperature Physics **105**, 1629–1634 (1996).

[76] V. Hadjiev, L. Bozukov, M. Baychev, Phys. Rev. B **50**, 16726–16728 (1994).

[77] H.-J. Park, H.-S. Shin, H.-G. Lee, I.-S. Yang, W. Lee, B. Cho, P. Canfield, D. Johnston, Phys. Rev. B **53**, 2237–2240 (1996).

[78] A. Litvinchuk, L. Börjesson, N. Phuc, N. Hong, Phys. Rev. B **52**, 6208–6210 (1995).

[79] F. Weber, S. Rosenkranz, L. Pintschovius, J.-P. Castellan, R. Osborn, W. Reichardt, R. Heid, K.-P. Bohnen, E. Goremychkin, A. Kreyssig, K. Hradil, D. Abernathy, Phys. Rev. Lett. **109**, 057001 (2012).

[80] J. Rath, A. J. Freeman, Phys. Rev. B **11**, 2109 (1975).

[81] S. Y. Savrasov, Phys. Rev. Lett. **69**, 2819 (1992).

[82] T. Fujiwara, S. Yamamoto, Y. Ishii, J. Phys. Soc. Jpn. **72**, 777 (2003).

[83] P. E. Blöchl, O. Jepsen, O. K. Andersen, Phys. Rev. B **49**, 16223 (1994).

[84] F. E. Harris, Journal of Physics: Condensed Matter **14**, 621 (2002).

[85] J. Perdew, M. Emzerhof, K. Burke, J. Chem. Phys. **105**, 9982 (1996).

[86] L. Hedin, Phys. Rev. **139**, A796 (1965).

Acknowledgment

Professor Sinji Tsuneyuki(常行 真司),
Associate-professor Yoshihiro Gohda(合田 義弘),
Assistant-professor Ryosuke Akashi(明石 遼介),
Ms. Emi Shimoshikiryo(下敷領 恵美), Ms. Makiko Fukuda(福田 牧子),
Dr. Terumasa Tadano(只野 央将), Dr. Toshiki Iwazaki(岩崎 誉志紀),
Dr. Kanako Yoshizawa(吉澤 香奈子),
Dr. Yasutomi Tatetsu(立津 慶幸), Dr. Daisuke Hirai(平井 大介)
Dr. Masayuki Ochi(越智 正之), Mr. Yoshiyuki Yamamoto(山本 良幸)
Mr. Hideki Misawa(見澤 英樹), Mr. Tatsuya Endo(遠藤 辰哉),
Mr. Nobuya Sato(佐藤 暢哉), Mr. Shunsuke Yamada(山田 俊介),
Mr. Hiroki Katow(加藤 洋生), Mr. Tatsuro Nishimoto(西本 健郎),
Mr. Yuta Tanaka(田中 悠太), Mr. Naoto Tsujimoto(辻本 直人),
Members of the Aoki(青木) research group,
Assistant-professor Hiroyasu Matsuura(松浦 弘泰)

Because I want to convey directly thankfulness, I do not write that here.

Associate-professor Kazuma Nakamura(中村 和磨),
Dr. Takashi Miyake(三宅 隆), Dr. Rei Sakuma(佐久間 怜)

Thank you for giving a tutorial on the screened Coulomb interaction.

Professor Ryotaro Arita(有田 亮太郎),
Everyone who discussed with me in the poster session

I am grad to discuss this topic in that session. I hope that the FermiSurfer program help your researches.

Dear Quantum ESPRESSO developer

Thank you for developing such a nice code !

FUJITSU LIMITED

Thank you for developing such a nice supercomputer !

Information Technology Center, The University of Tokyo

Thank you for your maintenance for the Oakleaf-FX supercomputer.

Oakleaf-FX

01010100011010000110000101101110011010110010000001111001011011110111010100100001

COFFEE BITTER(ビタール) in Ameya street

Thank you for serving delicious coffee beans. The roasting and the pricing of you are very

attractive.